

THESIS FOR THE DEGREE OF LICENTIATE IN ENGINEERING

Computational Aero Acoustics for Vehicle Applications

JOHAN LARSSON

Department of Thermo and Fluid Dynamics

CHALMERS UNIVERSITY OF TECHNOLOGY

Göteborg, Sweden, 2002

Computational Aero Acoustics for Vehicle Applications
JOHAN LARSSON

© JOHAN LARSSON, 2002

ISSN 1101-9972
ISRN CTH-TFD-PB-0205

Department of Thermo and Fluid Dynamics
Chalmers University of Technology
S-412 96 Göteborg, Sweden
Phone +46-(0)31-7721400
Fax: +46-(0)31-180976

This document was typeset using L^AT_EX

Printed at Chalmers Reproservice
Göteborg, Sweden 2002

Computational Aero Acoustics for Vehicle Applications

by

Johan Larsson

Department of Thermo and Fluid Dynamics
Chalmers University of Technology
S-412 96 Göteborg, Sweden

Abstract

The field of Aero Acoustics, which studies aerodynamically generated sound, has been around since the 1950's. In the beginning, the main focus was to make commercial airliners less noisy, but as the field has matured, a wider range of applications has been studied.

Consumer surveys on vehicles consistently rank wind noise as a top ten problem, which has led the vehicle industry to invest time and money to decrease this problem. A deeper understanding of aero acoustics would not only be beneficial in problems like wind noise, but also for problems like climate system noise, exhaust system flows, and others.

This thesis focuses mainly on the scalar wave equations pioneered by Lighthill. A thorough review, including the inherent limitations in each method, is conducted. The equation by Curle is identified as the one that meets the objectives of this study the best, and it is implemented and solved for an open cavity. Since no experimental data is available for this case, a Direct Simulation (two-dimensional), resolving both the flow and the acoustics, is performed.

The sound field computed by Curle's equation agrees well with the Direct Simulation, but the computational cost involved is considerably smaller. This makes Curle's equation, together with the simplifications introduced and validated in this thesis, suitable for engineering use.

The acoustic noise generation is studied in detail. The wall pressure fluctuations are found to account for roughly 90% of the radiated sound intensity, and the viscous and entropy fluctuations are found to be negligible. The downstream region of the cavity is found to generate the most sound, a fact which can be used to explain the directivity of the radiated sound.

Keywords: CAA, aero acoustics, Curle, low Mach number, cavity, open cavity, CFD, compressible flow, noise generation, sound generation

Preface

This thesis is, in part, based on 2 internal reports, listed in the bibliography as Larsson [1, 2]:

- Larsson, J., A Note on Numerical Errors, Internal Report 01/06, revised Sept 2002, Department of Thermo and Fluid Dynamics, Chalmers University of Technology, 2002.
- Larsson, J., On Low Mach Number Preconditioning by Pressure Under-relaxation, Internal Report 02/02, Department of Thermo and Fluid Dynamics, Chalmers University of Technology, 2002.

The results of this thesis have been submitted for publication to the 9th AIAA/CEAS Aeroacoustics Conference as:

- Larsson, J., Davidson, L., Olsson, M., and Eriksson, L.-E., Aero Acoustic Investigation of an Open Cavity at Low Mach Number.

Acknowledgements

This work was carried out at the Department of Thermo and Fluid Dynamics at Chalmers University of Technology, at Volvo Car Corporation, and, to a lesser extent, at the University of Waterloo, Canada. The project was funded by Volvo Car Corporation and VINNOVA.

I would like to thank Prof. Lars Davidson for the supervision and, your perhaps best quality, the many encouraging talks!

I would also like to thank Prof. Lars-Erik Eriksson for taking the time to explain many things about aero acoustics and numerical methods. Good luck on the new job!

Thanks also to Dr. Magnus Olsson for giving me this opportunity, and also for having wild and unorthodox ideas!

To the people at Volvo and Chalmers; I have had a great time, and you have all been part of that. Mattias Billson deserves a special mentioning; you have always taken the time for interesting discussions. To Jonas Ask: Good luck!

Last, but definitely not the least, thanks Lara for being who you are. You give me lots of joy in life, and you show me new sides of myself!

Nomenclature

Geometric quantities

x_i	cartesian tensor coordinate
y_i	cartesian tensor coordinate of source location
\mathbf{x}	observation coordinates
\mathbf{y}	source coordinates
L	cavity length (or integral length scale)
D	cavity depth
r	distance from source to observer
n_i	unit surface normal pointing towards fluid
l_i	unit vector pointing from source to observer
V_c	cell volume
A_f	face area
η	Kolmogorov length scale

Thermodynamic quantities

ρ	density
p	pressure
T	temperature
h	enthalpy
e	internal energy
e_o	total internal energy
c_p	specific heat at constant pressure (or pressure coefficient)
c_v	specific heat at constant volume
γ	ratio of specific heats
R	gas constant
a	speed of sound

Various quantities

u_i	instantaneous velocity
v_i	surface velocity
τ_{ij}	viscous stress tensor
T_{ij}	Lighthill's tensor
f	frequency
t	time
τ	retarded time
Π	Phillips' acoustic variable
I	acoustic intensity
SPL	sound pressure level
ϵ	artificial dissipation parameter
σ_o	buffer layer parameter
$\delta_{0.99}$	boundary layer thickness
δ^*	displacement thickness
θ	momentum thickness

Dimensionless quantities

Re_L	Reynolds number based on length L
Pr	Prandtl number
M	Mach number
St_L	Strouhal number based on length L
C_D	drag coefficient
c_p	pressure coefficient (or specific heat)
c_f	skin friction coefficient

Math symbols

f'	fluctuating quantity
\overline{f}	average, temporal or spatial
\tilde{f}	Favre average
\dot{f}	time derivative
d/dt	convective time derivative
∇	gradient operator
δ_{ij}	Kronecker delta
$\delta(f)$	Dirac's delta function
$H(f)$	Heaviside's step function
f_o	constant of integration (except for e_o)
f_∞	far field value
f_{rms}	root mean square
$ f $	magnitude

Contents

Abstract	iii
Preface	v
Acknowledgements	vii
Nomenclature	ix
1 Introduction	1
1.1 Motivation	2
1.2 Objectives	3
2 Review of CAA Methods	5
2.1 Direct Simulation	7
2.1.1 Large Scale Simulation	10
2.1.2 Wave Extrapolation Methods	10
2.2 Scalar Equations	11

2.2.1	Lighthill's Equation	12
2.2.2	Ffowes Williams and Hawkings' Equation	13
2.2.3	Curle's Equation	19
2.2.4	Phillips' Equation	22
2.2.5	Lilley's Equation	25
2.2.6	Discussion on Scalar Equations	26
2.3	Systems of Equations	28
2.3.1	Linear Euler Equations	28
2.3.2	Hardin and Pope's Equations	29
2.4	Sound Generation	30
2.4.1	Importance of Compressibility	30
2.4.2	Resolution Requirements	32
2.5	Sound Pressure Level	33
3	Choice of Method and Test Case	35
3.1	Acoustic Method	35
3.2	Test Case	36
3.2.1	Review on Open Cavities	36
3.2.2	Summary of Open Cavity Findings	39
3.2.3	Choice of Test Case	40
4	Methodology, Direct Simulation	41

4.1	Finite Volume Formulation	42
4.2	Inviscid Flux	42
4.3	Viscous Flux	45
4.4	Time Integration	46
4.5	Boundary Conditions	47
4.5.1	Inviscid BC	47
4.5.2	Viscous BC	48
4.5.3	Buffer Layers	48
5	Methodology, Curle’s Equation	51
5.1	Volume Sources	52
5.2	Surface Sources	53
5.3	Time Accumulation	53
5.4	Extension to 3D	55
5.5	Numerical Experiments	56
6	Open Cavity, Direct Simulation	59
6.1	Cavity Drag	60
6.2	Incoming Boundary Layer	62
6.3	Flow Features	64
6.4	Radiated Sound	68
6.5	Grid Independence	72

6.5.1	Resolution	72
6.5.2	Boundary Conditions	72
7	Open Cavity, Curle's Equation	75
7.1	Contributing Source Terms	75
7.2	Radiated Sound	78
7.3	Wall Sources	79
7.3.1	Pressure Sources	79
7.3.2	Viscous Sources	81
7.3.3	Correlations	81
7.3.4	Directivity	83
7.4	Volume Sources	84
7.5	Grid Independence of Curle's Equation	87
8	Summary of Results	89
8.1	Future Work	91

Chapter 1

Introduction

Telephone wires ‘singing’ in the wind, the tones generated by blowing across the opening of a bottle, and the noise generated by a jet engine are only a few examples of flow-induced sound, commonly called *aero acoustics*. Aero acoustics as a science began about 50 years ago, sparked by the development of jet airliners and the need to reduce their noise levels in order to operate in or near cities. The recent increase in computational power has led to a renewed interest in aero acoustics, but this time in the numerical simulation of sound by *Computational Aero Acoustics* (CAA).

Even though the concept of sound has been around for many years, some confusion seems to exist regarding the definition of sound, at least in the field of CAA. From the perspective of a human being, sound is the pressure fluctuation in or around the ears. In most texts on CAA, however, sound is defined as the pressure fluctuations propagating as waves at the speed of sound. Other pressure fluctuations, like the ones that are part of the turbulence, are often labeled ‘pseudo sound’. The reason to this is probably that all early efforts on aero acoustics were focused on problems like jet noise, where the sound of interest is at observation locations far from the origin of the sound. Since the ‘pseudo sound’ decreases faster with distance than the pressure fluctuations propagating as waves, only the sound waves will prevail far from the source.

Since modern aero acoustics deals not only with problems like jet noise, but also with problems where the sound very close to the origin is of importance, the term ‘pseudo sound’ is outdated and should not be used. From here

on, *sound* is defined to be the pressure fluctuation, *sound wave* is defined to be the part propagating as waves at the speed of sound, and *hydrodynamic pressure fluctuation* is defined to be the pressure fluctuations associated with phenomena like turbulence.

1.1 Motivation

The primary types of noise in a modern vehicle are tire noise, engine noise, wind noise, and noise from the climate system, with the latter two being mainly aero acoustic phenomena. Reductions in tire and engine noise during the last decades have led to wind noise being the primary type at vehicle speeds above approximately 120 km/h. Customer surveys like JD Power¹ show the importance of reducing the wind noise, since it consistently ranks as one of the most common complaints. Climate system noise rarely shows up in customer surveys, but this is probably due to the fact that all brands and models are as noisy, which leads customers to expect high sound levels. All in all, there has been an increased focus on aero acoustics in the automotive business during the last 5 years.

The time-to-market in the automotive industry has been shrinking for the last decade, and as a consequence there is very little time to build prototypes. Much of the analysis of new design suggestions must instead be done numerically, and hence this thesis deals primarily with CAA.

As will be seen partly in chapter 2, most of the academic research on aero acoustics to this date has been aimed at problems like jet noise, with high Mach numbers, and often a focus on the propagation of sound waves. Only a few studies have turned their attention to the actual noise generation, with investigations of, for example, which regions in a jet the noise sources are large. To the knowledge of this author, no such studies have been conducted in wall bounded flows.

Many texts on aero acoustics argue that, at low Mach numbers, noise sources on solid surfaces will be more powerful than sources in the fluid, but no quantitative results have been presented.

¹See for example www.jdpower.com.

1.2 Objectives

This research is aimed at testing the following hypotheses or statements:

1. In a low Mach number, wall bounded, flow, the noise sources in the fluid are negligible.
2. For a simple geometry, a suitable scalar equation will compute the radiated sound accurately.
3. It is possible to compare different design suggestions² by simply comparing the noise sources, without taking the propagation into account.

Apart from testing these hypotheses, the research aims at:

4. Conducting a thorough review of CAA methods.
5. Furthering of the understanding of low Mach number noise generation.
6. Implementing and testing a simple method for sound generation and propagation.

²With ‘different design suggestions’ is meant geometries that differ slightly.

Chapter 2

Review of CAA Methods

The compressible continuity, momentum, and energy, equations describe the motions in a fluid. Hence, the solution to these equations, subjected to boundary conditions, will include not only convection and diffusion, but also acoustic wave propagation. The acoustic part of the solution can not, in general, be separated from the rest of the solution. In many cases, though, it is possible to view the flow and the acoustics as two different fields.

Depending on the characteristics of the interaction between the flow and the acoustics, aero acoustic problems can be divided into two categories. If there is a mutual dependence of the flow and the acoustics, i.e. that energy is being transferred both from the flow to the acoustics and vice versa, the problem is called a *two-way coupled* case. If the acoustic part is dependent on the flow, but the flow is independent of the acoustics, the problem is called a *one-way coupled* case. Most low Mach number flows exhibit a one-way coupling, which is the basis for most aero acoustic modeling. There are, however, exceptions to this, with flows involving resonance being the main one. One example of a one-way coupled flow could be the vortex shedding around a cylinder at low Mach numbers, while the so-called ‘booming’ noise, that sometimes appears when driving a car with the sunroof open, could be an example of a two-way coupled flow. In the latter case, vortices in the shear layer radiate sound waves into the passenger compartment. These sound waves are reflected upwards, and when they reach the shear layer, the release of a new vortex is triggered.

For cases exhibiting a one-way coupling, the problem can be split into a

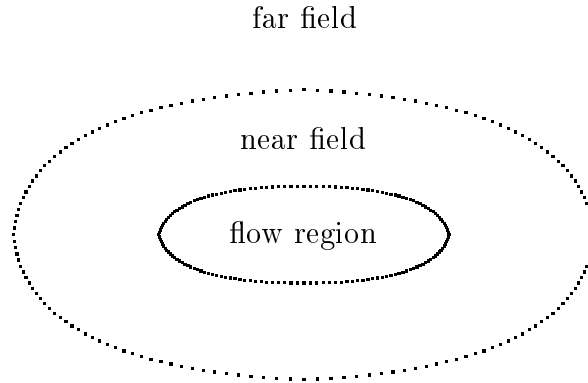


Figure 2.1: Regions in CAA

flow problem and an acoustics problem, with a mechanism for the transfer of energy from the flow to the acoustics. Due to the fundamental physical difference between flow phenomena, like turbulence, and acoustic phenomena, like wave propagation, the splitting of the problem will generally be advantageous, both from a computational point of view, and for purposes of understanding. While considering the split equations, however, it is important to remember that flow and acoustics, in reality, are coupled. The ‘booming’ noise mentioned above, for example, can not appear without the transfer of energy from the acoustics to the flow.

Geometrically speaking, many aero acoustic flows can be divided into 3 regions as in figure 2.1. The *flow region* is dominated by hydrodynamic phenomena. Although acoustic waves are present, the pressure fluctuations will primarily be due to turbulence or larger unsteady features, such as separations. The hydrodynamic pressure fluctuations will dominate, since the energy of the acoustic field is typically only of the order of 1% of the total energy [3]. The *far field* is a region with negligible turbulence, and the mean flow field is typically homogeneous. No sound is being generated in this region, so the only phenomena present is acoustic wave propagation. For small amplitudes and low Mach numbers, this region can be described by a linear, homogeneous wave equation. The *near field* is the overlapping area between the other 2 regions. In this region both hydrodynamics and acoustics are important. As a general rule of thumb, the flow region is about the size of an acoustic wavelength, and the far field starts several acoustic wavelengths out.

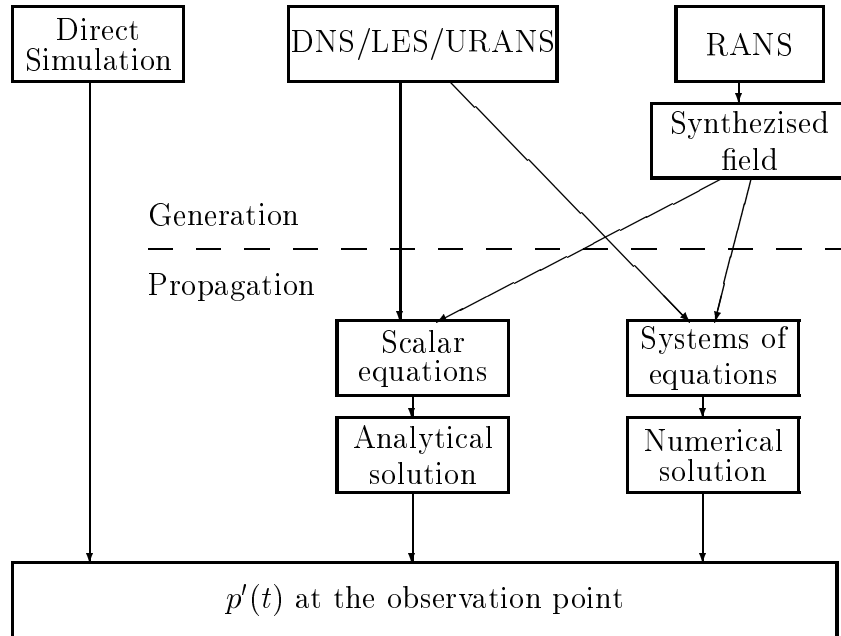


Figure 2.2: Overview of CAA methods

Basically all literature on aero acoustics deal with the far field sound, i.e. the modeling or computation of the acoustic waves leaving the flow region. The main approaches are summarized in figure 2.2, and will be reviewed in coming sections. As can be seen in the figure, most methods make a distinction between sound generation and propagation. When interested in the sound in the flow region, however, this distinction may not exist, and many of these models will not work.

2.1 Direct Simulation

Direct Simulation (DS), i.e. to solve the governing equations without modeling, is perhaps the most straightforward and intuitive way to compute sound. Since the governing equations completely describe all motions in a fluid, the solution to these equations will include acoustic phenomena.

The equations governing motion and energy in a compressible fluid are [4],

when written on conservative form, the continuity equation,

$$\frac{\partial \rho}{\partial t} + \frac{\partial \rho u_i}{\partial x_i} = 0 \quad (2.1)$$

the momentum equation,

$$\frac{\partial \rho u_i}{\partial t} + \frac{\partial \rho u_i u_j}{\partial x_j} = -\frac{\partial p}{\partial x_i} + \frac{\partial \tau_{ij}}{\partial x_j} \quad (2.2)$$

and the energy equation,

$$\frac{\partial \rho e_o}{\partial t} + \frac{\partial (\rho e_o u_j + p u_j)}{\partial x_j} = \frac{\partial (\tau_{ij} u_i - q_j)}{\partial x_j} \quad (2.3)$$

where $e_o = e + u_i u_i / 2$ is the total internal energy.

To close this set of equations, some constitutive and thermodynamic relations are needed. The viscous stress tensor τ_{ij} for a Newtonian fluid is given by

$$\tau_{ij} = \mu \left(\frac{\partial u_i}{\partial x_j} + \frac{\partial u_j}{\partial x_i} - \frac{2}{3} \frac{\partial u_k}{\partial x_k} \delta_{ij} \right) \quad (2.4)$$

The heat flux q_i is normally modeled by Fourier's heat law

$$q_i = -\frac{c_p \mu}{Pr} \frac{\partial T}{\partial x_i} \quad (2.5)$$

Most gases can be assumed to be thermally perfect, which implies

$$p = \rho R T \quad (2.6)$$

and $e = e(T)$, $h = h(T)$, $h = e + RT$ where R is a constant. If the gas can also be assumed to be calorically perfect, the internal energy and enthalpy can be written as

$$\begin{aligned} e &= c_v T \\ h &= c_p T \\ c_p &= c_v + R \end{aligned} \quad (2.7)$$

where the specific heats, c_p and c_v , are constants. The ratio of the specific heats is $\gamma = c_p / c_v$.

Although this set of equations is a complete description of the field, it has only been solved for academic test cases due to the extreme computational cost. The whole range of length scales, from the Kolmogorov microscale to the distance traveled by the sound waves, needs to be resolved, which makes DS more expensive than traditional, incompressible, Direct Numerical Simulation (DNS). In traditional DNS, the largest length scale is roughly the integral scale L , while the smallest is the Kolmogorov microscale η . This leads to an estimated L/η points in each direction, and since the size of the timestep is coupled to the grid size via the CFL number, the total number of degrees of freedom (DOF) becomes $(L/\eta)^4$. The ratio of the length scales L/η can be shown to be proportional¹ to $Re_L^{3/4}$ [5], where $Re_L = u_{rms}L/\nu$ is a turbulent Reynolds number. The number of DOF in traditional DNS then becomes proportional to Re_L^3 .

In DS, the largest length scale is not the integral scale, but rather the distance between the noise sources and the observer location. Assuming a very compact problem, this distance can be estimated to being of the order of the wavelength λ of the sound waves. The number of DOF then becomes $(\lambda/\eta)^4$, or $(\lambda/L)^4$ times larger than for DNS. The wavelength is $\lambda = a/f$, and the frequency of a turbulent fluctuation is $f \sim u_{rms}/L$, which yields $(\lambda/L)^4 \sim (a/u_{rms})^4 = 1/M_t^4$, with M_t being the turbulent Mach number. Hence, the number of DOF in DS scales as $M_t^{-4}Re_L^3$, which certainly prohibits DS to be anything but an academic tool in the foreseeable future.

The fact that different physical phenomena have to be resolved also puts very high requirements on the numerics. In DNS it is common to use schemes of high order, but in DS not only the order of the scheme, but also the characteristics when propagating waves, is important. This typically means that high-quality grids with less than 1% stretching are needed, along with very accurate numerical schemes. No matter how slowly the grid is stretched, the fact that at least 4 points per wavelength are needed to resolve a wave puts an upper limit on the cell size that applies in the whole computational domain. Larsson [1] discusses some issues regarding numerical requirements when resolving wave motion. For further reading, Tam and Webb [6] and Bogey and Bailly [7] offer more details.

The boundary conditions of a DS are also critical; they have to minimize the reflection of acoustic waves back into the domain, or in some cases cor-

¹This is true only for infinite Reynolds number, but it will do for the purposes of estimation.

rectly model the acoustic impedance. Non-reflecting boundary conditions are either based on the local characteristic variables, as for example those by Thompson [8] and Poinso and Lele [9], or on an asymptotic analysis far from the source, as those by for example Bayliss and Turkel [10] and Tam and Webb [6]. Since no boundary conditions are non-reflecting for a discrete, non-linear, case, the use of a buffer zone, that slowly dampens oscillations close to the boundary, was suggested by Colonius *et al* [11]. The main draw-back with buffer zones is the computational effort involved, since they typically increase the number of grid points by 20 – 40%. Billson [12] offers a more complete review of boundary conditions for CAA.

2.1.1 Large Scale Simulation

A Direct Simulation solves the compressible Navier-Stokes equations without modeling, and hence solves for the acoustic field as well as the turbulence. If traditional DNS, which solves for the turbulence but not the acoustics, is considered a subset of DS, one could imagine another subset that solves for the acoustics, but not the turbulence. This subset lacks a descriptive name, but the name given to it by Mankbadi *et al* [13], *Large Scale Simulation* (LSS), will be used here.

In essence, all methodologies that compute the sound field directly, but that do not resolve all of the turbulence, can be considered to belong to LSS. For example, a compressible Unsteady RANS (URANS), where the pressure fluctuations are recorded during the simulation and taken as the sound field, would belong to the LSS category of methodologies. Apart from the study by Mankbadi *et al*, LSS has been performed by for example Shieh and Morris [14]. The main strength of LSS is, of course, that the computational cost is considerably smaller than in DS, while still computing the sound field directly. Since the small scales of the turbulence are believed to have only a very modest influence on the radiated sound, LSS is a promising approach.

2.1.2 Wave Extrapolation Methods

The Large Scale Simulation decreases the computational cost by not resolving the turbulence. Another way of decreasing the computational effort is to minimize the computational domain. If the domain extends to a point where

the sound waves leaving the domain can be described by a simpler wave equation, this simpler equation can be used to ‘extrapolate’ the sound waves farther out into the far field (hence the name *Wave Extrapolation Methods*).

The most common method is the Kirchhoff method, which makes use of the general solution² to the linear wave equation, to analytically ‘extrapolate’ the sound waves into the far field. By utilizing this methodology, the computational domain of the DS, or the LSS, needs only be large enough to include all non-linear effects. The Kirchhoff method is described by for example Billson [12].

A more recent development is to use Ffowcs Williams and Hawkings’ [15] equation as a Wave Extrapolation Method, which was done by Gloerfelt *et al* [16]. The advantage of this method is that the domain can be made even smaller, compared to the Kirchhoff method.

2.2 Scalar Equations

The field of aero acoustics was pioneered by Lighthill’s first paper [17], in which he derived a scalar equation for the propagation of sound waves. Other authors have later followed the same basic approach to come up with various scalar equations. All the approaches start with the Navier-Stokes equations, and proceed by rewriting the equations to get *one* equation for an acoustic variable, with a wave operator on the left hand side.

The primary strength of these scalar equations is that most of them can be solved analytically, which has proven instrumental in producing estimations of the radiated sound. The primary weakness of these methods is the fact that much of the physics is left out, since acoustic wave propagation only can be described by a scalar equation under some circumstances.

²Equation (2.32), without the volume integral, is the equation used in the Kirchhoff Wave Extrapolation Method.

2.2.1 Lighthill's Equation

Differentiating the continuity equation (2.1) with respect to time, and subtracting the divergence of the momentum equation (2.2), yields a scalar equation

$$\frac{\partial^2 \rho}{\partial t^2} - \frac{\partial^2 \rho u_i u_j}{\partial x_i \partial x_j} = \frac{\partial^2 p}{\partial x_i^2} - \frac{\partial^2 \tau_{ij}}{\partial x_i \partial x_j} \quad (2.8)$$

In order to get a wave equation for the density, the convective term is moved to the right hand side, and a term $-a_\infty^2 \partial^2 \rho / \partial x_i^2$ is added to both sides of the equation. The result is the famous Lighthill's equation

$$\frac{\partial^2 \rho}{\partial t^2} - a_\infty^2 \frac{\partial^2 \rho}{\partial x_i^2} = \frac{\partial^2 T_{ij}}{\partial x_i \partial x_j} \quad (2.9)$$

where $T_{ij} = \rho u_i u_j - \tau_{ij} + (p - a_\infty^2 \rho) \delta_{ij}$ is called the Lighthill tensor. Since no assumptions were made, this is an exact equation, and hence, it includes all physics such as wave propagation, convection, and diffusion. If the right hand side is assumed to be known, and independent of the left hand side, equation (2.9) can be viewed as an inhomogeneous wave equation in an isotropic medium at rest.

This last statement is important, and too often overlooked. If the right hand side is *assumed* to be a source term, all the physics of the propagation must exist on the left hand side. The left hand side is an ordinary wave operator, and hence such wave propagation is the only propagation that is described by Lighthill's equation. Another way of saying the same thing is that only for problems where the isotropic wave operator correctly describes the propagation of sound, will Lighthill's equation make physical sense.

If the right hand side is assumed known, and independent of the left hand side, the equation can be solved analytically to

$$\rho(\mathbf{x}, t) - \rho_o = \frac{1}{4\pi a_\infty^2} \int_\infty \frac{1}{r} \frac{\partial^2 T_{ij}}{\partial y_i \partial y_j} dV(\mathbf{y}) = \frac{1}{4\pi a_\infty^2} \frac{\partial^2}{\partial x_i \partial x_j} \int_\infty \frac{T_{ij}}{r} dV(\mathbf{y}) \quad (2.10)$$

where $T_{ij} = T_{ij}(\mathbf{y}, \tau)$, $r = |\mathbf{x} - \mathbf{y}|$, and ρ_o is a constant of integration. $\tau = t - r/a_\infty$ is the *retarded time*, i.e. the time at which the source radiates a fluctuation that reaches the observer at t .

The first form of the solution is the perhaps most straightforward one, where the source term, as it appears in Lighthill's equation, is to be integrated over

all space. The second form is equivalent to the first one on an unbounded domain, and it is, in fact, the form that Lighthill originally used. The reason to this is that this form simplifies estimations of the radiated sound, the main use of acoustic equations several decades ago.

2.2.2 Ffowcs Williams and Hawkings' Equation

If present, solid surfaces will alter the sound generation and radiation. The surfaces may act as sources of sound, and they will reflect and diffract the radiated sound, changing the radiation characteristics of the flow. The first attempt at finding a theory for these phenomena was published by Curle [18], and Ffowcs Williams and Hawkings [15] extended Curle's theory to include surfaces in arbitrary motion. In this review, the contribution of Ffowcs Williams and Hawkings will be analyzed before that of Curle, since the derivation of the former is more mathematically rigorous. Curle's equation will be presented in section 2.2.3.

The main approach of Ffowcs Williams and Hawkings is to rewrite the governing equations using generalized functions, to make the equations valid over all space. A wave equation is then constructed, and the solution of this wave equation is obtained by convolution by a Green's function.

Consider the flow around a body, where the surface of the body may be porous. Following Crighton [19], the surface S of the body is defined by the function f as

$$\begin{cases} f(\mathbf{x}, t) < 0 & , \text{ inside } S \\ f(\mathbf{x}, t) = 0 & , \text{ on } S \\ f(\mathbf{x}, t) > 0 & , \text{ outside } S \end{cases} \quad (2.11)$$

When moving with the surface velocity v_i , f satisfies the relation

$$\frac{\partial f}{\partial t} + v_i \frac{\partial f}{\partial x_i} = 0 \quad (2.12)$$

which will be used later to eliminate $\partial f / \partial t$.

For reasons that will be explained later on, a term $\partial \rho_\infty / \partial t = 0$ is added to the continuity equation (2.1), yielding

$$\frac{\partial \rho - \rho_\infty}{\partial t} + \frac{\partial \rho u_i}{\partial x_i} = 0 \quad (2.13)$$

Since ρ_∞ is a constant, this will not change the equation. Multiplying all terms by the Heaviside step function $H(f)$ yields

$$\frac{\partial \rho - \rho_\infty}{\partial t} H(f) + \frac{\partial \rho u_i}{\partial x_i} H(f) = 0 \quad (2.14)$$

or equivalently, when utilizing the rule for differentiation of products,

$$\frac{\partial(\rho - \rho_\infty)H(f)}{\partial t} - (\rho - \rho_\infty)\frac{\partial H(f)}{\partial t} + \frac{\partial \rho u_i H(f)}{\partial x_i} - \rho u_i \frac{\partial H(f)}{\partial x_i} = 0 \quad (2.15)$$

Moving the second and fourth terms in equation (2.15) to the right hand side, and simplifying, yields

$$\begin{aligned} & \frac{\partial(\rho - \rho_\infty)H(f)}{\partial t} + \frac{\partial \rho u_i H(f)}{\partial x_i} = \\ & = (\rho - \rho_\infty)\frac{\partial H(f)}{\partial t} + \rho u_i \frac{\partial H(f)}{\partial x_i} \\ & = \left[(\rho - \rho_\infty)\frac{\partial f}{\partial t} + \rho u_i \frac{\partial f}{\partial x_i} \right] \delta(f) \\ & = [\rho_\infty v_i + \rho(u_i - v_i)] \frac{\partial f}{\partial x_i} \delta(f) \\ & = Q |\nabla f| \delta(f) \end{aligned} \quad (2.16)$$

where the second last step uses relation (2.12) to eliminate $\partial f / \partial t$, the last step uses $\partial f / \partial x_i = n_i |\nabla f|$, and $Q = (\rho_\infty v_i + \rho(u_i - v_i))n_i$. Equation (2.16) is the continuity equation for the function $(\rho - \rho_\infty)H(f)$, a function that is equal to the density fluctuation outside the surface S , and equal to 0 inside of it. The source term Q exists on S , and accounts for all boundary effects.

So what is the significance of the ρ_∞ -term? The reason for rewriting the equation is to get source terms that account for the boundary effects, so that the equation is valid over an infinite space with no boundaries. The second part of Q clearly acts as a source of matter when $u_i \neq v_i$, i.e. when there is a mass flux through the surface, just as expected. The first part, however, acts as a source when the surface is moving, and this effect would have been lost if the ρ_∞ -term had not been added. The reason is simply that a moving surface is a source of density fluctuations, $\rho - \rho_\infty$, but not of mass in a global sense.

Applying the same methodology to the momentum equation (2.2) yields

$$\frac{\partial \rho u_i H(f)}{\partial t} + \frac{\partial \rho u_i u_j H(f)}{\partial x_j} + \frac{\partial p H(f)}{\partial x_i} - \frac{\partial \tau_{ij} H(f)}{\partial x_j} =$$

$$\begin{aligned}
 &= \rho u_i \frac{\partial H(f)}{\partial t} + \rho u_i u_j \frac{\partial H(f)}{\partial x_j} + p \frac{\partial H(f)}{\partial x_i} - \tau_{ij} \frac{\partial H(f)}{\partial x_j} \\
 &= \left[\rho u_i \frac{\partial f}{\partial t} + \rho u_i u_j \frac{\partial f}{\partial x_j} + p \delta_{ij} \frac{\partial f}{\partial x_j} - \tau_{ij} \frac{\partial f}{\partial x_j} \right] \delta(f) \\
 &= \left[\rho u_i (u_j - v_j) \frac{\partial f}{\partial x_j} + p \delta_{ij} \frac{\partial f}{\partial x_j} - \tau_{ij} \frac{\partial f}{\partial x_j} \right] \delta(f) \\
 &= F_i |\nabla f| \delta(f)
 \end{aligned} \tag{2.17}$$

where $F_i = (\rho u_i (u_j - v_j) + p \delta_{ij} - \tau_{ij}) n_j$. Equation (2.17) is the momentum equation for the generalized function $\rho u_i H(f)$. The source term accounts for the flux of momentum across the surface. In the case of an impermeable surface, F_i reduces to the force exerted by the body on the fluid.

What has been achieved by rewriting the continuity and momentum equations in this way? The original equations ((2.1) and (2.2)) are valid only in the space occupied by the fluid, whereas equations (2.16) and (2.17) are valid throughout all space. The source terms appearing in the latter equations correspond to the boundary conditions that would have been applied to the original ones.

Using the same methodology as when deriving Lighthill's equation (2.9), i.e. taking the time derivative of the continuity equation, subtracting the divergence of the momentum equation, and subtracting a term $a_\infty^2 \partial^2 \rho / \partial x_i^2$, yields a wave equation similar to Lighthill's, but with source terms accounting for the boundary effects,

$$\left[\frac{\partial^2}{\partial t^2} - a_\infty^2 \frac{\partial^2}{\partial x_i^2} \right] (\rho - \rho_\infty) H(f) = \frac{\partial^2 T'_{ij} H(f)}{\partial x_i \partial x_j} - \frac{\partial F_i |\nabla f| \delta(f)}{\partial x_i} + \frac{\partial Q |\nabla f| \delta(f)}{\partial t} \tag{2.18}$$

where $T'_{ij} = \rho u_i u_j - \tau_{ij} + (p - a_\infty^2 (\rho - \rho_\infty)) \delta_{ij} = T_{ij} + a_\infty^2 \rho_\infty \delta_{ij}$.

Equation (2.18) is similar to Lighthill's equation outside S , and it is a trivial identity inside S . Since the boundary effects are included as source terms, it is valid over all space. This means that a solution can be obtained by convolution by a Green's function, although special care has to be taken since the equation consists of distributions, rather than functions.

To solve equation (2.18), some convolution algebra is needed. An equation

$$L_1 \rho = L_2 q \tag{2.19}$$

where L_1 and L_2 are linear differential operators, has a solution

$$\rho(\mathbf{x}, t) = L_2(q * G) = L_2 \int q(\mathbf{y}, \tau) G(\mathbf{x} - \mathbf{y}, t - \tau) d\mathbf{y} d\tau \quad (2.20)$$

where the Green's function G is defined by

$$L_1 G = \delta \quad (2.21)$$

The Green's function for the isotropic wave operator (L_1) is

$$G(\mathbf{r}, \theta) = \frac{\delta(|\mathbf{r}| - a_\infty \theta)}{4\pi a_\infty |\mathbf{r}|} \quad (2.22)$$

According to (2.20), and due to the linearity of the wave equation, the solution of (2.18) is

$$\begin{aligned} \rho(\mathbf{x}, t) - \rho_o &= \\ &= \frac{\partial^2}{\partial x_i \partial x_j} \int_\infty [T'_{ij} H(f)](\mathbf{y}, \tau) \frac{\delta(r - a_\infty(t - \tau))}{4\pi a_\infty r} dV(\mathbf{y}) d\tau \\ &\quad - \frac{\partial}{\partial x_i} \int_\infty [F_i |\nabla f| \delta(f)](\mathbf{y}, \tau) \frac{\delta(r - a_\infty(t - \tau))}{4\pi a_\infty r} dV(\mathbf{y}) d\tau \\ &\quad + \frac{\partial}{\partial t} \int_\infty [Q |\nabla f| \delta(f)](\mathbf{y}, \tau) \frac{\delta(r - a_\infty(t - \tau))}{4\pi a_\infty r} dV(\mathbf{y}) d\tau \end{aligned} \quad (2.23)$$

where ρ_o is a constant of integration that includes ρ_∞ . Note that \mathbf{y} and τ are *independent* variables in equation (2.23), as well as \mathbf{x} and t , of course.

In the case of a moving surface, the source terms and the function f describing the surface, will be best represented in a coordinate system moving with the surface. For the sake of simplicity, the coordinate system \mathbf{y}^* is assumed to be translating with constant velocity v_i relative to \mathbf{y} , and hence

$$y_i = y_i^* + v_i \tau \quad (2.24)$$

For this translation, the Jacobian of the coordinate transformation becomes $J(\mathbf{y}/\mathbf{y}^*) = 1$. Velocities measured in the moving coordinate system are defined by

$$u_i = u_i^* + v_i \quad (2.25)$$

In order to integrate over $d\tau$ and get rid of the $\delta(r - a_\infty(t - \tau))$ function, the variable substitution $g(\tau) = r - a_\infty(t - \tau)$ is used. Since \mathbf{y} is now a function of τ , $r = |\mathbf{x} - \mathbf{y}|$ becomes a function of τ , as well. Differentiating $g(\tau)$ yields $dg = (\partial r / \partial \tau + a_\infty) d\tau$, where $\partial r / \partial \tau$ is

$$\frac{\partial r}{\partial \tau} = \frac{\partial r}{\partial y_j} \frac{\partial y_j}{\partial \tau} = \frac{-2(x_j - y_j)}{2\sqrt{(x_i - y_i)^2}} \frac{\partial y_j}{\partial \tau} = -\frac{x_j - y_j}{r} v_j = -l_j v_j \quad (2.26)$$

where l_j is a unit vector pointing from the source to the observer position. This leads to $dg = (a_\infty - l_j v_j) d\tau$ and

$$\begin{aligned} \rho(\mathbf{x}, t) - \rho_o &= \\ &= \frac{\partial^2}{\partial x_i \partial x_j} \int_\infty [T'_{ij} H(f^*)] (\mathbf{y}^*, \tau) \frac{\delta(g)}{4\pi a_\infty r (a_\infty - l_j v_j)} dV(\mathbf{y}^*) dg \\ &\quad - \frac{\partial}{\partial x_i} \int_\infty [F'_i |\nabla f^*| \delta(f^*)] (\mathbf{y}^*, \tau) \frac{\delta(g)}{4\pi a_\infty r (a_\infty - l_j v_j)} dV(\mathbf{y}^*) dg \\ &\quad + \frac{\partial}{\partial t} \int_\infty [Q^* |\nabla f^*| \delta(f^*)] (\mathbf{y}^*, \tau) \frac{\delta(g)}{4\pi a_\infty r (a_\infty - l_j v_j)} dV(\mathbf{y}^*) dg \quad (2.27) \end{aligned}$$

Integration over dg yields

$$\begin{aligned} \rho(\mathbf{x}, t) - \rho_o &= \\ &= \frac{1}{4\pi a_\infty^2} \frac{\partial^2}{\partial x_i \partial x_j} \int_\infty \frac{T'_{ij} H(f^*)}{r(1 - \frac{l_j v_j}{a_\infty})} dV(\mathbf{y}^*) \\ &\quad - \frac{1}{4\pi a_\infty^2} \frac{\partial}{\partial x_i} \int_\infty \frac{F'_i}{r(1 - \frac{l_j v_j}{a_\infty})} |\nabla f^*| \delta(f^*) dV(\mathbf{y}^*) \\ &\quad + \frac{1}{4\pi a_\infty^2} \frac{\partial}{\partial t} \int_\infty \frac{Q^*}{r(1 - \frac{l_j v_j}{a_\infty})} |\nabla f^*| \delta(f^*) dV(\mathbf{y}^*) \quad (2.28) \end{aligned}$$

where the integrands are to be evaluated at $g = 0$ or, equivalently, $\tau = t - r/a_\infty$. τ is now the *retarded time*, and it is no longer an independent variable.³

The $H(f^*)$ -function in the first integral in (2.28) is non-zero in the fluid, i.e. on the domain V . To integrate over the remaining δ -functions, the following

³The origin of the retarded time in the solution of Lighthill's equation (2.10) can now be seen clearly.

theorem has to be used [19]:

$$\int_{\infty} h(\mathbf{z})\delta(f(\mathbf{z}))dV(\mathbf{z}) = \int_{\Sigma} \frac{h(\hat{\mathbf{z}})}{|\nabla f|}dS(\hat{\mathbf{z}}) \quad (2.29)$$

The left hand side of equation (2.29) is a volume integral including a Dirac delta function, which has an argument $f(\mathbf{z})$ that is zero on the surface Σ , i.e. $f(\hat{\mathbf{z}}) = 0$. According to the theorem, this volume integral is equal to a surface integral of the function h divided by $|\nabla f|$, over all points $\hat{\mathbf{z}}$.⁴

Applying this to equation (2.28) yields

$$\begin{aligned} \rho(\mathbf{x}, t) - \rho_o &= \\ &= \frac{1}{4\pi a_{\infty}^2} \frac{\partial^2}{\partial x_i \partial x_j} \int_V \frac{T_{ij}^*}{r(1 - \frac{l_j v_i}{a_{\infty}})} dV(\mathbf{y}^*) \\ &\quad - \frac{1}{4\pi a_{\infty}^2} \frac{\partial}{\partial x_i} \int_S \frac{F_i^*}{r(1 - \frac{l_j v_j}{a_{\infty}})} dS(\mathbf{y}^*) \\ &\quad + \frac{1}{4\pi a_{\infty}^2} \frac{\partial}{\partial t} \int_S \frac{Q^*}{r(1 - \frac{l_j v_j}{a_{\infty}})} dS(\mathbf{y}^*) \end{aligned} \quad (2.30)$$

The only remaining task is to derive expressions for the source terms when measured in the moving coordinate system. From definition (2.24) one gets $\partial/\partial y_i = \partial/\partial y_i^*$. Since the surface velocity v_i is constant, definition (2.25) yields $\partial u_i = \partial u_i^*$, and hence $\tau_{ij} = \tau_{ij}^*$. The source terms then become

$$\begin{aligned} T_{ij}^* &= \rho(u_i^* + v_i)(u_j^* + v_j) - \tau_{ij}^* + \left(p - a_{\infty}^2(\rho - \rho_{\infty})\right) \delta_{ij} \\ F_i^* &= \left(\rho(u_i^* + v_i)u_j^* + p\delta_{ij} - \tau_{ij}^*\right) n_j \\ Q^* &= (\rho_{\infty}v_i + \rho u_i^*) n_i \end{aligned} \quad (2.31)$$

In equation (2.30), the first source term represents quadrupole sources due to fluctuating stresses in the fluid, the second term represents dipole sources due to fluctuating forces on the surfaces, and the third term represents monopole sources due to fluctuating mass fluxes through the surfaces. For impermeable surfaces, $u_i^* \equiv 0$ on the surface, and hence the surface source terms reduce to $F_i^* = (p\delta_{ij} - \tau_{ij}^*)n_j$ and $Q^* = \rho_{\infty}v_i n_i$. When the surfaces are also stationary, the monopole term Q^* disappears completely.

⁴This theorem can be proven by a coordinate transformation, where one of the new coordinates is normal to the surface Σ , and the others are tangential to Σ . The integration can then be taken over the coordinate normal to the surface.

2.2.3 Curle's Equation

As was mentioned in the previous section, Curle [18] was the first to derive an acoustic equation that takes the effects of solid boundaries into account.

The general solution of the inhomogeneous wave equation (2.9) on a bounded domain is

$$\begin{aligned} \rho(\mathbf{x}, t) - \rho_o &= \frac{1}{4\pi a_\infty^2} \int_V \frac{1}{r} \frac{\partial^2 T_{ij}}{\partial y_i \partial y_j} dV(\mathbf{y}) \\ &\quad - \frac{1}{4\pi} \int_S \left(\frac{1}{r} \frac{\partial \rho}{\partial n} + \frac{1}{r^2} \frac{\partial r}{\partial n} \rho + \frac{1}{a_\infty r} \frac{\partial r}{\partial n} \frac{\partial \rho}{\partial \tau} \right) dS(\mathbf{y}) \end{aligned} \quad (2.32)$$

where n is the surface normal pointing towards the fluid.

Curle seeks a solution where the double divergence is taken outside the integral sign. Although not stated in [18], he manipulates the volume integral in equation (2.32) on the convolution integral that leads to equation (2.32). Similar to the derivation in section 2.2.2, Curle thinks of the volume integral in (2.32) as

$$\frac{1}{4\pi a_\infty^2} \int_V \frac{1}{r} \frac{\partial^2 T_{ij}}{\partial y_i \partial y_j} dV(\mathbf{y}) = \int_\infty \int_V \frac{\partial^2 T_{ij}}{\partial y_i \partial y_j}(\mathbf{y}, \tau) G(\mathbf{x} - \mathbf{y}, t - \tau) dV(\mathbf{y}) d\tau \quad (2.33)$$

where $G(\mathbf{x} - \mathbf{y}, t - \tau)$ is the Green's function given by (2.22), and \mathbf{y} and τ are independent variables. He then uses the divergence theorem to get

$$\begin{aligned} &\frac{1}{4\pi a_\infty^2} \int_V \frac{1}{r} \frac{\partial^2 T_{ij}}{\partial y_i \partial y_j} dV(\mathbf{y}) = \\ &= \int_\infty \int_V \frac{\partial}{\partial y_i} \left[\frac{\partial T_{ij}(\mathbf{y}, \tau)}{\partial y_j} G(\mathbf{x} - \mathbf{y}, t - \tau) \right] dV(\mathbf{y}) d\tau \\ &\quad - \int_\infty \int_V \frac{\partial T_{ij}(\mathbf{y}, \tau)}{\partial y_j} \frac{\partial G(\mathbf{x} - \mathbf{y}, t - \tau)}{\partial y_i} dV(\mathbf{y}) d\tau \\ &= \int_\infty \int_S -n_i \frac{\partial T_{ij}(\mathbf{y}, \tau)}{\partial y_j} G(\mathbf{x} - \mathbf{y}, t - \tau) dS(\mathbf{y}) d\tau \\ &\quad + \int_\infty \int_V \frac{\partial T_{ij}(\mathbf{y}, \tau)}{\partial y_j} \frac{\partial G(\mathbf{x} - \mathbf{y}, t - \tau)}{\partial x_i} dV(\mathbf{y}) d\tau \end{aligned} \quad (2.34)$$

where the last step uses the fact that $\partial G / \partial y_i = -\partial G / \partial x_i$, since the argument of G is $\mathbf{x} - \mathbf{y}$. Since \mathbf{y} and τ are *independent* variables, $\partial / \partial x_i$ can be taken

outside the integral. Repeating a similar process for the volume integral in (2.34) yields

$$\begin{aligned}
 & \frac{1}{4\pi a_\infty^2} \int_V \frac{1}{r} \frac{\partial^2 T_{ij}}{\partial y_i \partial y_j} dV(\mathbf{y}) = \\
 & = \int_\infty \int_S -n_i \frac{\partial T_{ij}(\mathbf{y}, \tau)}{\partial y_j} G(\mathbf{x} - \mathbf{y}, t - \tau) dS(\mathbf{y}) d\tau \\
 & + \frac{\partial}{\partial x_i} \int_\infty \int_V \frac{\partial}{\partial y_j} [T_{ij}(\mathbf{y}, \tau) G(\mathbf{x} - \mathbf{y}, t - \tau)] dV(\mathbf{y}) d\tau \\
 & - \frac{\partial}{\partial x_i} \int_\infty \int_V T_{ij}(\mathbf{y}, \tau) \frac{\partial G(\mathbf{x} - \mathbf{y}, t - \tau)}{\partial y_j} dV(\mathbf{y}) d\tau \\
 & = \int_\infty \int_S -n_i \frac{\partial T_{ij}(\mathbf{y}, \tau)}{\partial y_j} G(\mathbf{x} - \mathbf{y}, t - \tau) dS(\mathbf{y}) d\tau \\
 & + \frac{\partial}{\partial x_i} \int_\infty \int_S -n_j T_{ij}(\mathbf{y}, \tau) G(\mathbf{x} - \mathbf{y}, t - \tau) dS(\mathbf{y}) d\tau \\
 & \frac{\partial^2}{\partial x_i \partial x_j} \int_\infty \int_V T_{ij}(\mathbf{y}, \tau) G(\mathbf{x} - \mathbf{y}, t - \tau) dV(\mathbf{y}) d\tau \tag{2.35}
 \end{aligned}$$

Integrating over the δ -function in G , using the same methodology as in section 2.2.2, and rearranging, yields

$$\begin{aligned}
 & \frac{1}{4\pi a_\infty^2} \int_V \frac{1}{r} \frac{\partial^2 T_{ij}}{\partial y_i \partial y_j} dV(\mathbf{y}) = \\
 & = \frac{1}{4\pi a_\infty^2} \frac{\partial^2}{\partial x_i \partial x_j} \int_V \frac{T_{ij}(\mathbf{y}, \tau)}{r} dV(\mathbf{y}) \\
 & - \frac{1}{4\pi a_\infty^2} \frac{\partial}{\partial x_i} \int_S n_j \frac{T_{ij}(\mathbf{y}, \tau)}{r} dS(\mathbf{y}) \\
 & - \frac{1}{4\pi a_\infty^2} \int_S \frac{n_i}{r} \frac{\partial T_{ij}(\mathbf{y}, \tau)}{\partial y_j} dS(\mathbf{y}) \tag{2.36}
 \end{aligned}$$

where $\tau = t - r/a_\infty$ is now the retarded time.

Curle then rewrites the surface integral in (2.32) to get it on a form similar to (2.36) by using the relations

$$\frac{\partial}{\partial n} = n_i \frac{\partial}{\partial y_i} \quad , \quad \frac{\partial}{\partial x_i} \left[\frac{f(\tau)}{r} \right] = - \left[\frac{f}{r^2} + \frac{1}{a_\infty r} \frac{\partial f}{\partial \tau} \right] \frac{\partial r}{\partial x_i} \tag{2.37}$$

where the retarded time has been taken into account. The surface integral becomes

$$\begin{aligned}
 & \int_S \left[\frac{1}{r} \frac{\partial \rho}{\partial n} + \frac{1}{r^2} \frac{\partial r}{\partial n} \rho + \frac{1}{a_\infty r} \frac{\partial r}{\partial n} \frac{\partial \rho}{\partial \tau} \right] dS(\mathbf{y}) = \\
 & = \int_S n_i \left[\frac{1}{r} \frac{\partial \rho}{\partial y_i} + \frac{1}{r^2} \frac{\partial r}{\partial y_i} \rho + \frac{1}{a_\infty r} \frac{\partial r}{\partial y_i} \frac{\partial \rho}{\partial \tau} \right] dS(\mathbf{y}) \\
 & = \int_S n_i \left[\frac{1}{r} \frac{\partial (\rho \delta_{ij})}{\partial y_j} - \frac{1}{r^2} \frac{\partial r}{\partial x_i} \rho - \frac{1}{a_\infty r} \frac{\partial r}{\partial x_i} \frac{\partial \rho}{\partial \tau} \right] dS(\mathbf{y}) \\
 & = \int_S \frac{n_i}{r} \frac{\partial (\rho \delta_{ij})}{\partial y_j} dS(\mathbf{y}) + \frac{\partial}{\partial x_i} \int_S \frac{n_j}{r} \rho \delta_{ij} dS(\mathbf{y}) \tag{2.38}
 \end{aligned}$$

Inserting expressions (2.36) and (2.38) into equation (2.32) yields

$$\begin{aligned}
 \rho(\mathbf{x}, t) - \rho_o &= \frac{1}{4\pi a_\infty^2} \frac{\partial^2}{\partial x_i \partial x_j} \int_V \frac{T_{ij}}{r} dV(\mathbf{y}) \\
 & - \frac{1}{4\pi a_\infty^2} \frac{\partial}{\partial x_i} \int_S \frac{n_j}{r} (T_{ij} + a_\infty^2 \rho \delta_{ij}) dS(\mathbf{y}) \\
 & - \frac{1}{4\pi a_\infty^2} \int_S \frac{n_i}{r} \frac{\partial}{\partial y_j} (T_{ij} + a_\infty^2 \rho \delta_{ij}) dS(\mathbf{y}) \tag{2.39}
 \end{aligned}$$

From the definition of T_{ij} , one gets $T_{ij} + a_\infty^2 \rho \delta_{ij} = \rho u_i u_j - \tau_{ij} + p \delta_{ij}$. This is almost the momentum equation, so the integrand in the last surface integral in (2.39) above can be written

$$\frac{n_i}{r} \frac{\partial}{\partial y_j} (T_{ij} + a_\infty^2 \rho \delta_{ij}) = -\frac{n_i}{r} \frac{\partial \rho u_i}{\partial t} \tag{2.40}$$

Inserting this into equation (2.39) yields

$$\begin{aligned}
 \rho(\mathbf{x}, t) - \rho_o &= \frac{1}{4\pi a_\infty^2} \frac{\partial^2}{\partial x_i \partial x_j} \int_V \frac{T_{ij}}{r} dV(\mathbf{y}) \\
 & - \frac{1}{4\pi a_\infty^2} \frac{\partial}{\partial x_i} \int_S \frac{n_j}{r} (\rho u_i u_j + p \delta_{ij} - \tau_{ij}) dS(\mathbf{y}) \\
 & + \frac{1}{4\pi a_\infty^2} \frac{\partial}{\partial t} \int_S \frac{\rho u_i n_i}{r} dS(\mathbf{y}) \tag{2.41}
 \end{aligned}$$

For solid surfaces, the velocity on the surface is zero. This yields Curle's final result

$$\rho(\mathbf{x}, t) - \rho_o = \frac{1}{4\pi a_\infty^2} \frac{\partial^2}{\partial x_i \partial x_j} \int_V \frac{T_{ij}}{r} dV(\mathbf{y}) - \frac{1}{4\pi a_\infty^2} \frac{\partial}{\partial x_i} \int_S \frac{n_j}{r} (p\delta_{ij} - \tau_{ij}) dS(\mathbf{y}) \quad (2.42)$$

What is the difference between Curle's and Ffowcs Williams and Hawkings' equations, expect for the fact that the latter takes surface motion into account? A comparison between equations (2.41) and (2.30), with the surface velocity $v_i = 0$ in (2.30) (and hence $u_i = u_i^*$), reveals that the only difference is the $a_\infty^2 \rho_\infty \delta_{ij}$ -term in T_{ij}^* . For stationary sources, however, this term will only add a constant that can be absorbed in ρ_o , and Curle's and Ffowcs Williams and Hawkings' equations are then equal to each other.

The real difference between Curle's and Ffowcs Williams and Hawkings' contributions is the more mathematically rigorous derivation of the latter. One of the main contributions by Ffowcs Williams and Hawkings, although not included here, was the estimations of the radiated sound from surfaces moving at velocities close to the speed of sound, and these predictions were made possible by the more mathematical approach.

2.2.4 Phillips' Equation

Lighthill, Curle, and Ffowcs Williams and Hawkings all rewrote the governing equations to get an isotropic wave operator on the left hand side, taking all remaining terms as source terms. This implicitly assumes that the isotropic wave operator correctly describes the propagation of sound waves, and this is true only for flows with zero mean motion, and constant mean density and temperature. For all cases when this is not true, some propagation must be included in the right hand side of the equation.

Phillips [20] rewrote the governing equations to get a more general wave operator on the left hand side. The idea behind this is that if all propagation is included in the left hand side, the terms on the right hand side must be true source terms.

The continuity equation (2.1) can be written as

$$\frac{1}{\rho} \frac{d\rho}{dt} + \frac{\partial u_i}{\partial x_i} = 0 \quad (2.43)$$

where the convective time derivative $d/dt = \partial/\partial t + u_j \partial/\partial x_j$ has been introduced to simplify notation. Since $\rho = \rho(p, s)$, this can be written as

$$\frac{1}{\rho} \left[\left. \frac{\partial \rho}{\partial p} \right|_s \frac{dp}{dt} + \left. \frac{\partial \rho}{\partial s} \right|_p \frac{ds}{dt} \right] + \frac{\partial u_i}{\partial x_i} = 0 \quad (2.44)$$

The second law of thermodynamics can be written as [21]

$$ds = \frac{c_v}{T} dT - \frac{1}{\rho^2} \left. \frac{\partial p}{\partial T} \right|_\rho d\rho \quad (2.45)$$

which yields

$$\begin{aligned} \left. \frac{\partial s}{\partial \rho} \right|_p &= \frac{c_v}{T} \left. \frac{\partial T}{\partial \rho} \right|_p - \frac{1}{\rho^2} \left. \frac{\partial p}{\partial T} \right|_\rho \\ &= -\frac{c_v}{T} \frac{p}{\rho^2 R} - \frac{\rho R}{\rho^2} \\ &= -\frac{1}{\rho} (c_v + R) \\ &= -\frac{c_p}{\rho} \end{aligned} \quad (2.46)$$

where the perfect gas relations (2.6) and (2.7) have been utilized. The speed of sound is defined by

$$a^2 = \left. \frac{\partial p}{\partial \rho} \right|_s = \frac{\gamma p}{\rho} \quad (2.47)$$

Using these relations, the continuity equation (2.44) can be rewritten as

$$\frac{1}{\gamma p} \frac{dp}{dt} - \frac{1}{c_p} \frac{ds}{dt} + \frac{\partial u_i}{\partial x_i} = 0 \quad (2.48)$$

or equivalently, using the rule for differentiation of the log-function,

$$\frac{1}{\gamma} \frac{d}{dt} \left(\log \frac{p}{p_o} \right) - \frac{1}{c_p} \frac{ds}{dt} + \frac{\partial u_i}{\partial x_i} = 0 \quad (2.49)$$

where p_o is an arbitrary reference pressure.

The momentum equation (2.2) can be expanded to

$$\frac{du_i}{dt} = \frac{\partial u_i}{\partial t} + u_j \frac{\partial u_i}{\partial x_j} = -\frac{1}{\rho} \frac{\partial p}{\partial x_i} + \frac{1}{\rho} \frac{\partial \tau_{ij}}{\partial x_j} \quad (2.50)$$

Using the definition of the speed of sound, and the rule for differentiation of the log-function, the pressure term can be rewritten to

$$-\frac{1}{\rho} \frac{\partial p}{\partial x_i} = -\frac{a^2}{\gamma p} \frac{\partial p}{\partial x_i} = -\frac{a^2}{\gamma} \frac{\partial}{\partial x_i} \left(\log \frac{p}{p_o} \right) \quad (2.51)$$

In a spirit similar to that used when deriving Lighthill's equation, the divergence of the momentum equation is subtracted from the *convective* time derivative of the continuity equation, inserting relation (2.51) in the process.

$$\begin{aligned} \frac{1}{\gamma} \frac{d^2}{dt^2} \left(\log \frac{p}{p_o} \right) - \frac{\partial}{\partial x_i} \left[\frac{a^2}{\gamma} \frac{\partial}{\partial x_i} \left(\log \frac{p}{p_o} \right) \right] = \\ \frac{\partial}{\partial x_i} \left(\frac{du_i}{dt} \right) - \frac{d}{dt} \left(\frac{\partial u_i}{\partial x_i} \right) - \frac{\partial}{\partial x_i} \left(\frac{1}{\rho} \frac{\partial \tau_{ij}}{\partial x_j} \right) + \frac{d}{dt} \left(\frac{1}{c_p} \frac{ds}{dt} \right) \end{aligned} \quad (2.52)$$

The first two terms on the right hand side are expanded to

$$\frac{\partial}{\partial x_i} \left(\frac{du_i}{dt} \right) - \frac{d}{dt} \left(\frac{\partial u_i}{\partial x_i} \right) = \frac{\partial u_i}{\partial x_j} \frac{\partial u_j}{\partial x_i} \quad (2.53)$$

Neglecting the viscous term, assuming isentropic flow, and introducing the variable $\Pi = 1/\gamma \log(p/p_o)$, yields Phillips' equation

$$\frac{d^2 \Pi}{dt^2} - \frac{\partial}{\partial x_i} \left(a^2 \frac{\partial \Pi}{\partial x_i} \right) = \frac{\partial u_i}{\partial x_j} \frac{\partial u_j}{\partial x_i} \quad (2.54)$$

The left hand side of Phillips' equation governs wave propagation in a non-stationary flow with varying speed of sound. For low Mach number applications, the speed of sound is fairly uniform throughout the domain, and may be taken as constant. Since more physics, compared to Lighthill's, Curle's or Ffowcs Williams and Hawkings' equations, are included in the wave operator, the right hand side is a better representation of the actual sources of sound. The downsides, however, are primarily that Phillips' equation can not be solved analytically for a general case, and that wave propagation through shear layers is not taken into account. The latter fact was pointed out by, for example, Doak [22], and will be explained in section 2.2.5.

2.2.5 Lilley's Equation

Lilley [23] realized that Phillips' wave operator is not correct in a sheared flow, and fixed this problem by further manipulations of Phillips' equation. Taking the convective time derivative of equation (2.54) yields

$$\frac{d}{dt} \left[\frac{d^2 \Pi}{dt^2} - \frac{\partial}{\partial x_i} \left(a^2 \frac{\partial \Pi}{\partial x_i} \right) \right] = 2 \frac{\partial u_j}{\partial x_i} \frac{d}{dt} \left(\frac{\partial u_i}{\partial x_j} \right) \quad (2.55)$$

To simplify the right hand side, one expands

$$\begin{aligned} \frac{d}{dt} \left(\frac{\partial u_i}{\partial x_j} \right) &= \frac{\partial}{\partial t} \left(\frac{\partial u_i}{\partial x_j} \right) + u_k \frac{\partial}{\partial x_k} \left(\frac{\partial u_i}{\partial x_j} \right) \\ &= \frac{\partial}{\partial x_j} \left(\frac{\partial u_i}{\partial t} \right) + \frac{\partial}{\partial x_j} \left(u_k \frac{\partial u_i}{\partial x_k} \right) - \frac{\partial u_i}{\partial x_k} \frac{\partial u_k}{\partial x_j} \\ &= \frac{\partial}{\partial x_j} \left(\frac{du_i}{dt} \right) - \frac{\partial u_i}{\partial x_k} \frac{\partial u_k}{\partial x_j} \\ &= \frac{\partial}{\partial x_j} \left(-a^2 \frac{\partial \Pi}{\partial x_i} \right) - \frac{\partial u_i}{\partial x_k} \frac{\partial u_k}{\partial x_j} \end{aligned} \quad (2.56)$$

where the last step uses Phillips' momentum equation (2.50) when neglecting viscosity, relation (2.51), and the definition of Π . Inserting this into (2.55) yields

$$\frac{d}{dt} \left[\frac{d^2 \Pi}{dt^2} - \frac{\partial}{\partial x_i} \left(a^2 \frac{\partial \Pi}{\partial x_i} \right) \right] = -2 \frac{\partial u_j}{\partial x_i} \frac{\partial}{\partial x_j} \left(a^2 \frac{\partial \Pi}{\partial x_i} \right) - 2 \frac{\partial u_j}{\partial x_i} \frac{\partial u_i}{\partial x_k} \frac{\partial u_k}{\partial x_j} \quad (2.57)$$

The right hand side of equation (2.57) stems from the source term in Phillips' equation. The first term includes Π , and hence that term is *not* a source term. The term is non-zero only in sheared flows, which is why Phillips' equation is not valid in those flows.

Rearranging equation (2.57) to get all terms involving Π on the left hand side yields Lilley's equation

$$\frac{d}{dt} \left[\frac{d^2 \Pi}{dt^2} - \frac{\partial}{\partial x_i} \left(a^2 \frac{\partial \Pi}{\partial x_i} \right) \right] + 2 \frac{\partial u_j}{\partial x_i} \frac{\partial}{\partial x_j} \left(a^2 \frac{\partial \Pi}{\partial x_i} \right) = -2 \frac{\partial u_i}{\partial x_j} \frac{\partial u_j}{\partial x_k} \frac{\partial u_k}{\partial x_i} \quad (2.58)$$

The left hand side of Lilley's equation (2.58) correctly represents wave propagation through shear layers with a spatially varying speed of sound, which

makes it the most general scalar wave equation. Due to its complexity, it is impossible to solve analytically, which has limited its use.

2.2.6 Discussion on Scalar Equations

The scalar equations, often called *acoustic analogies*, were generally derived for the purpose of estimations of the radiated sound from jets or propellers and fans. With the recent increases in computational power, these equations have found new use as tools in CAA, partly because of their relative simplicity and, primarily, because of the fact that analytical solutions are available. The expression ‘relative simplicity’ here refers to the fact that these equations are wave equations that do not include hydrodynamic phenomena, and should not be interpreted as simplicity in understanding when and where these equations are valid.

In order to understand the validity of these equations, it is necessary to understand what assumptions were made in the process of derivation. Taking Lighthill’s equation, for example, no assumptions were made when deriving the equation, so it is valid everywhere in every flow, in the sense that the left hand side will always be equal to the right hand side. The analytical solution of Lighthill’s equation is also exact and without assumptions, but only if the right hand side is truly a source term. What, then, is a ‘true source term’? Mathematically speaking, it has to be completely independent of the solution of the equation. This, however, is not strictly the case in any of these scalar equations. In Lighthill’s, Curle’s, and Ffowcs Williams and Hawkings’ equations, the source terms include the density ρ that is being solved for. In *all* the scalar equations, the source terms include velocity, which is linked to the fluctuating pressure and density that are being solved for. Hence, even though no assumptions were made explicitly, all scalar equations mentioned above have *implicitly* assumed that the source terms are, by some measure, good representations of the actual sources of sound in a flow.

So what determines whether the source terms are ‘good representations’ of the actual sources of sound? Again taking Lighthill’s equation as an example, the equation is derived directly from the governing equations, and hence the equation is correct for all physical phenomena, like for example acoustic wave propagation, vortical motion, and convection. But, the only phenomenon described by the left hand side operator is acoustic wave propagation in a uniform medium at rest, meaning that the rest of the physics must be

included on the right hand side of the equation. It follows intuitively that the scalar equations are ‘good representations’ of the important physics when their left hand side operators include all of the essential physics, leaving the source terms to be just that; sources of sound. It also follows immediately that the more complex equations, such as Phillips’ and Lilley’s, are valid over a greater range of flows.

Another consequence of the need for the left hand side operator to describe the propagation of sound waves properly, is that the scalar equations only work for simple geometries. In situations where multiple reflections may occur, such as in ducts, the wave operator needs to take these reflections into account, but no equation presented here does so. For complex geometries, one may have to use a more complex wave operator, such as those described in section 2.3.

When computing the integral solutions to Lighthill’s, Curle’s, or Ffowcs Williams and Hawkings’ equations numerically, Sarkar and Hussaini [24] argued that the original form of the equations will need fairly high resolution in time. They argued that it is wiser to rewrite the equations by assuming that r is much larger than the extent of the sources, and to convert the spatial derivatives into temporal ones as

$$\begin{aligned} \rho(\mathbf{x}, t) - \rho_o &= \frac{1}{4\pi a_\infty^2} \frac{\partial^2}{\partial x_i \partial x_j} \int_\infty \frac{T_{ij}}{r} dV(\mathbf{y}) \\ &\approx \frac{1}{4\pi a_\infty^2} \frac{1}{r} \frac{\partial}{\partial x_i} \int_\infty -\frac{l_j}{a_\infty} \dot{T}_{ij} dV(\mathbf{y}) \\ &\approx \frac{1}{4\pi a_\infty^4} \frac{l_i l_j}{r} \int_\infty \ddot{T}_{ij} dV(\mathbf{y}) \end{aligned} \quad (2.59)$$

since

$$\frac{\partial f(\tau)}{\partial x_i} = -\frac{1}{a_\infty} \frac{\partial r}{\partial x_i} \frac{\partial f}{\partial \tau} = -\frac{l_i}{a_\infty} \dot{f} \quad (2.60)$$

This form of the equation is, according to Sarkar and Hussaini, supposed to require less resolution in time, compared to the original form. The downsides are that the equation is only valid in the far field, and that a symmetric 2nd order tensor needs to be stored, as opposed to a scalar. The author of this thesis is not convinced that this argument is correct, and will touch upon this subject, albeit briefly, in section 8.1.

For further reading on the validity of acoustic analogies, the (fairly critical)

review by Doak [22] offers a deeper physical discussion.

2.3 Systems of Equations

The problems with scalar equations for sound propagation was found to be the fact that the propagation operators were only valid in certain cases. Phillips and Lilley tried to solve this by developing more general scalar equations. These equations, however, can not be solved analytically, and hence they must be solved numerically. If one has to solve *one* equation numerically, one may as well solve a whole system numerically, and this is where the systems of equations come in.

The general idea is to start from the governing equations, and to simplify them for acoustics. This typically means that viscosity can be neglected, and that the equations can be linearized. The gain over DS is that, since the flow and the acoustics are solved for separately, the computational grids and the numerics can be better suited to what is needed to resolve either the flow (turbulence) or the acoustics. This typically means much larger cell sizes in the acoustic simulation, and hence much fewer cells. The gain over the scalar equations is that the equations describe more of the physics, such as the near field region, propagation through shear layers⁵, and reflections at walls. This last fact is crucial in complex geometries. The main downside is that many of the numerical issues associated with DS, such as the necessity of special schemes to resolve waves properly and non-reflective boundary conditions, are issues here as well. Also, *two-way coupling* is removed when the acoustics are separated from the rest of the flow.

2.3.1 Linear Euler Equations

The propagation of sound waves is an almost completely inviscid phenomenon, and hence viscous terms are negligible. Also, since the amplitudes of sound waves are incredibly small, the equations can be linearized. This leads to the linear Euler equations, used by for example Bechara *et al* [25], Bailly *et al* [26], and Billson [12, 27]. Following the derivation of the latter, the linear

⁵Lilley's equation does take propagation through shear layers into account.

Euler equations on conservative form are

$$\frac{\partial \rho'}{\partial t} + \frac{\partial(\rho u_i)'}{\partial x_i} = 0 \quad (2.61)$$

$$\begin{aligned} \frac{\partial(\rho u_i)'}{\partial t} + \frac{\partial}{\partial x_j} [\tilde{u}_j(\rho u_i)' + \tilde{u}_i(\rho u_j)' - \tilde{u}_i \tilde{u}_j \rho' + p' \delta_{ij}] = \\ = -\frac{\partial}{\partial x_j} [\rho u_i'' u_j'' - \overline{\rho u_i'' u_j''}] \end{aligned} \quad (2.62)$$

$$\frac{\partial(\rho e_o')}{\partial t} + \frac{\partial}{\partial x_j} [\tilde{h}_o(\rho u_j)' + \tilde{u}_j(\rho h_o)' - \tilde{h}_o \tilde{u}_j \rho'] = -\frac{\partial}{\partial x_j} [\rho h_o'' u_j'' - \overline{\rho h_o'' u_j''}] \quad (2.63)$$

where all quantities have been decomposed according to either $\phi = \bar{\phi} + \phi'$ or $\phi = \tilde{\phi} + \phi''$, where $\tilde{\phi} = \overline{\rho \phi} / \bar{\rho}$ is the Favre average of ϕ . All non-linearities have been moved to the right hand side and can be viewed as source terms for small perturbations.

The main problem with this system of equations is two-fold. First, the linear Euler operator supports not only acoustic waves, but vorticity and entropy waves as well. Second, there is no mechanism for the dissipation of energy. This means that, for some flow cases, the vorticity and entropy modes may grow without bounds. Part of the problem is the lack of a viscous term, part of the problem is the linearization of the system. In a non-linear system a disturbance may become saturated, which prevents further growth.

2.3.2 Hardin and Pope's Equations

The approach of Hardin and Pope [28] is unique in the sense that it assumes from the outset that the flow field will be obtained by an incompressible simulation, which has rendered it the name Expansion about Incompressible Flow (EIF). The equations are fully non-linear, and the only assumption made is to neglect viscosity.

While being a novel approach, and certainly an interesting one, it is the opinion of this author that it is more physically illuminating to derive equations for the acoustics, and then to decide whether compressibility effects are important or not in determining the source terms. This will, to some degree, be done in section 2.4.1.

Some question marks regarding Hardin and Pope's derivation have been raised by Shen and Sørensen [29], who argued the existence of an inconsistency in the formulation.

2.4 Sound Generation

When splitting the problem into sound generation and sound propagation, the source terms in the propagation equation will represent the generation. Whether solving a scalar equation or a system of equations, these source terms need to be computed, typically by the use of more traditional Computational Fluid Dynamics (CFD) methods.

2.4.1 Importance of Compressibility

Traditional CFD methods for low Mach number flows are typically incompressible, but is it possible to compute source terms to a clearly compressible phenomenon (acoustics) from an incompressible field?

In a compressible field, the value of a source term at a certain time will be an effect of hydrodynamic phenomena, like turbulence, and acoustic phenomena, like already existing sound waves. This particular source term will then (maybe) generate sound. The corresponding incompressible field would include the turbulence, but not the sound waves. Hence, the same source term, when computed from the corresponding incompressible field, would then (maybe) generate sound, *but only the sound due to hydrodynamic phenomena.*

An example of this could be the wall pressure terms in Curle's and Ffowcs Williams and Hawkings' equations. Since the pressure on solid walls is primarily affected by hydrodynamic phenomena, it is possible to compute these source terms from an incompressible field. The only effect lost would be that of any incoming sound waves, which means that these incoming waves would not give rise to reflected waves leaving the solid wall.

This example only applies to the scalar equations, since the systems of equations include reflections when solving for the acoustic fluctuations. It is

possible to remedy this problem for the scalar equations by using a so-called *hard wall Green's function* to derive a scalar propagation equation, tailored to a specific geometry. In essence, this technique takes all possible reflections at walls into account in the Green's function (giving it the name *hard wall*), which means that even an incompressible simulation together with this tailored scalar propagation equation will include reflections at walls. Wang and Moin [30] adapted this technique to compute the generation and scattering of sound at the trailing edge of a wing, a case where the presence of the wing has a large influence on the generation and the directivity of the radiated sound.

Lighthill's tensor $T_{ij} = \rho u_i u_j - \tau_{ij} + (p - a_\infty^2 \rho) \delta_{ij}$ is normally⁶ simplified for low Mach number flows. The viscous term is dropped, since most flows are at high Reynolds numbers, making viscous effects negligible. Since $p = p(\rho, s)$, where s is the entropy, small fluctuations in pressure can be written as

$$p' = \left. \frac{\partial p}{\partial \rho} \right|_s \rho' + \left. \frac{\partial p}{\partial s} \right|_\rho s' = a^2 \rho' + \left. \frac{\partial p}{\partial s} \right|_\rho s' \quad (2.64)$$

The pressure p and density ρ in the term $(p - a_\infty^2 \rho) \delta_{ij}$ can be replaced by the fluctuations p' and ρ' , since the mean (time-averaged) components will only contribute to the constant of integration. This, together with equation (2.64), then yields

$$p - a_\infty^2 \rho = p' - a_\infty^2 \rho' = (a^2 - a_\infty^2) \rho' + \left. \frac{\partial p}{\partial s} \right|_\rho s' \quad (2.65)$$

and it is seen that that the $(p - a_\infty^2 \rho) \delta_{ij}$ -term represents the effects of entropy fluctuations, and of deviations of the speed of sound from its ambient value. In most low Mach number flows, $s' \approx 0$ and $a \approx a_\infty$, which then means that the $(p - a_\infty^2 \rho) \delta_{ij}$ -term will be negligible.

The density is very close to its ambient value in low Mach number flows, which yields the common simplification $T_{ij} \approx \rho_\infty u_i u_j$.

When computing Lighthill's tensor T_{ij} from an incompressible field, some care has to be taken. The double divergence of the full Lighthill tensor $\partial^2 T_{ij} / \partial x_i \partial x_j = \partial^2 (\rho u_i u_j - \tau_{ij} + (p - a_\infty^2 \rho) \delta_{ij}) / \partial x_i \partial x_j$ will, when computed

⁶The arguments for simplification were originally put forth by Lighthill, and have been used by most researchers since.

from an incompressible field, be identically zero! Upon inspection this is not surprising, since Lighthill's equation reduces to the incompressible Poisson equation for pressure, when the density is assumed constant. In this case, the convective term is perfectly balanced by the pressure term, as it should be in an incompressible field.

The correct approach, instead, is to make the simplification $T_{ij} \approx \rho_\infty u_i u_j$ while considering the fluid compressible, and then to realize that the convective term will be essentially the same, whether compressibility is taken into account or not.

Another interesting observation is that the simplified source term in Lighthill's equation, when computed from an incompressible velocity field, becomes

$$\frac{\partial^2 \rho_\infty u_i u_j}{\partial x_i \partial x_j} = \rho_\infty \frac{\partial u_i}{\partial x_j} \frac{\partial u_j}{\partial x_i} \quad (2.66)$$

which is exactly (except for the constant ρ_∞) the same as the source term in Phillips' equation.

2.4.2 Resolution Requirements

Most studies on aero acoustics find that the majority of the acoustic energy exists in the low frequency modes. These modes can typically be computed by Large Eddy Simulation (LES) or Unsteady RANS (URANS).

In some cases, the higher frequency modes are important for the sound generation. Seror *et al* [31] considered this problem in the case of LES, and analyzed the contribution from the subgrid stress. They found that, for some flow cases, the sound from the high frequency modes (included in the subgrid model) needs to be included to get reliable results.

If a large part of the spectrum needs to be included in the source terms, it is evident that this complicates matters at higher Reynolds numbers. A fundamentally different approach suitable to these situations is the stochastic source modeling, sometimes called the Stochastic Noise Generation and Radiation (SNGR) method. In this method, a stationary RANS is used to compute the kinetic energy of the turbulence in the whole field. The energy spectrum of the turbulence is then assumed to be isotropic, and divided into a discrete number of wavenumber bands. Using the assumed spectrum and

the turbulent kinetic energy, the energy of each mode is computed. The phases and directions of all modes are then randomized in time and space, which generates a fluctuating velocity field that is not turbulence, but that at least has the same spectrum as turbulence. This fluctuating field is then used to compute the source terms of some acoustic equation. For further reading on SNGR, the thesis by Billson [12] and the article by Bechara [25] are recommended.

2.5 Sound Pressure Level

The acoustic intensity I_i , i.e. the acoustic flux of energy through a unit area in direction i , is defined as [32]

$$I_i = p' u'_i \quad (2.67)$$

Since the human ear registers differences in sound levels on a logarithmic scale, it is common to define the Sound Pressure Level (*SPL*) as

$$SPL_i = 10 \log_{10} \left(\frac{\bar{I}_i}{10^{-12} W/m^2} \right) dB \quad (2.68)$$

where the unit is the famous *dB*, or decibel. For plane waves, the velocity and the pressure fluctuations are related as [33]

$$u'_i = \frac{n_i p'}{\rho a_\infty} \quad (2.69)$$

where n_i is a unit vector in the direction of the wave. In the i -direction, this yields

$$SPL = 10 \log_{10} \left(\frac{\overline{(p')^2}}{\rho a_\infty 10^{-12} W/m^2} \right) = 20 \log_{10} \left(\frac{p_{rms}}{p_{ref}} \right) \quad (2.70)$$

with $p_{ref} = \sqrt{\rho_\infty a_\infty 10^{-12} W/m^2}$. For atmospheric conditions, $p_{ref} = 2.0 \cdot 10^{-5} Pa$. Typically, the term *SPL* is used when referring to the acoustic intensity within a certain frequency band, and the term Overall Sound Pressure Level (*OASPL*) is used when referring to the total acoustic intensity.

Chapter 3

Choice of Method and Test Case

There are many areas in vehicle design that involve aero acoustics, and they have differing characteristics that make it hard to choose one methodology to deal with them all. For example, external wind noise and climate system noise are both coupled one-way, whereas the ‘booming’ noise experienced when driving with an open sunroof or side window, is coupled two-ways. From the review in chapter 2, it is then quite obvious that some kind of Direct Simulation would be needed to solve the ‘booming’ noise problem.

The geometry of the problem is also important to consider, since the scalar equations do not take reflections into account. In the case of external wind noise, the geometries are often simple enough that scalar equations can be used, but in the case of climate system noise, the reflections in the ducts are probably crucial, and hence a systems of equations, that solve for all reflections, may be necessary.

3.1 Acoustic Method

In accordance with the stated objectives of this work, some criteria on the chosen method can be stated:

1. Simple method, which in this case is interpreted as a scalar method with an analytical solution.
2. Both wall and volume sources have to be taken into account, and the noise sources have to appear explicitly for the purpose of analysis.

These criteria suggest the use of Curle's or Ffowcs Williams and Hawkings' equations. Since, except for when studying fan noise, the noise sources are stationary relative to the observer, Curle's equation is chosen in this work.

3.2 Test Case

In order to test the method, a test case that fulfills some criteria is needed:

1. Wall bounded flow, to maximize the relevance to vehicle applications.
2. Low Mach number, since flows in vehicle applications are typically at low Mach numbers.
3. Simple enough geometry so that a scalar method is applicable.
4. Laminar flow, to simplify the problem and enable a focus on the acoustics.
5. Case well tested and analyzed in the literature.

The test case found to best fulfill these criteria is the *open cavity*, that has been investigated theoretically, numerically, and experimentally, by many researchers.

3.2.1 Review on Open Cavities

The open cavity has been a popular test case for investigations in areas like fluid dynamic oscillations, fluid dynamic resonance, aero acoustics, and flow control, for decades. The reason to this is probably the simple geometry, and the fascinating flow features this seemingly simple case gives rise to. While

making no attempt at reviewing all the work that has been done on the open cavity, included here is some work that is relevant to this thesis.

Gharib and Roshko [34] studied the incompressible flow in and around axisymmetric cavities experimentally, and found that the flow in a cavity is heavily dependent on the length to depth (L/D) ratio. At low L/D , a shear layer is formed along the upper part of the cavity. The flow above the cavity is relatively undisturbed, and the main unsteady flow feature is the convection of vortices in the shear layer. The drag of the cavity is fairly low, typically $C_D \sim 0.01$. At higher L/D , the flow becomes more violent and unsteady. A vortex that fills the whole cavity is formed at the leading edge of the cavity, and when it is large enough it is released at the trailing edge. The flow above the cavity is affected by the flow inside the cavity, and freestream fluid is periodically directed into the cavity. The drag in this flow regime is much higher, typically $C_D \sim 0.3$. Gharib and Roshko used the term *wake-mode* to describe this latter flow regime, and some researchers use the term *shear-mode* to describe the first one. In this thesis, the terms *shear regime* and *wake regime* will be used, in order to avoid confusion with the term *mode*, which is used for dominant frequencies.

The review of Rockwell and Naudascher [35] offers an excellent overview of the various types of cavity flows, and of what parameters are important in determining the character of the flow. Included in this review are the measurements and findings by Ethembabaoglu [36], Sarohia [37], and Rossiter [38]. Ethembabaoglu performed incompressible experiments with turbulent boundary layers, and found that the spectrums of the wall pressure fluctuations were highly organized with clear peaks. This suggests that a feedback mechanism is present, which couples the flow and the acoustics in a two-way manner¹, and that the turbulence itself may be of secondary importance to the oscillations. In experiments with laminar boundary layers, Sarohia found that the cavity depth is insignificant, unless it is of the same order of magnitude as the boundary layer thickness $\delta_{0.99}$. Rossiter stressed the importance of the boundary layer upstream of the cavity, and found that a thinner boundary layer generates larger levels of fluctuations in the cavity.

Ahuja and Mendoza [39] performed aero acoustic measurements in cavities with the purpose of using the results for validation of CAA codes. Among other things, they studied the importance of $\delta_{0.99}$, L/D ratio, the influence

¹The feedback mechanism will be explained at the end of this section. two-way coupling is explained in chapter 2.

of the spanwise width of the cavity, and the Mach number, on the radiated sound in several directions.

During especially the last couple of years, several numerical studies of open cavity flows have been published. Colonius *et al* [11] performed Direct Simulations of the flow in 2D cavities at fairly low Reynolds numbers, typically $Re_D = 1500$. Varying several parameters, including L/D , M , and $\delta_{0.99}$, they found that the primary parameter deciding which flow regime (shear or wake regime) that will be present, is L/θ , where θ is the momentum thickness of the boundary layer.

Gloerfelt *et al* [16] performed similar 2D Direct Simulations, but at higher Mach and Reynolds numbers ($L/D = 2$, $M = 0.7$, and $Re_D = 41000$). At these Reynolds numbers one can start to question the 2D approach, since it prevents the existence of real turbulence. Nevertheless, if feedback mechanisms are more important than the nature of the turbulence, as Ethem-babaoglu's experiments suggest, 2D simulations may offer valuable insights even at fairly high Reynolds numbers.

Shieh and Morris [14] performed Large Scale Simulations (LSS) of cavities with $L/D = 2$ and $L/D = 4.4$ at Mach numbers 0.4, 0.5, and 0.6. Their presented Reynolds number is 200000, but is unclear from their paper what dimension this is based on. They found that the mean streamlines in the shear regime are virtually undisturbed above the cavity, but clearly not so in the wake regime. Also, they found the mean pressure profiles along the bottom of the cavity to be distinctly different between the shear and wake regimes.

Ashcroft and Zhang [40] repeated Ahuja and Mendoza's measurements using Unsteady RANS (URANS), and captured the main flow features. This is yet another indication that it is the feedback mechanisms of the low-frequency modes that are controlling the cavity flow.

Many attempts at feedback models that predict the dominant frequencies have been made, with Rossiter's [38] being the first one. These models typically try to model the convection of a vortex in the shear layer, the impingement of this vortex on the downstream cavity wall, the propagation upstream of an acoustic wave, and the triggering of a new vortex near the leading edge. These models are typically fairly successful in predicting shear regime flows, but rather unsuccessful in predicting wake regime flows. This comes as no surprise, since the feedback mechanism modeled only applies to

the shear regime. The current focus of feedback modeling seems to be to find the criterion for the regime-switching. Rossiter's model is

$$St_L = \frac{fL}{U_\infty} = \frac{m - \phi}{M + \frac{1}{\kappa}} \quad (3.1)$$

where f is the frequency, m is the mode number (integer), ϕ is the phase-lag between vortex impingement and emission of sound at the downstream wall, and κ is the ratio of the eddy convection velocity to the freestream velocity.

3.2.2 Summary of Open Cavity Findings

To summarize the findings of these authors, the current state of knowledge about the oscillations in open cavities is:

1. There exists two fundamentally different flow regimes; the shear and the wake regimes. The drag of a cavity is typically about $C_D \sim 0.01$ in the shear regime, and about $C_D \sim 0.3$ in the wake regime.
2. The feedback mechanisms that amplify certain frequencies are very important in deciding the structure of the open cavity flow. Evidence suggest that these mechanisms are of greater importance than the structure, or even existence, of turbulence in the cavity.
3. The boundary layer thickness $\delta_{0.99}$ upstream of the cavity is a very important parameter. A thinner boundary layer will generate higher amplitude fluctuations. Very thick boundary layers, on the other hand, may totally remove the dominant modes.
4. The depth D of a cavity is not an important parameter, unless it is of the same order of magnitude as $\delta_{0.99}$. The length L of a cavity is more important, and hence a parameter like the Strouhal number should be based on L .

The effect of the *details* of the incoming boundary layer, such as whether it is turbulent or not, seems rather unclear at the moment. On the one hand, findings such as number 2 above suggest that the presence of turbulence is of secondary importance, but on the other hand findings such as number 3 suggest that the details of the boundary layer are vital. A turbulent boundary

layer is more resistant to separation, and it transports momentum across the shear layer more efficiently, so the presence and the structure of turbulence in the boundary layer is probably a fairly important parameter as well.

3.2.3 Choice of Test Case

From the list of criteria in section 3.2, it is clear that no case studied in previous investigations offers a perfect match, primarily because of the too high Mach numbers studied. The best match is the study by Colonius *et al* [41], being laminar and at a low Reynolds number. The test case studied in this thesis will be an open cavity with:

1. $L/D = 4$ to ensure wake regime oscillations, since the violent, transient behaviour is typical of flows in vehicle applications.
2. $M = 0.15$, which at atmospheric conditions means a velocity of about 180 km/h. At vehicle speeds of about 140 km/h, the flow velocity around the sides of the car is typically about 180 km/h.
3. $Re_D = 1500$, which corresponds to the value used by Colonius *et al*.
4. The momentum thickness at the leading edge, assuming laminar flat-plate growth, will be $\theta/D = 0.04$, which corresponds to Colonius *et al*'s study.

Since no experimental data is available, a Direct Simulation resolving both the flow and the acoustics, will be performed. The database generated will serve as a benchmark for the computations with Curle's equation, and will also be used to compute the acoustic source terms.

Chapter 4

Methodology, Direct Simulation

The code used for the Direct Simulation is based on the finite volume code written by Eriksson [42]. Several modifications were made, including increasing the spatial and temporal accuracy, making the code work in 2D, and making the code parallel by the use of Message Passing Interface (MPI).

The governing equations, i.e. the continuity (2.1), momentum (2.2), and energy (2.3) equations, can be written on a compact conservative form as

$$\frac{\partial Q}{\partial t} + \frac{\partial E_j}{\partial x_j} = \frac{\partial F_j}{\partial x_j} \quad (4.1)$$

with

$$Q = \begin{pmatrix} \rho \\ \rho u_i \\ \rho e_o \end{pmatrix} \quad E_j = \begin{pmatrix} \rho u_j \\ \rho u_i u_j + p \delta_{ij} \\ \rho e_o u_j + p u_j \end{pmatrix} \quad F_j = \begin{pmatrix} 0 \\ \tau_{ij} \\ \tau_{ij} u_i - q_j \end{pmatrix} \quad (4.2)$$

where Q is the state vector, E_j is the convective or inviscid fluxes, and F_j is the diffusive or viscous fluxes.

4.1 Finite Volume Formulation

Integrating equation (4.1) over an arbitrary control volume Ω yields

$$\int_{\Omega} \frac{\partial Q}{\partial t} dV + \int_{\Omega} \left[\frac{\partial E_j}{\partial x_j} - \frac{\partial F_j}{\partial x_j} \right] dV = 0 \quad (4.3)$$

Since the temporal differentiation commutes with the integration, it can be taken outside the integral of the first term. The remaining two terms are rewritten by the use of Gauss' theorem to

$$\frac{\partial}{\partial t} \int_{\Omega} Q dV + \int_{\partial\Omega} [E_j n_j - F_j n_j] dA = 0 \quad (4.4)$$

where n_j is a unit normal pointing outwards, and $\partial\Omega$ is the bounding surface of Ω . Interpreting Ω as a cell in a finite volume framework, the integrals are now approximated (2nd order accurate) to

$$V_c \frac{\partial \overline{Q}^v}{\partial t} + \sum_{faces} A_f n_j [\overline{E}_j^f - \overline{F}_j^f] = 0 \quad (4.5)$$

where V_c is the volume of the cell, A_f is the area of a cell face, \overline{Q}^v is the volume average of Q , and \overline{E}_j^f is the face average of E_j .

The volume averages of the state vector (\overline{Q}^v) are chosen as the degrees of freedom (DOF), which means that the face averaged fluxes (\overline{E}_j^f and \overline{F}_j^f) need to be written in terms of the DOF, i.e. $\overline{E}_j^f(\overline{Q}^v)$ and $\overline{F}_j^f(\overline{Q}^v)$.

4.2 Inviscid Flux

Acoustic wave propagation is an almost inviscid phenomena, and hence the convective flux approximation is critical in order to correctly resolve acoustics. Many researchers have studied and proposed convective schemes for CAA, for example Tam and Webb [6], Bogey and Bailly [7], and Lele [43]. While their proposed schemes differ slightly, they all argue that schemes for CAA should be at least 4th order accurate¹ or higher. In this study, a scheme

¹The accuracy of these schemes is 4th order in a 1D linear system, but only 2nd order in a non-linear system. It is customary to refer to the accuracy in a linear system when discussing numerical schemes.



Figure 4.1: Finite volume grid 1

with a 6-point stencil will be used, which enables the use of schemes with up to 6th order accuracy.

A discretized system of equations can give rise to unphysical, high wave number, oscillations. This is especially true at the boundaries, where the use of extrapolated information and high order schemes creates grid-to-grid oscillations. To remove these unphysical waves, a small amount of artificial dissipation is added by upwinding. The question then is: How apply the upwinding, since the equations permit acoustic waves traveling both upstream and downstream (at subsonic speeds)?

When linearized, and projected onto a direction, the compressible Euler (inviscid Navier-Stokes) equations can be decoupled into 5 different characteristic variables, traveling at 5 different speeds [2]. When decoupled, the direction of propagation of different characteristic variables is easily determined, and hence upwinding can be applied in a straightforward manner. The fact that the equations must be linearized is not an obstacle, since only small changes occur during a timestep (and hence a linearization is permissible). Since fluxes describe transport through a face, the face normal is a natural choice of direction to project the equations onto.

The decoupling of the Euler equations into characteristic variables is described in detail in Larsson [2], and only a brief description of the convective flux algorithm will be given here. Consider a part of a finite volume grid as in figure 4.1. The inviscid flux through the face between cells 3 and 4 is computed by:

1. Compute the primitive² variables \bar{q}_o^f at the face using linear interpolation from \bar{q}_3^v and \bar{q}_4^v . The primitive variables are $q = (\rho, u_i, p)^T$.

²It is considerably easier to work with the primitive variables than the conservative ones.

2. Linearize the Euler equations around \bar{q}_o^f , project the equations onto the face normal n_j , and decouple into 5 characteristic variables \bar{W}_m^f and eigenvalues λ_m .
3. Compute \bar{W}_m^v in the neighbouring cells.
4. Based on the sign of λ_m , compute \bar{W}_m^f as

$$\bar{W}_m^f = \sum_{l=1}^6 c_l \bar{W}_{m,l}^v \quad , \quad \lambda_m > 0 \quad (4.6)$$

or

$$\bar{W}_m^f = \sum_{l=1}^6 c_{7-l} \bar{W}_{m,l}^v \quad , \quad \lambda_m < 0 \quad (4.7)$$

where c_l are the coefficients of the convective scheme.

5. Transform back to primitive variables \bar{q}^f .
6. Compute \bar{E}_j^f from \bar{q}^f .

The separate steps in the algorithm are all 2nd order accurate, except for steps 2 and 4. The accuracy of step 4 is dependent on the scheme used, which in CAA typically means high order. The accuracy of step 2 is hard to quantify; it only influences the direction used in the upwinding.

Having noticed all 2nd order approximations being made (primarily associated with the volume- or face-averaging), one might wonder what the point of a higher order interpolation scheme in step 4 is. Would not the 2nd order errors mask any improved accuracy in step 4? Numerical experiments [4] show that the errors from the volume- or face-averaging are small, albeit of 2nd order. The dominant source of error is the interpolation to the face, which justifies the use of a higher order method in this particular step.

The Dispersion Relation Preserving (DRP) scheme of Tam and Webb [6] is used in this study. This scheme is 4th order accurate, and it is optimized to minimize the dispersion errors. For numerical stability, a 6th order artificial dissipation term is added. An analysis of the DRP-scheme and the artificial dissipation, plus definitions and guidelines for choosing the dissipation parameter ϵ , are included in Larsson [1]. In this study, $\epsilon = 0.003$ is used.

4.3 Viscous Flux

The diffusive fluxes are, in the majority of the domain, much smaller than the convective ones. Furthermore, diffusion is not important for acoustic wave propagation, and hence the diffusive flux approximation is less critical than the convective flux approximation in CAA. In this study, a 2nd order accurate 2-point stencil is used to discretize the viscous terms. Considering figure 4.2, the flux \bar{F}_j^f at the face between cells 3 and 4 has to be approximated in terms

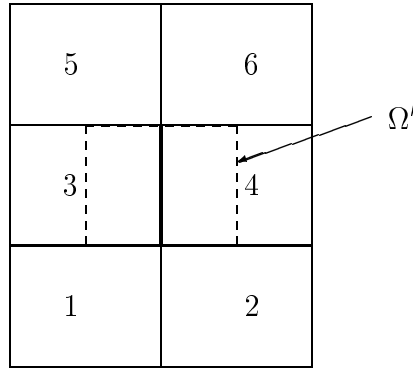


Figure 4.2: Finite volume grid 2

of the DOF in the neighbouring cells. The viscous flux involves gradients of velocity and temperature, so $\partial \bar{q}^f / \partial x_j$ needs to be computed at the face. This is done by introducing an auxiliary control volume Ω' , which is marked by the dashed line in figure 4.2. The viscous flux is then computed by:

1. Approximate the face-averaged gradient with the volume-averaged one.

$$\frac{\partial \bar{q}^f}{\partial x_j} \approx \frac{\partial \bar{q}^v}{\partial x_j} \quad (4.8)$$

2. Gauss' theorem yields

$$\frac{\partial \bar{q}^v}{\partial x_j} = \frac{1}{V_{\Omega'}} \int_{\Omega'} \frac{\partial q}{\partial x_j} dV = \frac{1}{V_{\Omega'}} \int_{\partial \Omega'} q n_j dA \quad (4.9)$$

which is approximated as

$$\frac{\partial \bar{q}^v}{\partial x_j} \approx \frac{1}{V_{\Omega'}} \sum_{\Omega' \text{ faces}} \bar{q}^{\Omega' f} n_j A_{\Omega' f} \quad (4.10)$$

3. Compute $\bar{q}^{\Omega f}$ by linear interpolation from \bar{q}^v .

All steps are 2nd order accurate.

4.4 Time Integration

It is well known that the compressible Navier-Stokes equations become stiff at low Mach numbers, since the speed of propagation of acoustic information is a factor $1/M$ faster than that of convected information. A common way of solving this problem is to use preconditioning, which modifies the temporal derivatives $\partial Q/\partial t$ in a way that essentially brings down the speed of sound. For problems where temporal accuracy is important, an implicit discretization in time can be used, and the preconditioning is then applied when solving the system of equations at each timestep. This approach is typically called dual time stepping, and it has been used by for example Weiss and Smith [44]. A preconditioner developed by Eriksson [45] was analyzed in Larsson [2], but it was found that the performance degraded severely when applied in a dual time stepping framework. Speed-up factors of 1 to 2 (when compared to the un-preconditioned system) were observed, which is similar to what Weiss and Smith reported. With such speed-ups, an explicit method will be more efficient, even at low Mach numbers.

Rewriting equation (4.5) as

$$\frac{\partial \bar{Q}^v}{\partial t} = -\frac{1}{V_c} \sum_{faces} A_f n_j [\bar{E}_j^f(\bar{Q}^v) - \bar{F}_j^f(\bar{Q}^v)] \quad (4.11)$$

and keeping in mind that $\bar{E}_j^f(\bar{Q}^v)$ and $\bar{F}_j^f(\bar{Q}^v)$ are approximations computed by the spatial schemes, equation (4.11) can now be used to compute an approximation to the temporal derivative of the DOF, for any given field \bar{Q}^v . A 4-stage, 4th order accurate, explicit Runge-Kutta algorithm is used to march the solution in time, as

$$\begin{aligned} \bar{Q}_{(1)}^v &= \bar{Q}_n^v + \frac{1}{4}\Delta t \frac{\partial \bar{Q}_n^v}{\partial t} \\ \bar{Q}_{(2)}^v &= \bar{Q}_n^v + \frac{1}{3}\Delta t \frac{\partial \bar{Q}_{(1)}^v}{\partial t} \end{aligned}$$

$$\begin{aligned}\overline{Q}_{(3)}^v &= \overline{Q}_n^v + \frac{1}{2}\Delta t \frac{\partial \overline{Q}_{(2)}^v}{\partial t} \\ \overline{Q}_{n+1}^v &= \overline{Q}_n^v + \Delta t \frac{\partial \overline{Q}_{(3)}^v}{\partial t}\end{aligned}\tag{4.12}$$

Larsson [1] includes an analysis of the accuracy and the stability of the Runge-Kutta algorithm. In short, it was found that $CFL < 0.75$ gives good accuracy.

4.5 Boundary Conditions

The boundary conditions (BCs) of a Direct Simulation are critical, since reflections at the boundaries can totally contaminate a solution. The main problem is that the acoustic energy typically is about 1% of the total energy of the flow, or less. This means that even if only a small portion of the energy in a vortex leaving the domain is reflected as an acoustic wave, this may act as a more powerful source of sound than the flow itself. Non-reflective BCs for CAA have been studied and proposed by, among many others, Tam *et al* [46], Hu [47], and Rowley and Colonius [48]. Although Billson [12] found that the BCs specifically developed for CAA are superior relative to the more traditional BCs used in compressible flow, a fairly traditional one is used in this study. The reason to this is partly the simplicity, but also the fact that the highly accurate BCs tailored to CAA are less robust [41] for the large amplitude, non-linear fluctuations (vortices) that are present in this study.

The BCs are applied to the convective and diffusive terms separately, and the inviscid terms make use of the same characteristic variable approach that is used for the spatial fluxes.

4.5.1 Inviscid BC

At boundaries, the inviscid flux scheme presented in section 4.2 is used, with the only modification being that the state vector outside the boundary is set to some prescribed boundary state \overline{Q}_{bc}^v . The net effect of this is that information propagating into the domain is taken from the prescribed boundary state \overline{Q}_{bc}^v , while information propagating out from the domain is extrapolated

at the boundary. In subsonic flows, 4 characteristics (1 entropy wave, 2 vorticity waves, and 1 acoustic wave) will follow the direction of the convection, and 1 characteristic (1 acoustic wave) will have the opposite direction.

At inflow, outflow, or freestream boundaries, the prescribed state \overline{Q}_{bc}^v is set to the appropriate values (such as ρ_∞ etc). At solid walls, \overline{Q}_{bc}^v is computed by mirroring the flow with respect to the wall.

4.5.2 Viscous BC

The viscous flux at inflow, outflow, and freestream boundaries is neglected. At solid walls, the boundary conditions are $u_i \equiv 0$ (no-slip) and $\partial T / \partial n \equiv 0$ (adiabatic). The gradients at the boundary face are approximated by a 1st order accurate stencil, but apart from that, the same methodology as in section 4.3 is used.

4.5.3 Buffer Layers

The boundary conditions used in this study are non-reflective only for small amplitude waves normal to the boundary. To minimize the reflections from the boundaries, buffer layers, where disturbances are damped slowly before reaching the boundary, are added to the domain. In the buffer layers, an extra damping term is added to the equations as

$$\frac{\partial Q}{\partial t} + \frac{\partial E_j}{\partial x_j} = \frac{\partial F_j}{\partial x_j} - \sigma_o \xi^2 (Q - Q^*) \quad (4.13)$$

where σ_o is a buffer parameter, ξ is the non-dimensional distance from the beginning of the buffer layer ($0 \leq \xi \leq 1$), and Q^* is the target state. In a buffer layer, it is important that the value of σ_o is properly chosen. Too large values will generate reflections at the beginning of the buffer layer, while too small values will not dampen the oscillations fast enough. An analysis of buffer layers and how to compute σ_o is included in Larsson [1]. The values of σ_o used in this study are given in table 4.1, where L_b is the length of the buffer layer, M_c is the Mach number of the oscillation, and D_b is the damping ratio as defined in [1]. $M_c = M$ at the outflow boundary, since the primary oscillations are convected vortices.

Boundary	L_b	M_c	σ_o	D_b
Inflow	2.2	$1 - M$	11.7	1%
Outflow	10	M	2.07	1%
Freestream	6.2	1	11.2	2.4%

Table 4.1: Buffer parameters

Chapter 5

Methodology, Curle's Equation

Curle wrote the solution to Lighthill's equation on a form with the spatial derivatives outside the integral, since this simplifies estimations of the radiated sound. For numerical computations, it is better to have the derivatives inside the integral. This, together with Sarkar and Hussaini's [24] arguments that temporal derivatives of the source term are preferable over spatial derivatives, suggests that equation (2.42) should be modified along those lines. In this work, the radiated sound fairly close to the region of generation is to be studied, and hence Sarkar and Hussaini's assumption that r is much larger than the extent of the sources, is invalid. This assumption, however, is not necessary, and will not be used here.

If the observer in equation (2.42) is located in a region where the flow is isentropic, the density fluctuation at this location can be written $\rho(\mathbf{x}, t) - \rho_o = (p(\mathbf{x}, t) - p_o)/a_\infty^2$. For a function $f(\tau)$, where $\tau = t - r/a_\infty$ is the retarded time, the spatial derivative can be converted to a temporal one by

$$\frac{\partial}{\partial x_i} \left[\frac{f(\tau)}{r} \right] = -\frac{\partial r}{\partial x_i} \left[\frac{\dot{f}}{a_\infty r} + \frac{f}{r^2} \right] = -l_i \left[\frac{\dot{f}}{a_\infty r} + \frac{f}{r^2} \right] \quad (5.1)$$

where l_i is a unit vector pointing from the source location to the observer location. Using this, equation (2.42) can be written as

$$\begin{aligned} p(\mathbf{x}, t) - p_o &= \\ &= \frac{1}{4\pi} \frac{\partial}{\partial x_i} \int_V -l_j \left[\frac{\dot{T}_{ij}}{a_\infty r} + \frac{T_{ij}}{r^2} \right] dV(\mathbf{y}) \end{aligned}$$

$$\begin{aligned}
 & -\frac{1}{4\pi} \int_S -l_i n_j \left[\frac{\dot{p}\delta_{ij} - \dot{\tau}_{ij}}{a_\infty r} + \frac{p\delta_{ij} - \tau_{ij}}{r^2} \right] dS(\mathbf{y}) \\
 = & \frac{1}{4\pi} \int_V \left(l_i l_j \left[\frac{\ddot{T}_{ij}}{a_\infty^2 r} + 2\frac{\dot{T}_{ij}}{a_\infty r^2} + 2\frac{T_{ij}}{r^3} \right] - \frac{\partial l_j}{\partial x_i} \left[\frac{\dot{T}_{ij}}{a_\infty r} + \frac{T_{ij}}{r^2} \right] \right) dV(\mathbf{y}) \\
 & + \frac{1}{4\pi} \int_S l_i n_j \left[\frac{\dot{p}\delta_{ij} - \dot{\tau}_{ij}}{a_\infty r} + \frac{p\delta_{ij} - \tau_{ij}}{r^2} \right] dS(\mathbf{y}) \tag{5.2}
 \end{aligned}$$

The term $\partial l_j / \partial x_i$ is expanded to

$$\frac{\partial l_j}{\partial x_i} = \frac{\partial}{\partial x_i} \left[\frac{x_j - y_j}{r} \right] = \frac{\delta_{ij} - l_i l_j}{r} \tag{5.3}$$

Inserting this into equation (5.2) yields

$$\begin{aligned}
 p(\mathbf{x}, t) - p_o = & \\
 = & \frac{1}{4\pi} \int_V \left[\frac{l_i l_j}{a_\infty^2 r} \ddot{T}_{ij} + \frac{3l_i l_j - \delta_{ij}}{a_\infty r^2} \dot{T}_{ij} + \frac{3l_i l_j - \delta_{ij}}{r^3} T_{ij} \right] dV(\mathbf{y}) \\
 & + \frac{1}{4\pi} \int_S l_i n_j \left[\frac{\dot{p}\delta_{ij} - \dot{\tau}_{ij}}{a_\infty r} + \frac{p\delta_{ij} - \tau_{ij}}{r^2} \right] dS(\mathbf{y}) \tag{5.4}
 \end{aligned}$$

and it is seen that Sarkar and Hussaini's form of the volume integral (2.59) is retrieved when r becomes large. Equation (5.4) is one principal result of this thesis.

For simplicity in the numerical algorithm, and for purposes of distinguishing between the different contributions, the pressure signal at the observer is split into

$$p(\mathbf{x}, t) - p_o = p_v(\mathbf{x}, t) - p_{o,v} + p_s(\mathbf{x}, t) - p_{o,s} \tag{5.5}$$

where p_v and p_s are the contributions from the volume and surface sources, respectively.

5.1 Volume Sources

The contribution from the volume sources can be written as

$$p_v(\mathbf{x}, t) - p_{o,v} = \sum_{cells} \frac{1}{4\pi} \int_{cell} \left[\frac{l_i l_j}{a_\infty^2 r} \ddot{T}_{ij} + \frac{3l_i l_j - \delta_{ij}}{a_\infty r^2} \dot{T}_{ij} + \frac{3l_i l_j - \delta_{ij}}{r^3} T_{ij} \right] dV(\mathbf{y}) \tag{5.6}$$

If the source terms and r change only slightly over a cell, this can be approximated to

$$p_v(\mathbf{x}, t) - p_{o,v} = \sum_{cells} \frac{V_c}{4\pi} \left[\frac{l_i l_j}{a_\infty^2 r_c} \ddot{T}_{ij}^v + \frac{3l_i l_j - \delta_{ij}}{a_\infty r_c^2} \dot{T}_{ij}^v + \frac{3l_i l_j - \delta_{ij}}{r_c^3} \overline{T}_{ij}^v \right] \quad (5.7)$$

where V_c is the cell volume and $r_c = |\mathbf{x} - \mathbf{y}_c|$, where \mathbf{y}_c is the cell center coordinates. The source terms in equation (5.7), being volume-averages, can be computed from \overline{Q}^v with 2nd order accuracy, and the temporal derivatives are computed using 2nd order accurate central stencils.

5.2 Surface Sources

The contribution from the surface sources can be written as

$$p_s(\mathbf{x}, t) - p_{o,s} = \sum_{faces} \frac{1}{4\pi} \int_{face} l_i n_j \left[\frac{\dot{p} \delta_{ij} - \dot{\tau}_{ij}}{a_\infty r} + \frac{p \delta_{ij} - \tau_{ij}}{r^2} \right] dS(\mathbf{y}) \quad (5.8)$$

If the source terms and r change only slightly over a face, this can be approximated to

$$p_s(\mathbf{x}, t) - p_{o,s} = \sum_{faces} \frac{l_i n_j A_f}{4\pi} \left[\frac{\dot{\overline{p}}^f \delta_{ij} - \dot{\overline{\tau}}_{ij}^f}{a_\infty r_c} + \frac{\overline{p}^f \delta_{ij} - \overline{\tau}_{ij}^f}{r_c^2} \right] \quad (5.9)$$

where A_f is the face area and r_c is the distance from the observer to the center of the face, as for the volume sources. The source terms can be computed from \overline{Q}^v with 2nd order accuracy, and the temporal derivative is computed using a 2nd order accurate stencil.

5.3 Time Accumulation

The pressure signal at the observer is described by equations (5.5), (5.7), and (5.9). In these equations, the source terms are to be computed at the retarded time $\tau = t - r/a_\infty$, where t is the time at the observer position.

In a discretized system, the observer time is $t_n = n\Delta t$, and the source time is $\tau_l = l\Delta\tau$, where n and l are integers. Using a simplified form, the pressure

signal can be written as

$$p(\mathbf{x}, t_n) = \sum_i f^{(i)}\left(t_n - \frac{r}{a_\infty}\right) \quad (5.10)$$

where i are all elements (cells and faces) that radiate sound, and $f^{(i)}$ is the source term for that particular element. For one element, the contribution Δp is

$$\Delta p(\mathbf{x}, t_n) = f^{(i)}\left(t_n - \frac{r}{a_\infty}\right) \quad (5.11)$$

Since the system has been discretized, the source term $f^{(i)}$ will only be available at times τ_l . With $\tau_l < t_n - r/a_\infty \leq \tau_{l+1}$, interpolation in time *at the source* yields

$$\Delta p(\mathbf{x}, t_n) = \left[1 - \frac{\left(t_n - \frac{r}{a_\infty}\right) - \tau_l}{\Delta\tau}\right] f^{(i)}(\tau_l) + \left[\frac{\left(t_n - \frac{r}{a_\infty}\right) - \tau_l}{\Delta\tau}\right] f^{(i)}(\tau_{l+1}) \quad (5.12)$$

It is convenient to choose $\Delta t = \Delta\tau$, although it is possible not to. With this choice, one gets the simpler equation

$$\Delta p_n = \left[1 - \left(n - \frac{r}{a_\infty\Delta t} - l\right)\right] f_l^{(i)} + \left[n - \frac{r}{a_\infty\Delta t} - l\right] f_{l+1}^{(i)} \quad (5.13)$$

where $\Delta p_n = \Delta p(\mathbf{x}, t_n)$ and $f_l^{(i)} = f^{(i)}(\tau_l)$

In order to relate n to l , one notes that $l < n - r/(a_\infty\Delta t) \leq l + 1$ or similarly $l + r/(a_\infty\Delta t) < n \leq l + 1 + r/(a_\infty\Delta t)$. Hence, when using $R^-()$ as a function that rounds towards minus infinity,¹

$$n = R^-\left(l + 1 + \frac{r}{a_\infty\Delta t}\right) = l + 1 + R^-(\Theta) \quad (5.14)$$

where $\Theta = r/(a_\infty\Delta t)$. Equation (5.13) can now be written as

$$\Delta p_n = [\Theta - R^-(\Theta)] f_l^{(i)} + [1 - (\Theta - R^-(\Theta))] f_{l+1}^{(i)} \quad (5.15)$$

It is now straightforward to see that the element i at source time l will contribute to the signal at the observer location as

$$\begin{aligned} \Delta\Delta p_n &= [\Theta - R^-(\Theta)] f_l^{(i)} \\ \Delta\Delta p_{n-1} &= [1 - (\Theta - R^-(\Theta))] f_l^{(i)} \end{aligned} \quad (5.16)$$

¹ $R^-()$ rounds a real number a to the closest integer *smaller* than a . For example, $R^-(3.99) = R^-(3.01) = R^-(3) = 3$ and $R^-(2 + 4.99) = 2 + R^-(4.99) = 6$.

where n is given by equation (5.14).

The $\Delta\Delta$ symbol indicates that the contributions have to be summed in both space and time. The main reason for deriving equation (5.16) is that the retarded time integrals can be computed without storing massive amounts of data at different times. Instead, the contributions can be summed while stepping in time.

5.4 Extension to 3D

Lighthill's equation, and hence Curle's solution, is valid in three dimensions, which means that the integrals have to be taken over a 3D volume and a 2D surface, respectively. For 2D cases, it is possible to derive a 2D analogue of equation (5.4), something that has been done by for example Gloerfelt *et al* [16]. The present work, however, will later move on to 3D geometries, and hence the 3D formulation of equation (5.4) is kept. Instead, 2D geometries will be viewed as infinite in the third direction, and the integrals will have to be extended in this direction.

Extending the integrals is, in principle, straightforward, but the important question as to whether they are convergent has to be addressed.² First, it is assumed that the observer is at $x_3 = 0$. Looking at one element (cell or face), the distance between the source and the observer can be written as $r = \sqrt{R^2 + y_3^2}$, where $R = \sqrt{(x_1 - y_1)^2 + (x_2 - y_2)^2}$ is the distance in two dimensions. From this, and the definition of l_i , one gets

$$\frac{1}{r} \sim l_1 \sim l_2 \sim \frac{1}{y_3} \quad , \quad l_3 \sim 1 \quad , \quad \text{as } y_3 \rightarrow \infty \quad (5.17)$$

Now, a close inspection of equations (5.7) and (5.9) reveals that all terms, except for the viscous and entropy $((p - a_\infty^2 \rho) \delta_{ij})$ terms, go to zero as $1/y_3^2$ or faster, making those integrals convergent. The viscous and entropy terms go to zero as $1/y_3$, which for ordinary functions would make those integrals divergent. In this case, however, the fact that the source terms are to be evaluated at a retarded time (that is a function of y_3), *might* make the

²The reader is reminded that integrals like $\int_\epsilon^\infty x^n dx$ are divergent for $n \geq -1$, and convergent for $n < -1$.

integrals convergent. Numerical experiments show that the integrals, indeed, are convergent.

5.5 Numerical Experiments

The computations of the discretized integrals (5.7) and (5.9) are dependent on some parameters, and the dependence of the final result on these parameters have to be established. The number of samples N_s (during a period) used to compute Curle's integral will affect the result, as will the cell size Δy_3 and the total distance $N\Delta y_3$ used to extend the integral to 3D. Also, the extent in the second direction $y_{2,ext}$ where volume sources are computed, needs to be determined.

The test case in these tests is the open cavity, and the radiated sound as computed by Curle's discretized equation is used for comparisons. For each parameter, a sequence of computations is performed, where each computation uses twice (or half) the value of the parameter, compared to the previous computation. The error is defined as the L_2 norm of the difference between two computations, and is, hence, a measure of how much the radiated sound changes when changing the value of the parameter.

Denoting the result from a sequence of computations by p_i ($i = 1, 2, 3, \dots$), where $p_i = p(\mathbf{x}, t)$ with $\mathbf{x}/D = (1, 7.16)$, the error can be defined as

$$\epsilon_i = \frac{\|p_i - p_{i-1}\|_2}{\|p_1\|_2} \quad (5.18)$$

The parameters tested are presented in table 5.1, and the parameter changed in each sequence of runs is printed in **boldface**.

Since Curle's integral is linear, the error is computed for each term individually. In a chapter 7, the contributions from the viscous terms, entropy terms, and $(\rho - \rho_\infty)u_i u_j$ terms will be found to be negligible, and hence the simplification $T_{ij} \approx \rho_\infty u_i u_j$ is used in these tests. In that same chapter, the source terms will be numbered for simplicity, and the same numbering is used here. Terms 1 and 2 are the $\dot{p}/(a_\infty r)$ and p/r^2 terms in equation (5.9), respectively. Terms 5, 9, and 10 are the $\ddot{T}_{ij}/(a_\infty^2 r)$, $\dot{T}_{ij}/(a_\infty r^2)$, and T_{ij}/r^3 terms in equation (5.7), respectively.

Case	$\Delta y_3/D$	$N\Delta y_3/D$	N_s	$y_{2,ext}/D$
1.1	0.2	320	160	6
1.2	0.4	320	160	6
1.3	0.8	320	160	6
1.4	1.6	320	160	6
1.5	3.2	320	160	6
2.1	0.6	480	160	6
2.2	0.6	240	160	6
2.3	0.6	120	160	6
2.4	0.6	60	160	6
3.1	0.6	180	240	6
3.2	0.6	180	120	6
3.3	0.6	180	60	6
4.1	0.6	180	160	6
4.2	0.6	180	160	5
4.3	0.6	180	160	4
4.4	0.6	180	160	3
4.5	0.6	180	160	2

Table 5.1: Numerical experiments. Parameter in **boldface** is changed.

Term	$\epsilon_{\Delta y_3} \sim$	$\epsilon_{N\Delta y_3}$	ϵ_{N_s}
1	$290(\Delta y_3/D)^{-2.2}$	$(N\Delta y_3/D)^n$	$290(N_s)^{-2.2}$
2	$86(\Delta y_3/D)^{-2.3}$	$(N\Delta y_3/D)^n$	$86(N_s)^{-2.3}$
5	$0.23(\Delta y_3/D)^{-0.3}$	$(N\Delta y_3/D)^n$	$0.23(N_s)^{-0.3}$
9	$3.0(\Delta y_3/D)^{-1.4}$	$(N\Delta y_3/D)^n$	$3.0(N_s)^{-1.4}$
10	$3.1(\Delta y_3/D)^{-1.9}$	$(N\Delta y_3/D)^n$	$3.1(N_s)^{-1.9}$

Table 5.2: Results from numerical experiments

For each contribution, and for each parameter tested, functions on the form $\epsilon = C\phi^n$, where ϕ is the parameter tested, are fitted to the results. The errors are summarized in table 5.2. The most striking result is that term 5 seems to be more sensitive to the number of samples per period than the other terms. The reason to this is not known.

The error introduced when changing $y_{2,ext}$ is fairly small. Since the integrals involve $1/r^n$ terms, it is not desirable to integrate the volume sources too closely to the observers. Therefore, $y_{2,ext}/D = 6$ is chosen as a compromise between converging the integral, and avoiding problems with the $1/r^n$ terms.

As for the other parameters, $\Delta y_3/D = 0.6$, $N\Delta y_3/D = 180$, and $N_s = 133$, are chosen. These values give errors of the order of 1%, which will later be found to be smaller than the errors introduced when using Curle's equation to compute the radiated sound.

Chapter 6

Open Cavity, Direct Simulation

In chapter 3 the *open cavity* was chosen as a test case in this study, and a brief review of previous research on open cavity flows was presented. Also, the lack of existing experimental data for this particular case indicated the need for a Direct Simulation. This Direct Simulation will be used to compute the source terms in Curle's equation, and for comparisons of the radiated sound. The methodology of the DS is described in chapter 4.

The computational domain is shown in figure 6.1. The resolution is roughly 80 cells per unit length (D) in and around the cavity, and the grid is stretched less than 1% per cell in the whole resolved domain. An upper limit on the cell size (roughly 3 times the smallest cell size) is set to avoid acoustic waves being reflected in the grid; if a high wavenumber wave reaches a region where the cell size is too large for it to be resolved, it will be reflected *in the grid* and contaminate the solution. The resolved domain extends between $-4.3 \leq x_1/D \leq 19$, and for $x_2/D \leq 10.5$. Outside of this domain, buffer layers are added to ensure non-reflective boundary conditions. The total number of cells is 593 900, of which 122 700 are located in the buffer layers.

This chapter mainly includes analyses of the flow field, and analyses to ensure the quality of the DS. The radiated sound will be analyzed further in chapter 7.

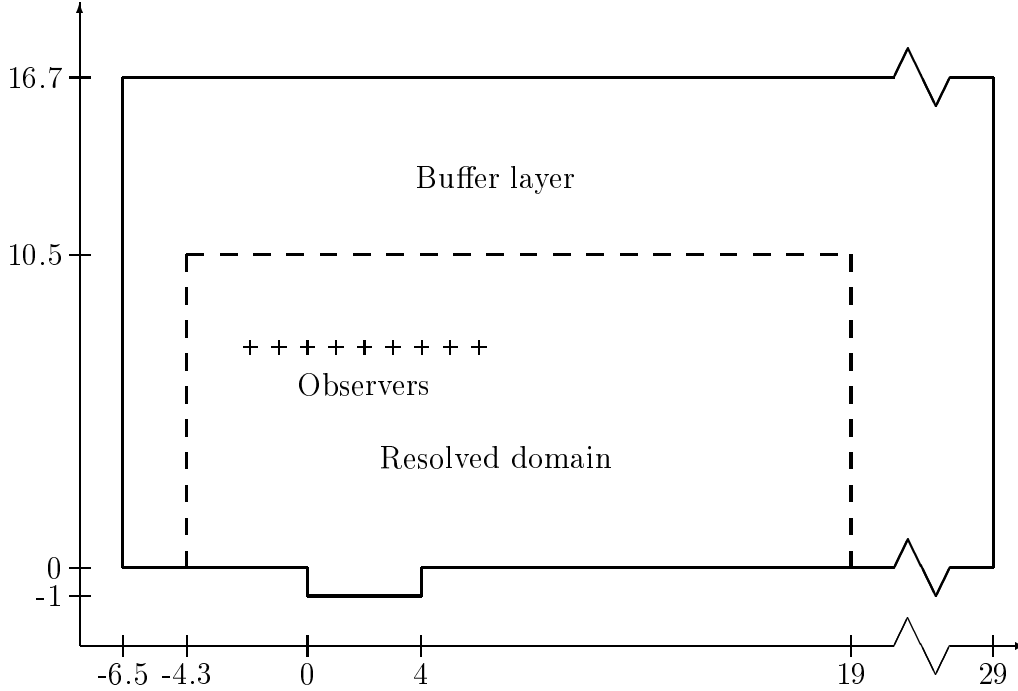


Figure 6.1: Computational domain, coordinates normalized by D

6.1 Cavity Drag

The drag of the cavity per unit width (being a 2D geometry) is defined as

$$C_D = \frac{F_1}{\frac{1}{2}\rho_\infty U_\infty^2 D} \quad (6.1)$$

where F_1 is the force in the 1-direction. After the initial transients have disappeared, a statistically stationary state is reached, as can be seen in figure 6.2(a). The mean drag is $\overline{C}_D = 0.384$, and it is interesting to note that the drag associated with pressure alone (no viscous stress) is $\overline{C}_D^p = 0.409$, i.e. larger than the total drag. This is due to the fact that the flow along the bottom of the cavity is mainly towards the left, and hence the viscous contribution is actually to lower the drag. The values computed in this study are in qualitative agreement with other published results. Gharib and Roshko [34] report $\overline{C}_D \sim 0.3$ for the incompressible flow in axisymmetric cavities. Colonius *et al* [41] report $\overline{C}_D = 0.227$ for a similar case but at $M = 0.6$.

The spectrum of the cavity drag is plotted in figure 6.2(b), where the ampli-

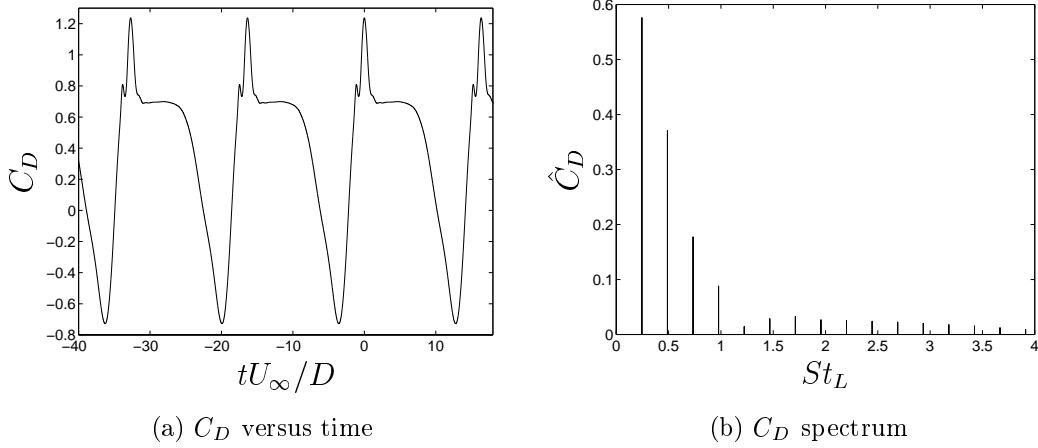


Figure 6.2: Cavity drag

tude \hat{C}_D of the drag is plotted versus the Strouhal number defined by

$$St_L = \frac{fL}{U_\infty} \quad (6.2)$$

The fundamental frequency is $St_L = 0.245$, and all higher modes are harmonics of this fundamental frequency. The first 4 modes are the largest, which means that most of the energy exists at $St_L \leq 1$.

A comparison with other published results is quite interesting. Colonius *et al* [41] report a fundamental frequency $St_L = 0.248$, which is almost identical to the value computed here. Other results worth mentioning are the ones by Ethembabaoglu [36] ($L/D = 4$, incompressible, $Re_\delta \approx 250000$, $\delta^*/D = 0.042$, $St_L \approx 0.5$), Shieh and Morris [14] ($L/D = 4.4$, $M = 0.6$, $Re = 200000$, $\delta_{0.99}/D = 0.2$, $St_L = 0.216$), Ashcroft and Zhang [40] ($L/D = 3.75$, $M = 0.26$, $Re_L \approx 280000$, $St_L \approx 0.5$), and Ahuja and Mendoza [39] (similar to Ashcroft and Zhang).

Is there a trend in these results? The similarity between this study and the one by Colonius *et al* suggests that Mach number effects (at least on the frequency) are small in the wake regime. The differences with respect to the other studies are harder to explain. If Mach number effects are indeed small, the most probable explanation would be effects by the Reynolds number or the boundary layer properties. For turbulent boundary layers, the displacement thickness $\delta^* \approx \delta_{0.99}/8$ [21], which means that Shieh and Morris' simulation had a displacement thickness $\delta^*/D \approx 0.025$. This value is

similar to Ethembaraoglu's, and it is hard to see any trends in the reported frequencies.

6.2 Incoming Boundary Layer

Most studies on open cavity flows show the importance of the incoming boundary layer (BL), but few study it in more detail. An attempt at doing this is included here. Since the incoming BL in this study is laminar, the famous Blasius solution (see for example [21]) is available for flat plate flows. Comparisons between the time-averaged BL in the simulation and the analytical solutions for a flat plate may yield some insight into open cavity flows.

A few definitions [21] are needed to analyze the BL. The boundary layer thickness $\delta_{0.99}$ is defined as the height where the velocity has reached 99% of its freestream value. The displacement thickness δ^* , which is the distance streamlines outside the BL are displaced, is defined as

$$\delta^* \equiv \int_0^{\infty} \left(1 - \frac{u}{U_{\infty}}\right) dx_2 \quad (6.3)$$

The momentum thickness θ , which is a measure of the viscous drag of the plate up to the point of the BL profile, is defined as

$$\theta \equiv \int_0^{\infty} \frac{u}{U_{\infty}} \left(1 - \frac{u}{U_{\infty}}\right) dx_2 \quad (6.4)$$

The shape factor H is defined as $H \equiv \delta^*/\theta$.

The momentum thickness θ at the beginning of the resolved domain ($x_1/D = -4.3$) is used to compute the virtual origin of the BL, and this virtual origin is then used to determine the analytical solutions [21]

$$\frac{\delta_{0.99,a}}{x_1} = \frac{5}{\sqrt{Re_{x_1}}} \quad , \quad \frac{\delta_a^*}{x_1} = \frac{1.721}{\sqrt{Re_{x_1}}} \quad , \quad \frac{\theta_a}{x_1} = \frac{0.664}{\sqrt{Re_{x_1}}} \quad (6.5)$$

The shape factor $H = 2.59$ for a flat plate, and separation occurs at $H_{sep} \approx 3.5$.

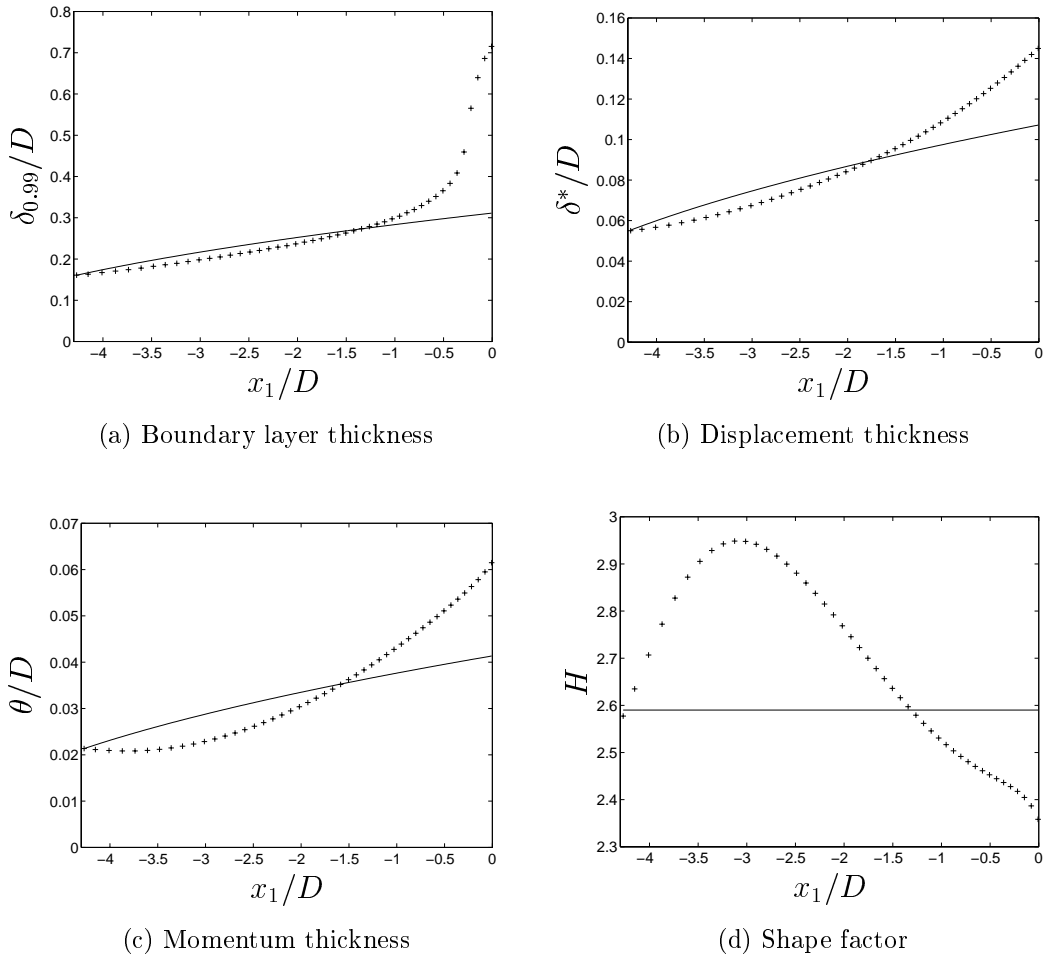


Figure 6.3: Incoming boundary layer. '-' analytical, '+' DS

The computed BL parameters are plotted in figure 6.3 together with the analytical solutions for a flat plate. It is seen that the time-averaged BL behaves in a very different way compared to a flat plate BL. The growth rate *increases* downstream, instead of *decreasing* like the flat plate solution. The plot of the momentum thickness is especially disturbing; since $\theta(x_1)$ is a measure of the drag from the virtual origin to x_1 , figure 6.3(c) suggests that the plate drag up to $x_1/D \approx -3.8$ is negative, which it of course can not be. The problem here is that all these theories are based on a uniform freestream velocity U_∞ , but the freestream velocity is actually increasing slowly with x_1 in this case. The reason is the periodic build-up and shedding of a vortex, which forces the freestream to accelerate around it.

Parameter	Actual value	Projected value
$\delta_{0.99}/D$	0.647	0.309
δ^*/D	0.142	0.107
θ/D	0.0595	0.0411
H	2.39	2.60

Table 6.1: Incoming boundary layer parameters at the cavity leading edge

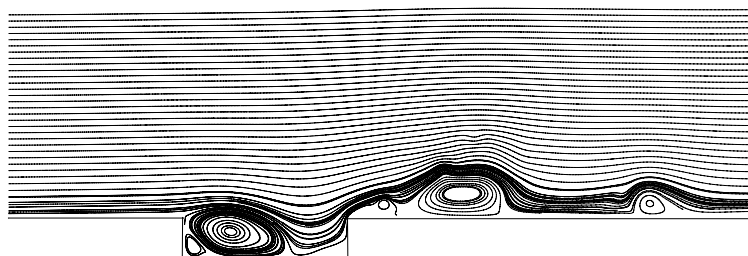
The fact that the incoming BL behaves as it does complicates comparisons with other published investigations. Colonius *et al* [41], for example, present the projected value of θ at the leading edge, assuming laminar growth. Other researchers, especially the experimentalists, present time-averaged values of $\delta_{0.99}$, δ^* , or θ at the leading edge. From the figures, it is clear that these measures can not be compared directly. The choice of Colonius *et al* is specifically cumbersome, since the projected values depend on how far upstream they are computed from. In this study, the projected and the actual parameters of the incoming BL are given in table 6.1.

6.3 Flow Features

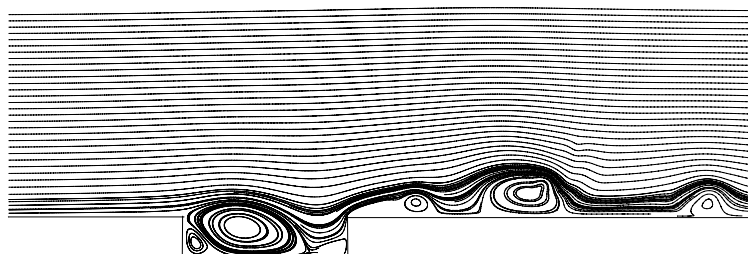
The flow in open cavities is truly fascinating, with many complicated flow patterns despite the geometric simplicity. A sequence of snapshots with instantaneous streamlines are shown in figures 6.4 and 6.5.

The time has been defined to be $t \equiv 0$ at the peak in C_D (see figure 6.2(a)), and the period is $T_p U_\infty / D = 16.32$.

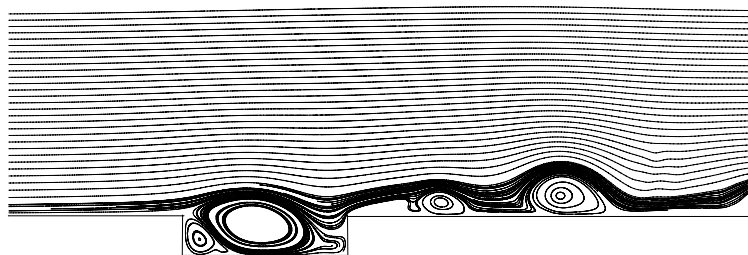
Starting at $tU_\infty / D = 12.24$, a vortex is formed at the leading edge. This vortex grows, and at $tU_\infty / D = 16.32$ a secondary vortex appears at the lower corner of the upstream cavity wall. At $tU_\infty / D = 2.04$, the primary vortex is large enough to deflect the flow above the cavity, and the boundary layer upstream of the cavity separates (albeit hard to see in the figures). At $tU_\infty / D = 8.16$, the secondary vortex (rotating counter-clockwise) has grown large enough to re-attach the upstream BL. At this time, the primary vortex has started to move downstream. At $tU_\infty / D = 10.20$, the primary vortex impinges on the downstream cavity wall, and during the next 2 snapshots it is ejected at the trailing edge. Freestream fluid is pulled down into the cavity at $tU_\infty / D = 14.28$, and it impinges on the downstream cavity wall



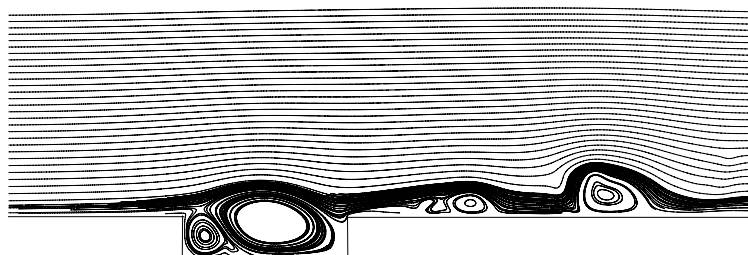
(a) $tU_\infty/D = 2.04$



(b) $tU_\infty/D = 4.08$

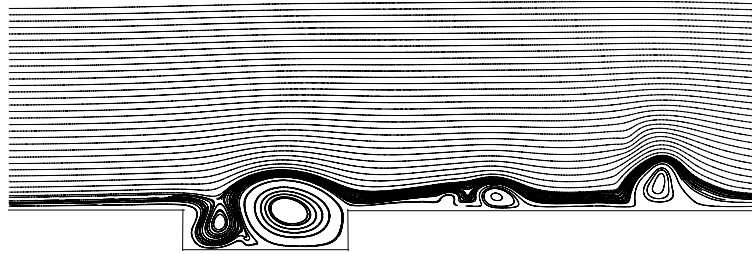


(c) $tU_\infty/D = 6.12$

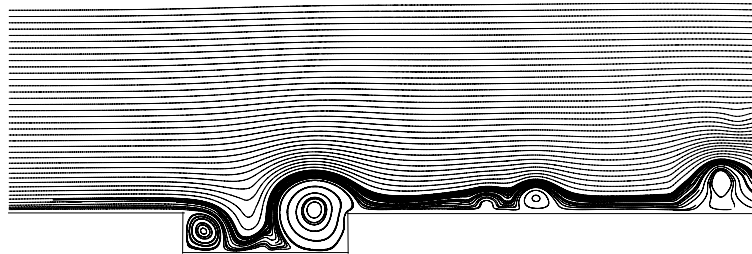


(d) $tU_\infty/D = 8.16$

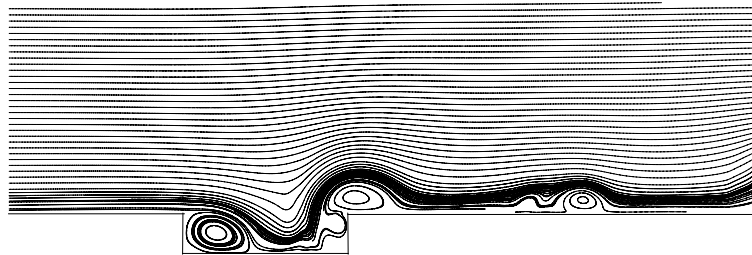
Figure 6.4: Instantaneous streamlines 1



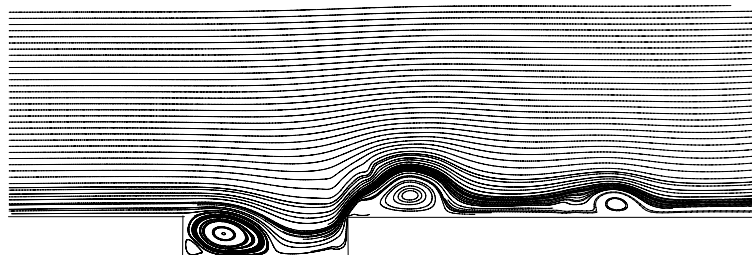
(a) $tU_\infty/D = 10.20$



(b) $tU_\infty/D = 12.24$



(c) $tU_\infty/D = 14.28$



(d) $tU_\infty/D = 16.32$

Figure 6.5: Instantaneous streamlines 2

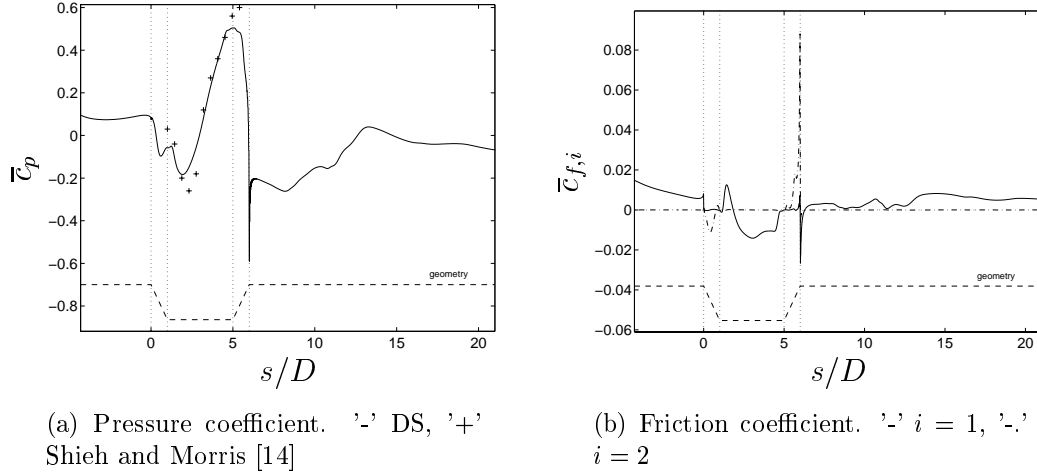


Figure 6.6: Mean pressure and friction coefficients

at $tU_\infty/D = 16.32$, which is when the maximum drag occurs. The ejected vortices are convected along the wall downstream of the cavity until they leave the resolved domain.

The pressure coefficient c_p , and the wall friction coefficient c_f , are defined as

$$c_p = \frac{p - p_\infty}{\frac{1}{2}\rho_\infty U_\infty^2} \quad (6.6)$$

and

$$c_{f,i} = \frac{n_j \tau_{ij}}{\frac{1}{2}\rho_\infty U_\infty^2} \quad (6.7)$$

where $c_{f,i}$ is the friction coefficient in the i -direction. The time-averaged values \bar{c}_p and $\bar{c}_{f,i}$ are plotted in figure 6.6. The parameter s in the figures is the distance from the leading edge *along the wall*, and the vertical lines outline the corners of the cavity. The fact that the viscous contribution to the cavity drag is negative is now seen clearly, since $\bar{c}_{f,1}$ is mainly negative along the bottom wall. This, of course, is a result of the flow along the bottom being primarily to the left, as was seen in figures 6.4 and 6.5.

The mean pressure \bar{c}_p is low on the upstream cavity wall and in the beginning of the cavity. It rises steeply towards the end of the cavity, and reaches a maximum in the lower, downstream wall, corner. This maximum is due to the periodic impingement of the freestream, which creates a stagnated region. The pressure decreases sharply at the trailing edge, due to the high

acceleration around the edge. Behind the cavity, the pressure rises slowly and reaches a small peak at $x_1/D \approx 11$ (i.e. $s/D \approx 13$), from where it falls of.

\bar{c}_p along the bottom wall from Shieh and Morris [14] is included in figure 6.6(a). Despite being a different case ($L/D = 4.4$, $M = 0.6$, $Re = 200000$, $\delta_{0.99}/D = 0.2$), the mean pressure coefficients are remarkably similar. Note that their results were for a longer cavity, and hence their bottom wall extends to $s/D = 5.4$. The trends are very similar; a minimum at $x_1/D \approx 1$ followed by a steep increase as the downstream cavity wall is approached. Shieh and Morris got a larger maximum value of \bar{c}_p at the downstream cavity wall, which could be a result of their longer cavity, giving the flow a larger distance for pressure recovery. This hypothesis is strengthened by the fact that the profiles follow the same trend between $x_1/D \approx 2$ and $x_1/D \approx 3.5$. Another possibility is that the higher Mach number of Shieh and Morris' case gives higher 'oscillations', an idea that is emboldened by the fact that all peaks are stronger in their results. A last possibility is the fact that their results were computed using a turbulence model, which could have given erroneous results.

The small peak of \bar{c}_p at $x_1/D \approx 11$ is probably an effect of a small secondary vortex. This smaller vortex is only seen in figures 6.4 and 6.5 as a small disturbance of the primary vortex as it travels downstream from the cavity. At $x_1/D \approx 11$, the smaller vortex is located in the lower part of the primary vortex, and this may enhance the entrainment of fluid towards the wall. This would then increase the pressure on the wall at that location.

6.4 Radiated Sound

The pressure signals in the 9 observation locations, shown in figure 6.1 and listed in table 6.2, are recorded during one period. From these, the Overall Sound Pressure Levels (*OASPL*, see section 2.5) are computed, and plotted in figure 6.7. The intensity of the radiated sound has a minimum straight above the downstream cavity wall, and it increases both upstream and downstream. Most published data on the directivity of the radiated sound from open cavities is for the far field, which makes comparisons with the present results hard. As will be seen in chapter 7, the observer locations used here are clearly in the near field. This being said, a qualitative comparison may

Observer	x_1/D	x_2/D
1	-2	7.16
2	-1	7.16
3	0	7.16
4	1	7.16
5	2	7.16
6	3	7.16
7	4	7.16
8	5	7.16
9	6	7.16

Table 6.2: Observer locations

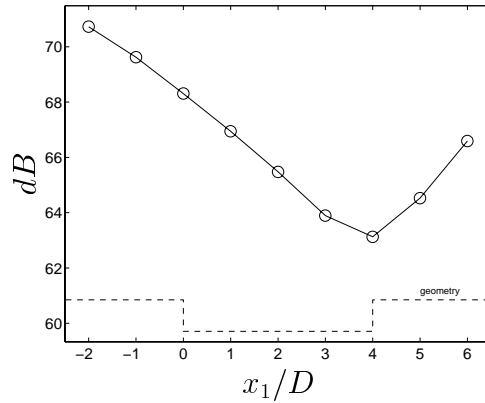


Figure 6.7: Radiated sound, OASPL

still be carried out.

Shieh and Morris [14] report maximum radiation in a direction 135° from the positive x_1 -axis, which agrees with figure 6.7 in the sense that the radiation is strongest in the upstream direction. Ahuja and Mendoza [39] present the *OASPL* for various angles at locations about $200D$ away from the cavity. Their results show a minimum roughly straight above the cavity, and increases of about 3 dB in the upstream direction. The increases in the downstream direction are slightly smaller. The present results are in qualitative, but not quantitative, agreement with Ahuja and Mendoza's findings. In chapter 7, the discrepancy will be found to be a near field effect.

The pressure signals, non-dimensionalized by

$$c'_p = \frac{p'}{\frac{1}{2}\rho_\infty U_\infty^2} \quad (6.8)$$

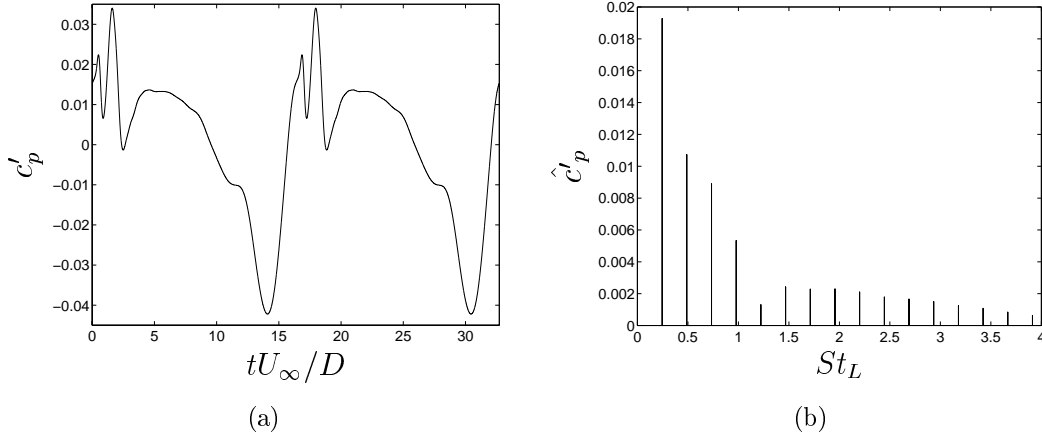


Figure 6.8: Observer 1

and their spectrums, where \hat{c}'_p is the amplitude, are plotted for some observers. Figure 6.8 shows observer 1, the location where the sound intensity has its maximum. The signal has a peak at $tU_\infty/D = 1.605$. The signals at positions 2 and 3 (not shown) have peaks at $tU_\infty/D = 1.548$ and $tU_\infty/D = 1.520$, respectively, which indicates that the high pressure pulse has propagated upstream. Recalling that the flow stagnates at the downstream cavity wall at $t \approx 0$ (figure 6.5), the peaks in the radiated pressure signals occur at $\Delta tU_\infty/D \approx (r/a_\infty)(U_\infty/D) = Mr/D$ after the pressure at the downstream wall has its peak value. This is an indication that the downstream cavity wall is important in the sound generation process, a fact that will be seen more clearly in chapter 7.

The spectrum at observer 1 is similar to the spectrum of the cavity drag in figure 6.2(b), with the fundamental frequency being the dominant mode. In contrast to the spectrum of \hat{C}_D , though, some energy exists up to $St_L \approx 4$.

The pressure signal at observer 5 is shown in figure 6.9, and the peak is now at $tU_\infty/D = 0.1980$. The major difference, compared to observer 1, is that the dominance of the fundamental frequency has decreased, due to the increase of mode 3. While the reason for this is not known, it is clear that there exists less of a coupling between the sound and the cavity drag, compared to at the locations farther upstream.

Observer 9, the one farthest downstream, is plotted in figure 6.10. Most of the energy is in the first 2 modes, and the high-pressure pulse is much less

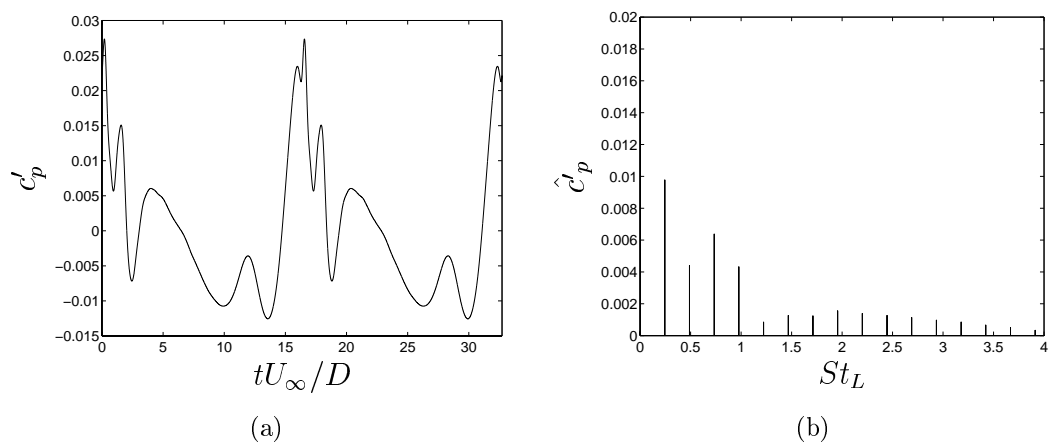


Figure 6.9: Observer 5

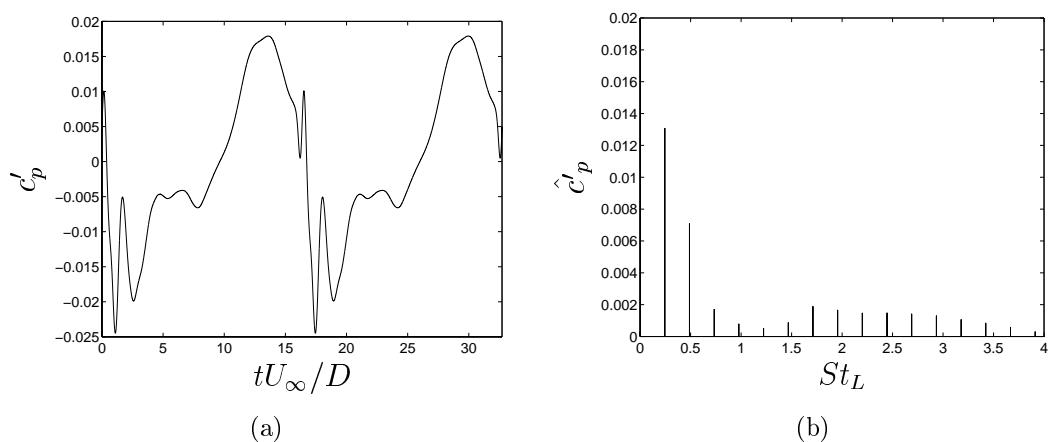


Figure 6.10: Observer 9

pronounced. In fact, the signal is fundamentally different compared to the other observer locations, in that there is a slow increase in pressure, followed by a sharp decrease (opposite to the observers upstream). This indicates that the radiated sound at downstream locations is generated in a different way compared to the upstream locations.

6.5 Grid Independence

Grid independence studies are important in all areas of CFD, and especially so in Direct Simulations of sound. The resolution has to be fine enough to resolve all important physics, and the boundary conditions must not affect the solution significantly. The latter is critical in CAA, since sound waves propagate over large distances. Although a boundary may be far away from the region of interest, any reflected sound waves will contaminate the solution in the *whole* domain.

6.5.1 Resolution

The shortest wavelength of interest is $\lambda_{min}/D = (L/D)/(MSt_L) \approx 7$, since most of the energy is contained in $St_L \leq 4$. At this wavelength, the resolution is roughly 500 cells per wavelength, which indicates that the resolution is, indeed, fine. Nevertheless, a simulation using roughly twice the cell size is run, and the main results are $C_D = 0.395$ and $St_L = 0.246$. The frequency has changed 0.4%, and the drag has changed 2.9%. The change in frequency is minimal, and the change in drag is probably due to too large values of y^+ . The mean values of y^+ for the standard grid are below 1, with a maximum of $y_{max}^+ = 3$ at the downstream cavity wall at $tU_\infty/D \approx 12.24$. These values are considered good enough, but with twice the cell size, errors in the computation of the viscous stress are to be expected.

6.5.2 Boundary Conditions

A simulation using a similar grid in and around the cavity, but with the boundaries moved closer, is run to test the influence of the boundary locations. The downstream boundary is moved $5D$ to $x_1/D = 14$, and the freestream boundary is moved $1.7D$ to $x_2/D = 8.8$. The length of the buffer layers are kept constant. The upstream boundary is kept, since it, and the buffer layer, determines the incoming boundary layer thickness.

The main parameters St_L , \overline{C}_D , and \overline{C}_D^p are completely unaffected, which is encouraging but expected. The real test is the sound at the observer locations, since the boundary conditions may reflect or generate sound that

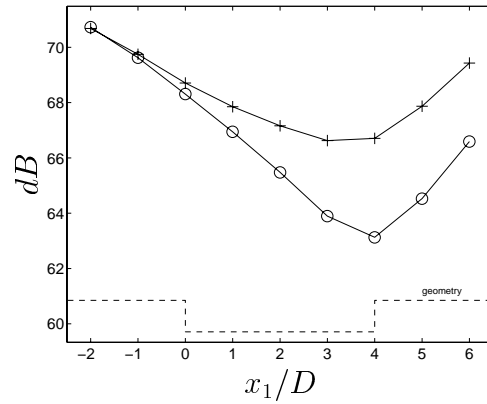


Figure 6.11: Grid independence, OASPL. 'o' standard grid, '+' shortened grid

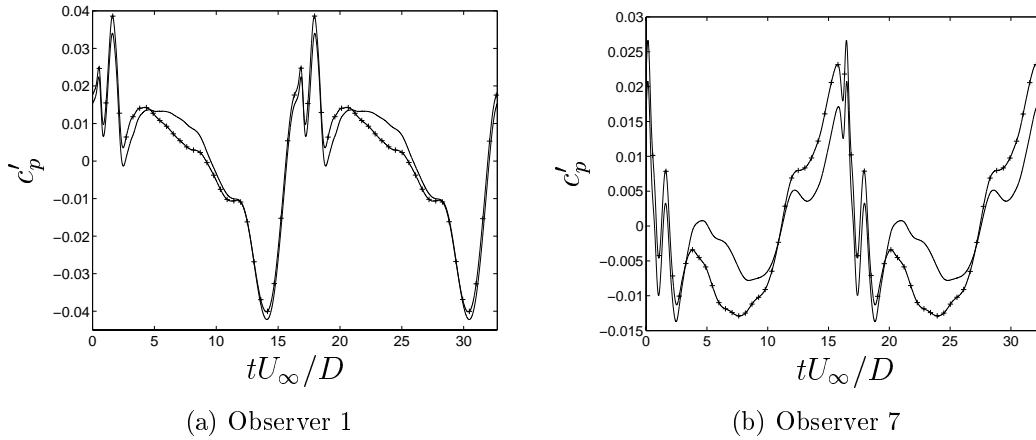


Figure 6.12: Grid independence, p' versus time. '-' standard grid, '-+' shortened grid

would contaminate the sound at those (or any other) positions. The Overall Sound Pressure Level (OASPL) is computed for both the standard grid and the shortened one, and plotted in figure 6.11. The 2 grids give similar OASPL at the upstream locations, but the shorter grid gives larger values at all other locations, especially the ones downstream. The largest difference is 3.6 dB. To further analyze the differences, the pressure signals at locations 1 ($x_1/D = -2$) and 7 ($x_1/D = 4$) are plotted in figure 6.12, since these positions show the best (observer 1) and the worst (observer 7) grid independence in figure 6.11, respectively. The pressure signal at location 1 has changed slightly, but the main peaks are still correct. The signal at location 7 has changed more.

While the peaks are still captured, small differences in levels and phase are present.

Can the solution be considered independent of the grid? Qualitatively speaking, the different grids give similar results, but the quantitative differences are fairly large. In this study, the database generated with the standard grid is considered grid independent, but the errors found here should be kept in mind when analyzing the results later on. The error in the standard grid is estimated to be smaller than the difference in *OASPL* between the standard and the shortened grids, which yields an estimated maximum error of 3.6 *dB*.

In terms of future work, a real study on the boundary condition dependence is clearly of high priority.

Chapter 7

Open Cavity, Curle's Equation

In this chapter, the radiated sound as computed by Curle's equation will be analyzed. Also, since Curle's equation separates the hydrodynamics and the acoustics of the flow, a deeper analysis of the sound generation will be possible. Before continuing with the analysis, it is important to remember the assumptions introduced in Curle's equation, as discussed in section 2.2.6. Curle's equation will only compute the sound whose propagation is described by an isotropic wave operator, which excludes effects like diffraction and convection with the mean flow from being included.

One of the objectives listed in section 1.2 is to analyze the acoustic noise generation in detail, which is an area that has received remarkably little attention, at least judging from published work. Among the few investigations dealing in detail with the sources of sound, Freund's [49] study of the noise sources in a jet, and Mankbadi *et al's* [50] investigation of supersonic jet noise, are two examples.

7.1 Contributing Source Terms

Curle's equation is linear, and hence the contributions from the various source terms can be computed independently. It is considered 'common knowledge' in the community of aero acoustic researchers, that pressure fluctuations on solid walls will be the primary sources of sound at low Mach numbers, and

Number	Term	\bar{I}/\bar{I}_{ds}
1	$\partial p/\partial\tau _w$	0.46
2	$p _w$	0.37
3	$\partial\tau_{ij}/\partial\tau _w$	$3.5 \cdot 10^{-7}$
4	$\tau_{ij} _w$	$6.9 \cdot 10^{-7}$
5	$\partial^2\rho_\infty u_i u_j/\partial\tau^2$	0.056
6	$\partial^2(\rho - \rho_\infty)u_i u_j/\partial\tau^2$	$2.4 \cdot 10^{-5}$
7	$\partial^2\tau_{ij}/\partial\tau^2$	$\sim 10^{-7}$
8	$\partial^2(p - a_\infty^2\rho)\delta_{ij}/\partial\tau^2$	$5.0 \cdot 10^{-4}$
9	$\partial\rho_\infty u_i u_j/\partial\tau$	0.068
10	$\rho_\infty u_i u_j$	0.045

Table 7.1: Contributions from different source terms

also that Lighthill’s tensor T_{ij} can be simplified to $T_{ij} \approx \rho_\infty u_i u_j$ for most flows, but to the knowledge of this author, no one has actually presented quantitative proof that this is the case. Even if one agrees with the dimensional arguments put forth by Lighthill [17], Curle [18], and others, justifying the facts mentioned above, a quantitative analysis might generate further insight into aerodynamic sound generation.

Curle’s equation in its modified form (5.4) involves a total of 13 source terms; 9 existing in the volume (\ddot{T}_{ij} , \dot{T}_{ij} , and T_{ij} , where each consists of $\rho u_i u_j$, τ_{ij} , and $(p - a_\infty^2\rho)\delta_{ij}$), and 4 existing on the walls (\dot{p} , $\dot{\tau}_{ij}$, p , and τ_{ij}). Furthermore, since the common simplification of T_{ij} introduces ρ_∞ , Lighthill’s tensor is best written $T_{ij} = \rho_\infty u_i u_j + (\rho - \rho_\infty)u_i u_j - \tau_{ij} + (p - a_\infty^2\rho)\delta_{ij}$, bringing the total number of source terms to 16.

In order to analyze the contribution of each source term, the radiated sound at an observer located at $\mathbf{x}/D = (1, 7.16)$ is computed by Curle’s equation. The sound intensity of each contribution is then computed by

$$\bar{I} = \frac{\overline{(p')^2}}{\rho_\infty a_\infty} \quad (7.1)$$

which is derived from equations (2.67) and (2.69). The results, scaled with the intensity computed at the same observer from the DS, are presented in table 7.1. As can be seen in the table, the viscous terms (3, 4, and 7) are negligible, both on the walls and in the volume. The assumption of $\rho \approx \rho_\infty$ introduces a very small error (6), and the entropy term (8) is negligible as well. Due to these findings, the first and zeroth order temporal derivatives of the viscous, entropy, and $(\rho - \rho_\infty)u_i u_j$ terms are skipped.

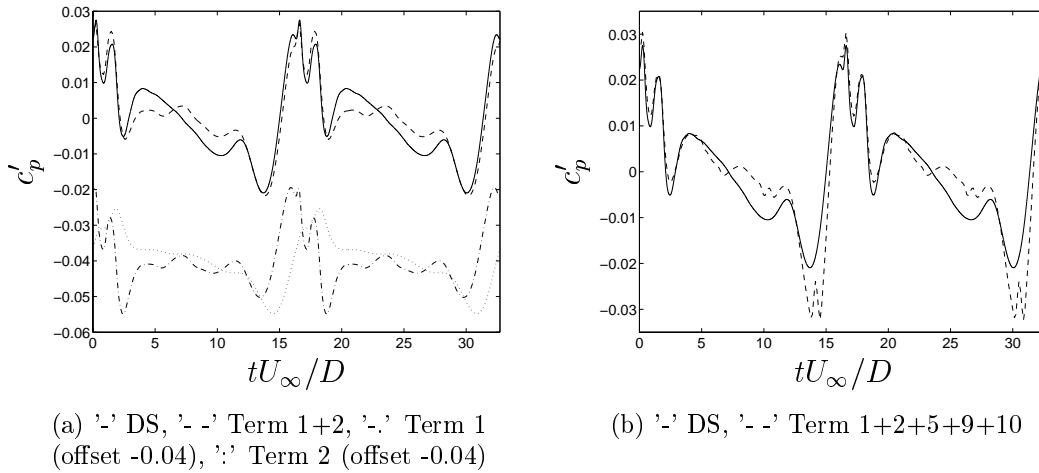


Figure 7.1: Radiated pressure signals at $\mathbf{x}/D = (1, 7.16)$

The contributions of the volume terms (5, 9, and 10) are about 10-15% of the wall term contributions (terms 1 and 2). A comparison like this one, however, does not take any cancellation effects into account. To analyze the contributions further, the pressure signals are plotted versus time in figure 7.1.

Figure 7.1(a) shows the contributions of terms 1 and 2, as well as the sum of them. The sum is very promising, since it shows remarkable similarity to the signal computed in the DS. From the individual contributions, it is seen that terms 1 and 2 are roughly as important (as indicated in table 7.1), and that there exists a phase lag between terms 1 and 2 at the main peaks.

Figure 7.1(b) shows the total contribution of both wall and volume terms. When compared to the results from the wall terms alone, the agreement between the signals computed by Curle's equation and the DS is better around $tU_\infty/D \approx 5$, but worse around $tU_\infty/D \approx 14$. The sharp oscillations around $tU_\infty/D \approx 14$ indicate that the resolution perhaps should have been higher in time.

So which terms are important in Curle's equation? The wall pressure terms (1 and 2) are dominant, and account for most of the radiated sound, whereas the simplified volume terms (5, 9, and 10) only modify the signal slightly. Whether the volume terms are important in terms of the radiated intensity, will be analyzed in section 7.2.

7.2 Radiated Sound

The radiated sound to the observers, listed in table 6.2, is computed by Curle’s modified equation (5.4). Points 1, 2, 8, and 9 are located in positions where they are shielded from parts of the source regions, which in a way illustrates one of the weaknesses of the scalar methods. In this study, those parts of the walls that are blocked from view from the observer, are excluded in Curle’s integral, but the volume integral is taken over the whole domain. Albeit wrong, this is done for simplicity. The error introduced should be fairly small, since these shielded regions are small.

The Overall Sound Pressure Levels (*OASPL*, defined in section 2.5) computed by the wall pressure contribution in Curle’s equation is plotted in figure 7.2(a), and it is seen that the levels are under-predicted by between 0.3

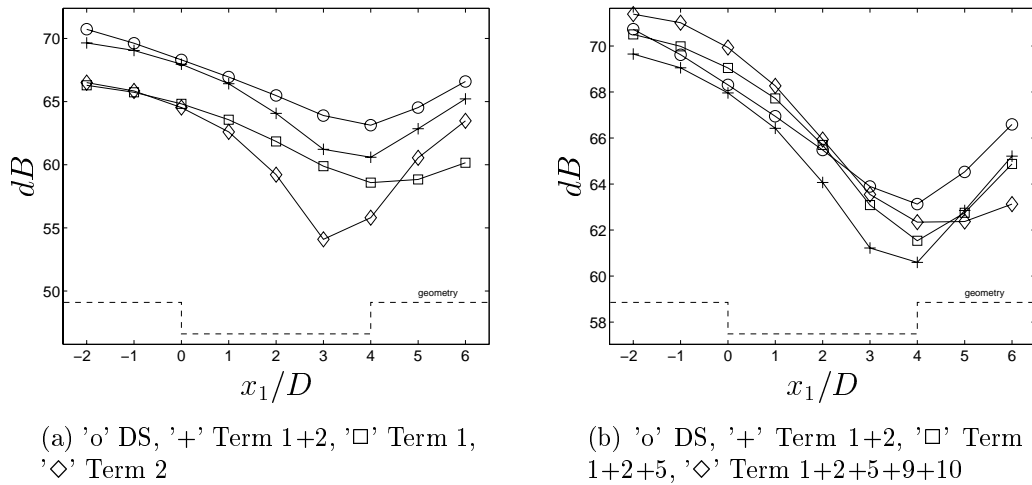


Figure 7.2: Overall Sound Pressure Levels at 9 observers

and 2.7 *dB*. The shape of the directivity is in fairly good agreement with the DS, but the under-prediction is larger straight above the downstream wall. The reason to this is not known, but it is hypothesized that it may be due to the lack of mean flow convection, which would enhance the downstream radiation. Looking at the individual contributions, term 2 shows the strongest directivity. Since this term disappears in the far field, the directivity will be flatter at larger distances.

The radiated sound intensity when the volume terms are added to the wall

terms is plotted in figure 7.2(b). Addition of term 5, i.e. when using terms 1, 2, and 5, improves the agreement slightly, and the maximum error is decreased to about 1.8 dB . The full contribution, i.e. that of terms 1, 2, 5, 9, and 10, makes the agreement slightly worse. The over-prediction upstream is increased, as well as the under-prediction downstream. The maximum error is increased to 3.5 dB .

Since the errors in the Direct Simulation were estimated to be smaller than 3.6 dB in section 6.5.2, it is hard to quantify the accuracy of Curle's equation. All combinations of source terms in figure 7.2, however, give results that are qualitatively correct, and within the error margin in the DS.

7.3 Wall Sources

The strength of the acoustic sources is defined here as

$$S_l \equiv 20 \log_{10} \frac{\Phi_{l,rms}}{\Phi_{l,ref}} \quad (7.2)$$

where Φ_l is one of the source terms listed in table 7.1. With this scaling, an increase of 10 dB is equivalent to a 10-fold increase in intensity, and an increase of 3 dB means a doubling of the intensity. $\Phi_{l,ref}$ acts only to change the level of the source strength, so, as long as only *relative* information is of interest, it can be chosen arbitrarily. Here, the reference for the wall pressure fluctuation ($l = 2$) is chosen to be the same as that for the radiated sound given in section 2.5, i.e. $\Phi_{2,ref} = p_{ref} = \sqrt{\rho_\infty a_\infty 10^{-12} W/m^2}$. This choice means that S_2 is the *OASPL* at the wall. Since terms 1 and 3 involve temporal derivatives, a factor U_∞/D is included in $\Phi_{l,ref}$ as, for example, $\Phi_{1,ref} = p_{ref} U_\infty/D$.

7.3.1 Pressure Sources

The strengths of the wall pressure sources (S_1 and S_2) are plotted in figure 7.3(a). They are small at the inlet, and grow a about a factor of 10 as they approach the leading edge. The low levels at the inlet are explained by the fact that the boundary layer is laminar, and the increase closer to the

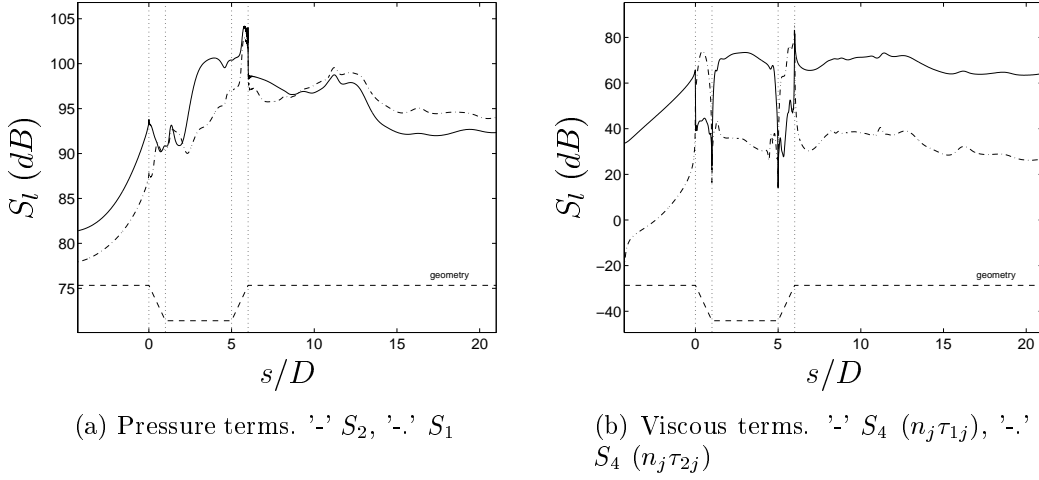


Figure 7.3: Wall source strengths

leading edge is due to the periodic separation of the BL upstream of the leading edge. The sources grow even larger towards the end of the bottom cavity wall, and reach a peak at the upper part of the downstream cavity wall. After the cavity, they stay fairly constant until $x_1/D \approx 11$ (i.e. $s/D \approx 13$), where they drop about 3-5 dB. This drop occurs at the same location where \bar{c}_p was found to have a small peak in figure 6.6(a), and where the small vortex was found in figures 6.4 and 6.5.

The fact that the contributions of terms 1 and 2 were found to be of similar magnitude in section 7.1 is, of course, not a coincidence. Assuming that terms 1 and 2 are affected similarly by cancellations, the radiated intensities would scale as

$$\frac{\bar{I}_2}{\bar{I}_1} \sim \frac{\left(\frac{Ap'}{r^2}\right)^2}{\left(\frac{A}{a_\infty r} \frac{\partial p}{\partial \tau}\right)^2} \sim \frac{a_\infty^2}{r^2} \frac{p_{rms}^2}{(\dot{p})_{rms}^2} \quad (7.3)$$

where A is some sound radiating area. Equation (7.2) is used to write

$$\begin{aligned} p_{rms}^2 &= p_{ref}^2 10^{S_2/10} \\ (\dot{p})_{rms}^2 &= \frac{U_\infty^2 p_{ref}^2}{D^2} 10^{S_1/10} \end{aligned} \quad (7.4)$$

which yields

$$\frac{\bar{I}_2}{\bar{I}_1} \sim \frac{a_\infty^2}{r^2} \frac{D^2}{U_\infty^2} \frac{10^{S_2/10}}{10^{S_1/10}} \sim \frac{1}{M^2 (r/D)^2} 10^{(S_2-S_1)/10} \quad (7.5)$$

In this case, with $M = 0.15$, $r/D \approx 8$ (measured from the end of the cavity to the observer), and $S_1 \sim S_2$, the ratio would be $\bar{I}_2/\bar{I}_1 \approx 0.7$. This is, at least qualitatively, in agreement with the results in table 7.1, and can be taken as an indication that the contributions from terms 1 and 2 are, indeed, affected by cancellations similarly.

The region between $x_1/D \approx 2$ and $x_1/D \approx 11$ is where most of the sound generation takes place, with the downstream cavity wall making the primary contribution. This fact will later be used to explain the directivity of sound from the cavity.

7.3.2 Viscous Sources

The viscous source strength S_4 is plotted in figure 7.3(b). The corresponding plot for S_3 is omitted, partly because of the unimportance of the viscous contribution, and partly because S_3 and S_4 look remarkably similar. As expected, the viscous sources are strongest *along* the wall (as opposed to normal to the wall). The levels are about 25 dB (a factor 1/300) lower than for the pressure sources. Following the arguments above, the viscous contribution to the sound intensity at $\mathbf{x}/D = (1, 7.16)$ should then be about 1/300 of the contributions from the pressure sources. Table 7.1, on the other hand, shows the viscous contribution to be about 10^{-6} of that of the pressure. How can this discrepancy be explained?

The critical point here is the fact that the viscous source strength is large *along* the wall. Since the area radiating to an observer is large when the observer is located nearly normal to the wall, but small when the observer is located nearly tangential to the wall, it is clear that the viscous source strength *normal* to the wall is more relevant in a comparison. The normal source strength is about 65 dB lower than the pressure strength, which corresponds to about 10^{-6} lower intensity.

7.3.3 Correlations

In an attempt to gain further insight into the acoustics of the open cavity, the sound signals at the observers (taken from the DS) are correlated with the dominating sources on the wall, taking the retarded time into account.

The correlation $R_l(\mathbf{x}, \mathbf{y})$ is defined as

$$R_l(\mathbf{x}, \mathbf{y}) \equiv \frac{\overline{p(\mathbf{x}, t)\Phi_l(\mathbf{y}, t - r/a_\infty)}}{p_{rms}(\mathbf{x})\Phi_{l,rms}(\mathbf{y})} \quad (7.6)$$

where $p(\mathbf{x}, t)$ is the pressure signal at an observer location, $\Phi_l(\mathbf{y}, t - r/a_\infty)$ is a source term at a source location, the bar denotes a temporal average, and $r = |\mathbf{x} - \mathbf{y}|$. The correlations for some observers are plotted in figure 7.4.

Before analyzing the correlations, some thought on what the correlation actually means is necessary. A high value of $R_l(\mathbf{x}, \mathbf{y})$ means that the signals have similar shapes and phases, which in this case means that the source has acted constructively (or increased the amplitude). $R_l(\mathbf{x}, \mathbf{y}) < 0$, on the other hand, means that the source has acted destructively and decreased the amplitude of the radiated signal. Whether the source has made a significant contribution or not can not be determined from the correlation; instead, the source strength in figure 7.3 has to be taken in consideration.

Regardless of observation location, the correlations oscillate around 0 above $x_1/D \approx 9$ (i.e. $s/D \approx 11$). This is an effect of the vortices being convected along the wall, generating pressure fluctuations as they pass each point on the wall. Since the length scale of these pressure fluctuations is much shorter than the acoustic length scales, the contributions will change from constructive to destructive and back again for different points along the wall. The drop in source strength occurs at $x_1/D \approx 11$ (see figure 7.3), so the sources above, say, $x_1/D \approx 11$ will probably not contribute significantly to the radiated sound.

Another interesting observation is the ‘spatial phase difference’ between R_1 and R_2 ; it is an effect of the temporal phase difference between \dot{p} and p .¹ Since R_1 and R_2 have different shapes, the radiated sound in the far field will be different from that in the near field, being dominated by the sound generation in different regions.

In general, R_2 changes more between different observation locations than R_1 does. An example of this is the region $x \leq 0$, where R_1 is positive for observers 1, 4, and 6, but where R_2 changes from positive to negative for the same observers. The reason to this is not known.

¹Differentiation of a signal with respect to time changes the phase $\pi/2$.

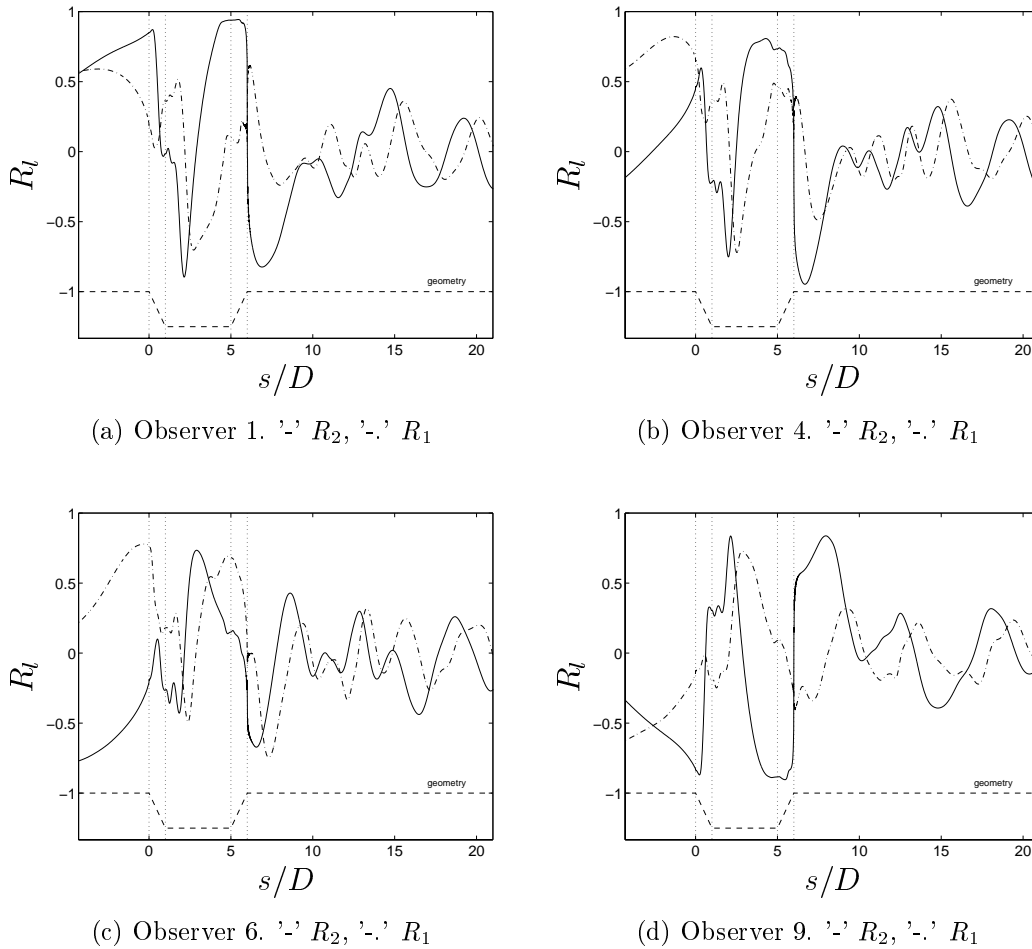


Figure 7.4: Correlations between radiated sound and wall source terms

7.3.4 Directivity

The directivity pattern, specifically the increased radiation at upstream locations, is easier to understand in the framework of Curle's equation than directly from the DS. In Direct Simulations, there is no way of telling where the sound originated from, but when using a scalar equation this becomes possible.

The contribution from a wall pressure source includes a term $l_i n_i = \cos \varphi$, where φ is the angle between the wall normal and the direction to the observer. Due to this, and the geometry of the cavity, it is clear that the

contribution from the downstream cavity wall grows larger upstream. Figure 7.3(a) shows that the strongest source, S_2 , has its peak at the downstream cavity wall, which then explains the increased radiation in the upstream direction. The fact that the correlation R_2 at the downstream cavity wall is very high for observer 1, and becomes successively lower for observers 2 to 6, confirms this.

Since R_2 is higher than R_1 for observers 1 to 5, and especially so for the observers farthest upstream, the main contribution to the radiated sound at those observers is that of term 2. Since the contribution from term 2 will disappear at larger distances (due to the $1/r^2$ factor), and since S_1 has a less pronounced maximum at the downstream cavity wall in figure 7.3(a), it is hypothesized that the upstream dominance will decrease in the far field. This is confirmed by figure 7.2(a), in which the directivity is seen to be flatter for the $\partial p/\partial t$ -term.

A similar argument can be made for the downstream radiation in the far field. Figure 7.4(d) shows that term 2 (R_2) is the main contribution to the sound at observer 9, whereas R_1 is smaller. This indicates that the directivity downstream, as well as upstream, will be flatter farther away from the cavity.

7.4 Volume Sources

The source strength of the volume sources is defined exactly as for the wall sources, i.e. by equation (7.2). The reference value is defined in a similar way, so, for example, $\Phi_{5,ref} = p_{ref}(U_\infty/D)^2$.

The source strengths of the volume sources are plotted in figures 7.5, 7.6, and 7.7. The volume source terms, especially S_5 (figure 7.5), have their maximums right behind the cavity. When comparing with the instantaneous flow field in figures 6.4 and 6.5, it is seen that the region of maximum S_5 is located slightly above the path of the vortices ejected from the cavity. The fact that the source strength is comparatively smaller *in* the cavity is a somewhat surprising result; after all, that is the region where the violent ejection of the vortices originates. The explanation could perhaps be that the flow field in the cavity is built up relatively slowly, whereas it changes more quickly in the region into which the vortices are ejected. This explanation is supported by the fact that the lower order temporal derivatives of T_{ij} (S_9

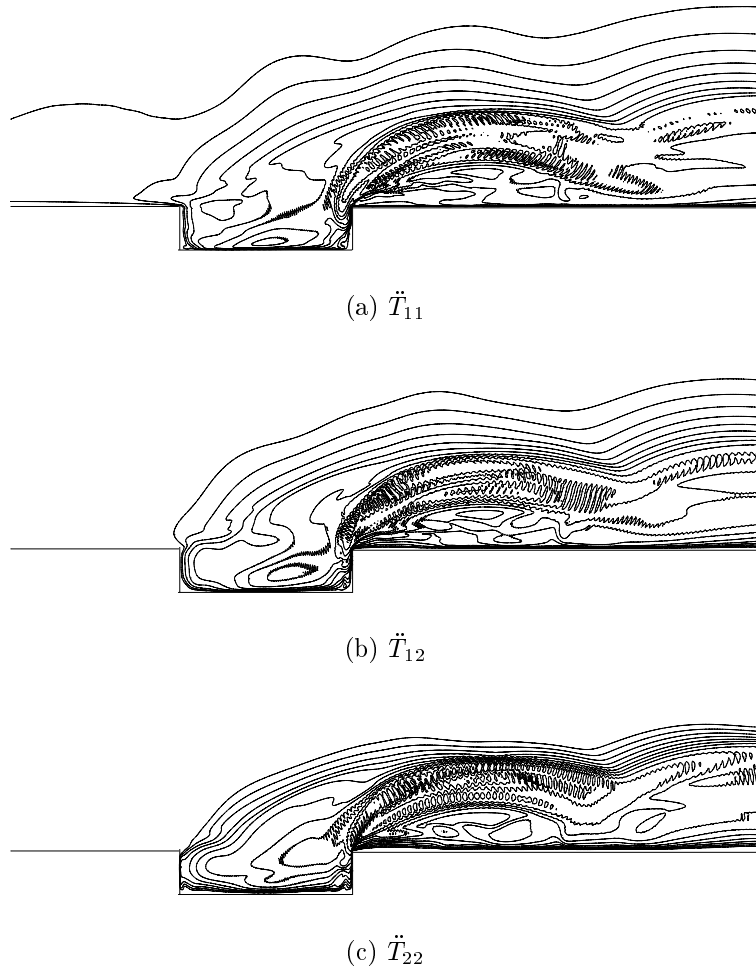


Figure 7.5: Volume source strength, S_5 . 12 levels between 80 *dB* and 140 *dB*.

and S_{10}) have less pronounced maximums in this region.

Knowing that the volume sources have their maximums behind the cavity, it is somewhat surprising that the main contribution from the volume sources is for the *upstream* observers, as shown in figure 7.2(b). The reason for this must be that the volume sources are out of phase with the wall sources, and hence they interact destructively downstream. At higher Mach numbers, the volume sources are expected to be more important, and hence the *upstream* dominance may disappear. That being said, higher Mach numbers would increase the effects of mean convection, an effect excluded from Curle's

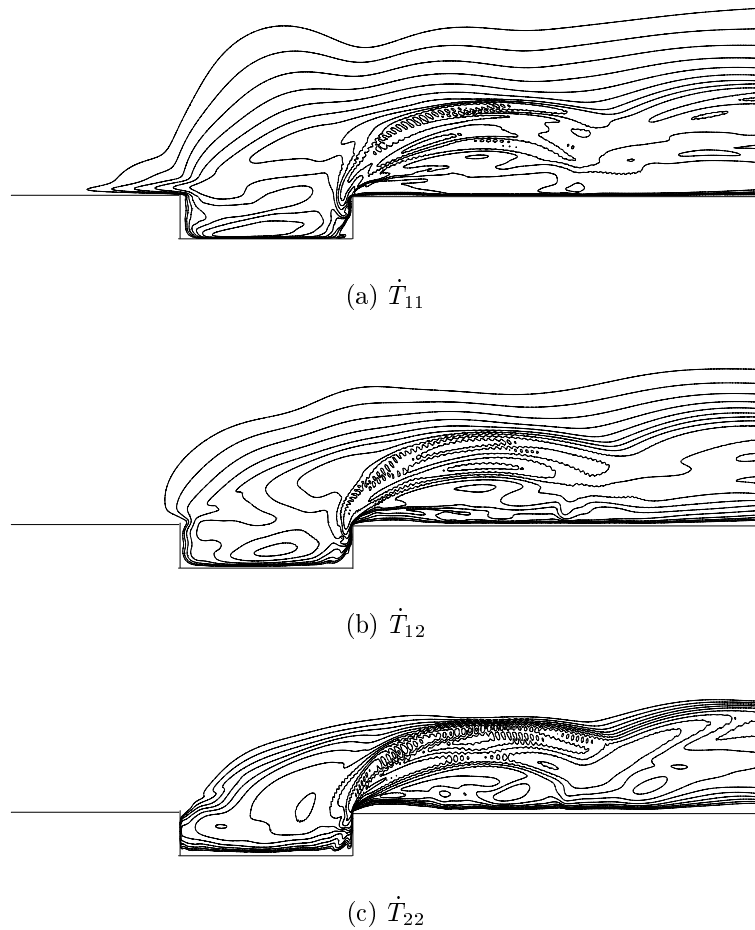


Figure 7.6: Volume source strength, S_9 . 12 levels between 80 dB and 120 dB .

equation, which may make these arguments invalid.

Some numerical, high-wave number, oscillations are present in figure 7.5, but not as much in the other 2 figures. That the \ddot{T}_{ij} term is especially affected by these grid to grid oscillations is not surprising, since the temporal derivatives enhance higher frequencies. Whether these numerical oscillations have an effect on the radiated sound, and if so, how big it is, is not known. They could be removed by increasing the artificial dissipation, but that would affect the accuracy of the DS adversely.

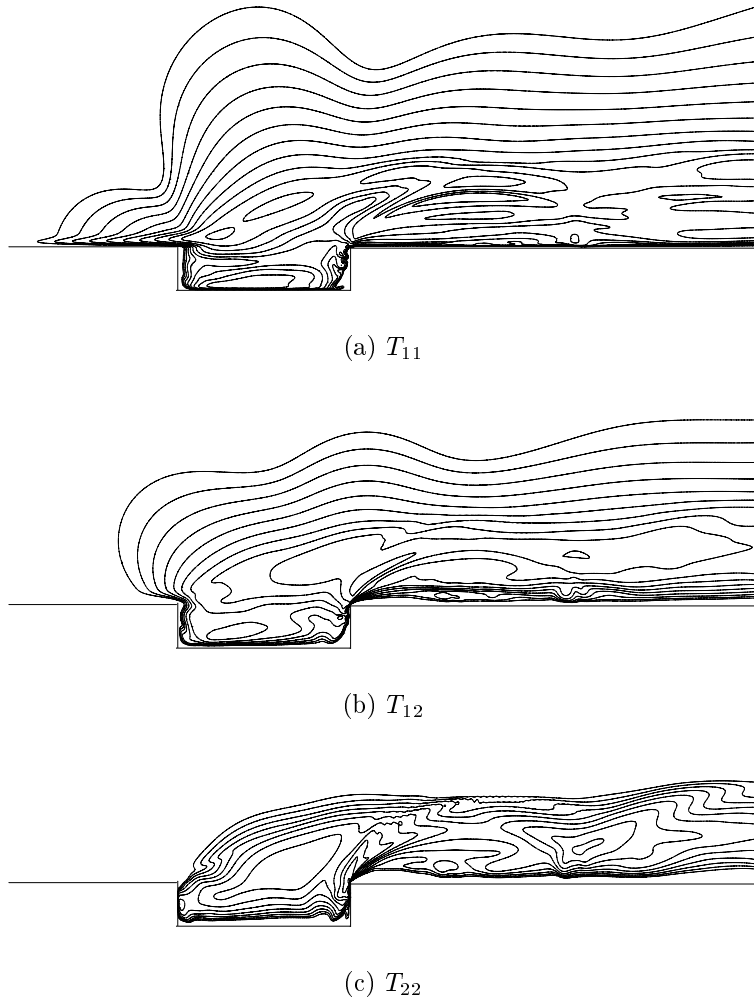
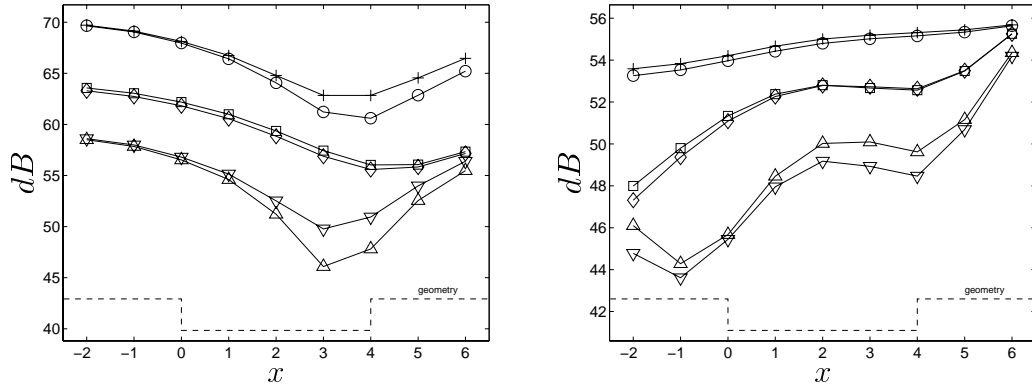


Figure 7.7: Volume source strength, S_{10} . 12 levels between 80 dB and 110 dB .

7.5 Grid Independence of Curle's Equation

The grid independence study in section 6.5 focused on the effects on the Direct Simulation, but the grid independence of Curle's equation can also be checked. Since the dominating source terms are related to hydrodynamic phenomena, the source terms themselves are not expected to be affected much by the shorter grid. Instead, the smaller area (or volume) used to compute the source terms may affect the radiated sound, especially when taking into account the fact that the correlations oscillate around 0 behind the cavity (figure 7.4).



(a) 'o' standard grid Term 1+2, '+' short grid Term 1+2, '◇' standard grid Term 1 (offset -3 dB), '□' short grid Term 1 (offset -3 dB), '△' standard grid Term 2 (offset -8 dB), '▽' short grid Term 2 (offset -8 dB)

(b) 'o' standard grid Term 5, '+' short grid Term 5, '◇' standard grid Term 9 (offset -3 dB), '□' short grid Term 9 (offset -3 dB), '△' standard grid Term 10 (offset -5 dB), '▽' short grid Term 10 (offset -5 dB)

Figure 7.8: Grid independence, Curle's equation, *OASPL* at 9 observers

The *OASPL* in the 9 observation locations are computed for both grids using Curle's equation, and plotted in figure 7.8. The influence on the wall terms is plotted in figure 7.8(a), and it is seen that the contribution from term 1 differs about 0.5 dB for all points between the 2 grids. The effect on term 2 is bigger, about 3.7 dB at the worst location, and the minimum above the downstream cavity wall is less pronounced. The volume terms (5, 9, and 10) are plotted in figure 7.8(b). The terms differ about 0.3 dB, 0.8 dB, and 2.0 dB, respectively.

The conclusion about the grid independence of Curle's equation is similar to the conclusion drawn in section 6.5 about the DS; clearly further studies on the effect of domain size and boundary conditions should be undertaken. That being said, the main features, such as the directivity pattern, are unchanged, and hence it is believed that the results with the standard grid are 'fairly' grid independent. Since the wall sources show no signs of decreasing fast beyond the resolved domain (figure 7.3(a)), Curle's integral will probably have to be taken over quite a large domain downstream to be completely 'grid independent'. The computational cost involved is certainly prohibitive of this.

Chapter 8

Summary of Results

The more general results obtained could be summarized as:

- The solution of Curle's equation has been written on a form with temporal derivatives, while still being valid in the near field.
- The main sources of sound in a low Mach number, wall bounded, flow are the pressure fluctuations on the walls. The viscous contribution on the walls is found negligible, since it mainly acts *along* the walls. The sources in the fluid are small, about 10% of the wall sources for this particular case.
- The common simplification of Lighthill's tensor $T_{ij} \approx \rho_\infty u_i u_j$ is valid, and introduces very small errors at low Mach numbers.
- Being mainly effects of hydrodynamics, the main source terms *should* be computable from the incompressible equations, but this has not been proven in this thesis.
- The tool of correlations can yield further insight into aero acoustic noise generation, by showing which sources have a phase such that they contribute constructively to the radiated sound.
- A Direct Simulation is very sensitive to the boundary conditions. The boundary conditions, coupled with the domain size, used in this study are adequate, but should be improved.

- Curle's equation is, at least in the near field, sensitive to the size of the domain over which the source terms are integrated. This sensitivity, however, is smaller than the sensitivity to boundary conditions of the Direct Simulation.

The findings on the open cavity are:

- The sources of sound are largest on the downstream cavity wall. They are also large along the second half of the bottom of the cavity, and about 2 cavity lengths behind the cavity.
- The directivity of the radiated sound is explained by noting that the dominating wall sources contribute primarily in the wall normal direction. The downstream cavity wall, where the sources are strongest, contributes mainly to the sound in the upstream direction.
- Correlations between the source terms and the radiated sound show that the directivity will be flatter in the far field.
- The incoming boundary layer behaves nothing like a flat plate boundary layer. A consequence of this is that it is hard to specify the boundary layer characteristics in a non-ambiguous way.
- The sound sources in the fluid, albeit small, are large primarily downstream of the cavity.

Have the objectives put forth in section 1.2 been met? Hypothesis 1, that the sources of sound in the fluid are negligible, has been proven correct, since the results using the wall pressure terms alone agree well with the Direct Simulation. Hypothesis 2 has been proven to be correct, since Curle's equation computes the radiated sound accurately. Whether hypothesis 3, that a local analysis of the source terms can be used to draw conclusions about the radiated sound, has been proven or not can not be answered easily. On the one hand, some regions are found to radiate an order of magnitude more energy than other regions, which suggests that if the source strength decreases in those regions, so should the radiated sound. On the other hand, the correlations show how some regions act constructively, and some destructively, depending on the phase of each source. Due to this, the radiated sound is an effect of the sources in the *whole* domain, and hence local analyses may fail. The more general goals of this study, objectives 4-6, have been met.

8.1 Future Work

- The boundary conditions of the Direct Simulation need improvement. Several improved boundary conditions have been proposed in the literature, and an implementation of one of these would be fairly straightforward.
- The domain size of the Direct Simulation should be investigated further. The current domain size only gives *fairly* grid independent results.
- The arguments by Sarkar and Hussaini [24] about why it is preferable to use the temporal form of Lighthill's equation over the spatial form should be investigated further. It is the belief of this author that while their conclusion is correct, their explanation is not necessarily so. One hypothesis is that a double differentiation (in space or time) amplifies high frequency errors, and since a simulation is almost always resolved better in time, this would mean that the temporal form is more accurate. Unfortunately, this has not been looked into, due to a lack of time.
- This author is strongly convinced that the source terms at low Mach number can be computed from an incompressible simulation. This would remove the problems of boundary conditions, and would decrease the computational work substantially.
- The open cavity should be studied at higher Reynolds number, using for example LES and a 3D grid.

Bibliography

- [1] Larsson, J. A note on numerical errors. Internal report 01/06, Chalmers University of Technology, 2001.
- [2] Larsson, J. On low mach number preconditioning by pressure under-relaxation. Internal report 02/02, Chalmers University of Technology, 2002.
- [3] Ribner, H. S. The generation of sound by turbulent jets. *Advances in Applied Mechanics*, 8:103–182, 1964.
- [4] Eriksson, L.-E. Personal communication, lecture notes.
- [5] George, W. K. Personal communication, lecture notes.
- [6] Tam, C. K. W. and Webb, J. C. Dispersion-relation-preserving finite difference schemes for computational acoustics. *Journal of Comp. Physics*, 107:262–281, 1993.
- [7] Bogey, C. and Bailly, C. A family of low dispersive and low dissipative explicit schemes for computing the aerodynamic noise. *AIAA*, 2002-2509, 2002.
- [8] Thompson, K. W. Time dependent boundary conditions for hyperbolic systems. *Journal of Comp. Physics*, 68:1–24, 1987.
- [9] Poinso, T. J. and Lele, S. K. Boundary conditions for direct simulations of compressible viscous flows. *Journal of Comp. Physics*, 101:104–129, 1992.
- [10] Bayliss, A, and Turkel, E. Far-field boundary conditions for compressible flows. *Journal of Comp. Physics*, 48:182–199, 1982.

- [11] Colonijs, T., Lele, S. K., and Moin, P. Boundary conditions for direct computation of aerodynamic sound generation. *AIAA Journal*, 31 No. 9:1574 – 1582, 1993.
- [12] Billson, M. Computational techniques for jet noise predictions. Licentiate thesis, Chalmers University of Technology, 2002.
- [13] Mankbadi, R. R., Shih, S. H., Hixon, R., and Povinelli, L. A. Direct computation of jet noise produced by large-scale axisymmetric structures. *Journal of Propulsion and Power*, 16 No. 2:207–215, 2000.
- [14] Shieh, C. M. and Morris, P. J. Parallel computational aeroacoustic simulation of turbulent subsonic cavity flow. *AIAA*, 2000-1914, 2000.
- [15] Ffowcs Williams, J. E. and Hawkins, D. L. Sound generation by turbulence and surfaces in arbitrary motion. *Philos. Trans. Roy. Soc.*, A 264 No. 1151:321–342, 1969.
- [16] Gloerfelt, X., Bailly, C., and Juvé, D. Computation of the noise radiated by a subsonic cavity using direct simulation and acoustic analogy. *AIAA*, 2001-2226, 2001.
- [17] Lighthill, M. J. On sound generated aerodynamically, I. General theory. *Proc. Roy. Soc.*, A 211:564–587, 1952.
- [18] Curle, N. The influence of solid boundaries upon aerodynamic sound. *Proc. Roy. Soc.*, A 231:505–514, 1955.
- [19] Crighton, D. G. Basic principles of aerodynamic noise generation. *Prog. Aerospace Sci.*, 16:31–96, 1975.
- [20] Phillips, O. M. On the generation of sound by supersonic turbulent shear layers. *Journal of Fluid Mechanics*, 9:1–27, 1960.
- [21] White, F. M. *Fluid Mechanics, 3rd Edition*. McGraw-Hill, 1994.
- [22] Doak, P. E. Analysis of internally generated sound in continuous materials: 2. A critical review of the conceptual adequacy and physical scope of existing theories of aerodynamic noise, with special reference to supersonic jet noise. *Journal of Sound and Vibration*, 25:263–335, 1972.
- [23] Lilley, G. M. On the noise from jets. *AGARD CP-131*, 1974.

BIBLIOGRAPHY

- [24] Sarkar, S. and Hussaini, M. Y. Computation of the acoustic radiation from bounded homogeneous flows. *Computational Aero Acoustics*, pages 335–354, 1993.
- [25] Bechara, W., Bailly, C., and Lafon, P. Stochastic approach to noise modeling for free turbulent flows. *AIAA Journal*, 32 No. 3:455–463, 1994.
- [26] Bailly, C. and Juvé, D. A stochastic approach to compute subsonic noise using linearized Euler’s equations. *AIAA*, 99-1872, 1999.
- [27] Billson, M., Eriksson, L.-E., and Davidson, L. Acoustic source terms for the linear Euler equations on conservative form. *AIAA*, 2002-2582, 2002.
- [28] Hardin, J. C. and Pope, D. S. An acoustic/viscous splitting technique for computational aeroacoustics. *Theoretical Comp. Fluid Dynamics*, 6:323–340, 1994.
- [29] Shen, W. Z. and Sørensen, J. N. Comment on the aeroacoustic formulation of Hardin and Pope. *AIAA Journal*, 37 No. 1:141–143, 1999.
- [30] Wang, M. and Moin, P. Computation of trailing-edge flow and noise using large-eddy simulation. *AIAA Journal*, 38 No. 12:2201–2209, 2000.
- [31] Seror, C., Sagaut, P., Bailly, C., and Juvé, D. Subgrid scale contribution to noise production in decaying isotropic turbulence. *AIAA*, 99-1979, 1999.
- [32] Pierce, A. D. *Acoustics. An Introduction to Its Physical Principles and Applications*. Acoustical Society of America, Woodbury, New York, 1991.
- [33] Lighthill, M. J. *Waves in Fluids*. The Press Syndicate of the University of Cambridge, 1978.
- [34] Gharib, M. and Roshko, A. The effect of flow oscillations on cavity drag. *Journal of Fluid Mechanics*, 177:501–530, 1987.
- [35] Rockwell, D. and Naudascher, E. Review - self-sustaining oscillations of flow past cavities. *Journal of Fluids Engineering*, 100:152–165, 1978.
- [36] Ethembabaoglu, S. On the fluctuating flow characteristics in the vicinity of gate slots. Technical report, University of Trondheim, Norwegian Institute of Technology, 1973.

- [37] Sarohia, V. Experimental investigation of oscillations in flows over shallow cavities. *AIAA Journal*, 15:984–991, 1977.
- [38] Rossiter, J. E. Wind tunnel experiments on the flow over rectangular cavities at subsonic and transonic speeds. Technical report 3438, Aeronautical Research Council Reports and Memoranda, 1964.
- [39] Ahuja, K. K. and Mendoza, J. Effects of cavity dimensions, boundary layer, and temperature on cavity noise with emphasis on benchmark data to validate computational aeroacoustic codes. *NASA*, CR-4653, 1995.
- [40] Ashcroft, G. and Zhang, X. A computational investigation of the noise radiated by flow-induced cavity oscillations. *AIAA*, 2001-0512, 2001.
- [41] Colonius, T., Basu, A. J., and Rowley, C. W. Computation of sound generation and flow/acoustic instabilities in the flow past an open cavity. *3rd ASME/JSME Joint Fluids Engineering Conference, FEDSM99-7228*, 1999.
- [42] Eriksson, L.-E. Development and validation of highly modular flow solver versions in g2dflow and g3dflow. Internal report 9970-1162, Volvo Aero Corporation, 1995.
- [43] Lele, S. K. Compact finite difference schemes with spectral-like resolution. *Journal of Comp. Physics*, 103 No. 1:16–42, 1992.
- [44] Weiss, J. M. and Smith, W. A. Preconditioning applied to variable and constant density flows. *AIAA Journal*, 33:2050–2057, 1995.
- [45] Eriksson, L.-E. A preconditioned Navier-Stokes solver for low mach number flows. Internal report, Volvo Aero Corporation, 1996.
- [46] Tam, C. K. W., Fang, J., and Kurbatskii, K. A. Non-homogeneous radiation and outflow boundary conditions simulating incoming acoustic and vorticity waves for exterior computational aeroacoustics problems. *Int. Journal for Numerical Methods in Fluids*, 26:1107–1123, 1998.
- [47] Hu, F. Q. On absorbing boundary conditions for linearized Euler equations by a perfectly matched layer. *Journal of Comp. Physics*, 129:201–219, 1996.
- [48] Rowley, C. W. and Colonius, T. Discretely nonreflecting boundary conditions for linear hyperbolic systems. *Journal of Comp. Physics*, 157:500–538, 2000.

BIBLIOGRAPHY

- [49] Freund, J. B. Noise sources in a low-Reynolds-number turbulent jet at mach 0.9. *Journal of Fluid Mechanics*, 438:277–305, 2001.
- [50] Mankbadi, R. R., Hayer, M. E., and Povinelli, L. A. Structure of supersonic jet flow and its radiated sound. *AIAA Journal*, 32 No. 5:897–906, 1994.

INTERNAL REPORT 1

CHALMERS



Internal Report 01/06, revised Sept 2002

A Note on Numerical Errors

Johan Larsson

Department of Thermo and Fluid Dynamics
CHALMERS UNIVERSITY OF TECHNOLOGY
and
VOLVO CAR CORPORATION
Göteborg, Sweden, September 2001

Contents

1	Introduction	1
2	The Nature of Spatial Derivatives	2
3	Truncation Errors	4
3.1	Discretization in Space	4
3.1.1	Taylor Expansions and the Modified Equation	4
3.1.2	The Viscous Term	5
3.1.3	The Convective Term	5
3.1.4	Upwinded Convective Schemes	6
3.1.5	Jameson-type Artificial Dissipation	7
3.1.6	Jameson versus Upwinding	7
3.1.7	Choosing the Amount of Added Dissipation	8
3.2	Discretization in Time	10
4	Fourier Analysis of Errors	11
4.1	Semi Discretization	11
4.1.1	Amplitude Errors	12
4.1.2	Phase Velocity Errors	12
4.2	Full Discretization	13
4.2.1	Methodology and Definitions	14
4.2.2	The Crank-Nicolson Scheme	14
4.2.3	A 3-stage Runge-Kutta Scheme	15
4.2.4	A 4-stage Runge-Kutta Scheme	16
5	Finite Difference - Finite Volume	18
5.1	Finite Differences	18

5.2	Finite Volume	18
5.3	Comparison	19
6	Buffer Layers	20
A	Coefficients for Finite Difference Schemes	21

1 Introduction

In this note accuracy and, to some degree, stability of discretized equations is discussed.

All analysis will be conducted using either the linearized Navier-Stokes (N-S) equation

$$\frac{\partial u}{\partial t} + c \frac{\partial u}{\partial x} = \nu \frac{\partial^2 u}{\partial x^2} \quad (1)$$

or the hyperbolic model equation

$$\frac{\partial u}{\partial t} + c \frac{\partial u}{\partial x} = 0 \quad (2)$$

The non-linearities of the N-S will complicate matters substantially, and hence it is chosen to consider the linearized version.

All analysis will be made using finite differences (FD). The reason is that this is considerably simpler than using the Finite Volume (FV) method. All schemes can be transferred between FD and FV on structured grids anyway, which will be shown in section 5.

For further reading, the books by Vichnevetsky [1] and Hirsch [2] can be recommended.

2 The Nature of Spatial Derivatives

In order to understand the effect of truncation errors, it is necessary to understand the effect various forms of spatial derivatives have in an equation. Consider the equation

$$\frac{\partial u}{\partial t} = \alpha \frac{\partial^n u}{\partial x^n} \quad (3)$$

Assume that an intermediate solution (or the initial condition) to this equation can be written as a Fourier series, where each component is

$$u(x, t) = V(t)e^{ikx} \quad (4)$$

In order to obtain a well-defined solution, this component must not grow without bounds as time progresses.

Inserting the component (4) into equation (3), and dividing by e^{ikx} , yields

$$\frac{dV(t)}{dt} = V(t)\alpha(ik)^n \quad (5)$$

Multiplication by the integrating factor $e^{-\alpha(ik)^n t}$ yields

$$\frac{dV(t)}{dt}e^{-\alpha(ik)^n t} - V(t)\alpha(ik)^ne^{-\alpha(ik)^n t} = 0 \quad (6)$$

which can be written as

$$\frac{d}{dt} [V(t)e^{-\alpha(ik)^n t}] = 0 \quad (7)$$

Integrating this yields

$$V(t) = V(0)e^{\alpha(ik)^n t} \quad (8)$$

which can be inserted into (4) to get the solution

$$u(x, t) = V(0)e^{ikx + \alpha(ik)^n t} \quad (9)$$

The effect of spatial derivatives can now be examined. First, consider the first order derivative ($n = 1$), which generates the solution

$$u(x, t) = V(0)e^{ik(x + \alpha t)} \quad (10)$$

This corresponds to translation of the solution with the phase velocity α .

The second order derivative ($n = 2$) generates the solution

$$u(x, t) = V(0)e^{-\alpha k^2 t} e^{ikx} \quad (11)$$

Hence, for $\alpha > 0$ the solution will be damped in time with no translation, since the imaginary part is constant in time. The damping will affect short wave components (high wavenumber k) more. For $\alpha < 0$ the solution will grow without bounds.

The third order derivative ($n = 3$) generates the solution

$$u(x, t) = V(0)e^{ik(x - \alpha k^2 t)} \quad (12)$$

This is translation with the phase velocity αk^2 , and hence the waves will propagate with a speed that is a function of the wavenumber.

The fourth order derivative ($n = 4$) generates the solution

$$u(x, t) = V(0)e^{\alpha k^4 t} e^{ikx} \quad (13)$$

which for $\alpha < 0$ means damping without translation, and for $\alpha > 0$ means growth without bounds.

Generally, odd order derivatives mean translation of waves, and even order derivatives mean damping or amplification, depending on the sign.

3 Truncation Errors

Approximation of a derivative with a finite difference scheme introduces errors. One way of analyzing the errors is to look directly at the terms left out in the approximation.

Throughout this note, a scheme applied at node j will involve the nodes $j+l$.

3.1 Discretization in Space

Semi discretized equations will be studied, i.e. equations that are continuous in time.

3.1.1 Taylor Expansions and the Modified Equation

When either constructing a FD scheme, or analyzing an existing one, one needs to write all variables u_{j+l} in terms of the central one u_j .

$$u_{j+l} = u_j + (l\Delta x) \frac{\partial u_j}{\partial x} + \frac{(l\Delta x)^2}{2!} \frac{\partial^2 u_j}{\partial x^2} + \frac{(l\Delta x)^3}{3!} \frac{\partial^3 u_j}{\partial x^3} + \dots \quad (14)$$

Multiplying by a_l yields

$$a_l u_{j+l} = a_l u_j + a_l (l\Delta x) \frac{\partial u_j}{\partial x} + a_l \frac{(l\Delta x)^2}{2!} \frac{\partial^2 u_j}{\partial x^2} + a_l \frac{(l\Delta x)^3}{3!} \frac{\partial^3 u_j}{\partial x^3} + \dots \quad (15)$$

Sum over all l and divide by Δx^n yields a scheme and its Taylor expansion

$$\sum_l \frac{a_l u_{j+l}}{\Delta x^n} = \sum_l \frac{a_l}{\Delta x^n} u_j + \sum_l \frac{a_l l}{\Delta x^{n-1}} \frac{\partial u_j}{\partial x} + \sum_l \frac{a_l l^2}{2! \Delta x^{n-2}} \frac{\partial^2 u_j}{\partial x^2} + \sum_l \frac{a_l l^3}{3! \Delta x^{n-3}} \frac{\partial^3 u_j}{\partial x^3} + \dots \quad (16)$$

Choosing a set of a_l so that the first n terms on the right hand side cancel out will yield a finite difference scheme for the n th derivative.

The effect that the truncated terms have on the equation is seen when the so called modified equation is studied. When approximating the spatial derivatives in equation (1) with numerical schemes of type (16), the equation solved in the code is

$$\frac{\partial u_j}{\partial t} + \frac{c}{\Delta x} \sum_l a_l u_{j+l} = \frac{\nu}{\Delta x^2} \sum_l d_l u_{j+l} \quad (17)$$

Substituting the Taylor expansions of the schemes into the equation yields the modified equation

$$\frac{\partial u}{\partial t} + c \frac{\partial u}{\partial x} = \nu \frac{\partial^2 u}{\partial x^2} - cT_{conv} + \nu T_{visc} \quad (18)$$

where T_{conv} and T_{visc} are the truncation errors from the convective and viscous terms, respectively. It is now clear that the truncation errors affect the equation, and we will see how in the following sections.

3.1.2 The Viscous Term

The most obvious choice of d_l is a centered scheme. This is also the scheme that gives the highest order truncation error. A centered scheme of an even derivative means that $d_l = d_{-l}$, i.e. that the scheme is symmetric. Due to this symmetry, all odd derivatives in the Taylor expansion (16) will disappear. For example, consider the 3 point central difference approximation

$$\frac{u_{j-1} - 2u_j + u_{j+1}}{\Delta x^2} = \frac{\partial^2 u_j}{\partial x^2} + \frac{\Delta x^2}{12} \frac{\partial^4 u_j}{\partial x^4} + O(\Delta x^4) \quad (19)$$

that generates a modified equation

$$\frac{\partial u}{\partial t} + c \frac{\partial u}{\partial x} = \nu \frac{\partial^2 u}{\partial x^2} - cT_{conv} + \nu \frac{\Delta x^2}{12} \frac{\partial^4 u_j}{\partial x^4} + O(\Delta x^4) \quad (20)$$

This scheme is second order, but what effect does the truncation error have? If only the leading error term is considered, it is seen that this corresponds to equation (3) with $n = 4$ and $\alpha = \nu \frac{\Delta x^2}{12}$. As was shown in section 2, this represents growth of the solution without translation. The magnitude of this growth, however, is much smaller than the damping of the viscous term itself, due to the factor Δx^2 .

Since the errors introduced via the approximation of the viscous term are affecting the amplitude of the solution, but much less so than the viscous term itself, only the order of the approximation is normally considered.

3.1.3 The Convective Term

A centered scheme of an odd derivative will yield $a_l = -a_{-l}$ and $a_0 = 0$, i.e. an anti-symmetric scheme. This anti-symmetry will cancel out all even

derivatives in the Taylor expansion (16). For example, the 3 point central difference approximation

$$\frac{u_{j+1} - u_{j-1}}{2\Delta x} = \frac{\partial u_j}{\partial x} + \frac{\Delta x^2}{6} \frac{\partial^3 u_j}{\partial x^3} + O(\Delta x^4) \quad (21)$$

will generate a modified equation

$$\frac{\partial u}{\partial t} + c \frac{\partial u}{\partial x} = \nu \frac{\partial^2 u}{\partial x^2} + \nu T_{visc} - c \frac{\Delta x^2}{6} \frac{\partial^3 u_j}{\partial x^3} + O(\Delta x^4) \quad (22)$$

This is a second order scheme, and the truncation errors are all odd derivatives. Recall from section 2 that this corresponds to translation of waves with a phase velocity that depends on the wavenumber. This error, called dispersion error, can be dangerous, since it may mean that different waves are superpositioned due to the non-constant phase velocity. This makes the approximation of the convective term fundamentally different from that of the viscous term, since the nature of the scheme may introduce instabilities.

When dispersion errors are present, some dissipation is needed to prevent build-up of waves. There are essentially two ways of getting this dissipation, either by introducing it explicitly or by introducing it via the convective scheme.

3.1.4 Upwinded Convective Schemes

Upwinded schemes for the convective terms in Navier-Stokes are known to enhance stability. To see this, approximate the derivative using two schemes, one left ($a_{-1} = -1, a_0 = 1$) and one right ($a_0 = -1, a_1 = 1$) oriented. If the viscous term is left out, this yields the modified equations

$$\frac{\partial u}{\partial t} + c \frac{\partial u}{\partial x} = \begin{cases} +c\Delta x \frac{\partial^2 u}{\partial x^2} + O(\Delta x^2) & , \text{left oriented} \\ -c\Delta x \frac{\partial^2 u}{\partial x^2} + O(\Delta x^2) & , \text{right oriented} \end{cases} \quad (23)$$

For stability, a positive dissipative term is needed. Hence, the left oriented scheme should be chosen for $c > 0$, and the right oriented scheme for $c < 0$, and hence the name upwinding.

The fact that the scheme is non-centered gives a dissipative truncation error, and the upwinding (i.e. choosing the direction of the scheme) gives it a positive sign.

3.1.5 Jameson-type Artificial Dissipation

An alternative way to obtain a dissipative term in the modified equation is to add it explicitly, and to use a centered scheme for the convective term. This is normally called a Jameson type scheme. Leaving out the viscous term, the equation being solved is

$$\frac{\partial u}{\partial t} + \frac{c}{\Delta x} \sum_l a_l u_{j+l} = \frac{\nu_{num}}{\Delta x^n} \sum_l d_l u_{j+l} \quad (24)$$

where n is the order of the artificial dissipation. A centered approximation of the added term yields

$$\frac{\partial u}{\partial t} + c \frac{\partial u}{\partial x} = -c T_{conv} + \nu_{num} \frac{\partial^n u}{\partial x^n} \quad (25)$$

where the truncation error from the added term has been left out, according to section 3.1.2.

3.1.6 Jameson versus Upwinding

Are the dissipative terms yielded by upwinding and Jameson type schemes similar? Choosing $\nu_{num} = \epsilon c \Delta x^{n-1}$ in the Jameson type equation (24), using a centered scheme for the convective term, yields

$$\frac{\partial u}{\partial t} + \frac{c}{\Delta x} \sum_l a_l u_{j+l} = \frac{\epsilon c}{\Delta x} \sum_l d_l u_{j+l} \quad (26)$$

which can be rewritten as

$$\frac{\partial u}{\partial t} + \frac{c}{\Delta x} \sum_l b_l u_{j+l} = 0 \quad (27)$$

where $b_l = a_l - \epsilon d_l$. Since a_l is anti-symmetric and d_l is symmetric, the resulting scheme b_l is non-centered (which in turn means that the direction of the scheme is important). Since this equation is linear, the modified equation becomes, as expected

$$\frac{\partial u}{\partial t} + c \frac{\partial u}{\partial x} = -c T_{conv} + \epsilon c \Delta x^{n-1} \frac{\partial^n u}{\partial x^n} \quad (28)$$

Equation (28) is similar to (25), but since the dissipative term involves c , the sign of ϵ has to be chosen so that the dissipative term is indeed dissipative. Choosing the sign of ϵ is equivalent to upwinding, as was shown in section 3.1.4.

Which is to prefer, Jameson type or upwinding? Both schemes will do essentially the same, which is adding dissipation to the modified equation. There are, however, some differences.

- Computational efficiency. Upwinding involves checking the direction of propagation of information at every node prior to applying the scheme. This means *if* or *max* statements for every node in the code, which is time consuming. The Jameson type implementation, however, involves only central differences, and hence these checks are not needed. On the other hand, extra lines of code are needed to compute the added term.
- Adaptive dissipation. The dissipative term in an upwinded scheme contains a factor $c\Delta x^{n-1}$, which means that the magnitude of the term is locally dependent on the solution and the mesh. This is not the case with a Jameson scheme. For a scalar equation, like the one studied here, it is straight forward to implement an adaptive coefficient ν_{num} (e.g. $\nu_{num} = |c|\Delta x^{n-1}$). For systems of equations, however, this might not be the case. An example could be the compressible Euler equations, that support different kinds of waves that travel with different wavespeeds.

3.1.7 Choosing the Amount of Added Dissipation

How can the correct amount of added dissipation be chosen, i.e. how can the value of ϵ be decided? The value should be small enough not to affect the solution severely, but big enough not to get stability problems.

One way to estimate the effects on the solution is to compare the amount of added dissipation to the viscous dissipation in N-S. The added term in equation (28) is

$$\epsilon c \Delta x^{n-1} \frac{\partial^n u}{\partial x^n} \quad (29)$$

Recall from section 2 that this term yields solutions on the form

$$u(x, t) = V(0)e^{-\epsilon c \Delta x^{n-1} k^n t} e^{ikx} = V(0)D_a e^{ikx} \quad (30)$$

where

$$D_a = e^{-\epsilon c \Delta x^{n-1} k^n t} \quad (31)$$

Also, recall from section 2 that the viscous term in N-S yields solutions on the form

$$u(x, t) = V(0)e^{-\nu k^2 t} e^{ikx} = V(0)D_v e^{ikx} \quad (32)$$

where

$$D_v = e^{-\nu k^2 t} \quad (33)$$

The ratio of the speeds of these dissipative processes can then be defined as

$$R \equiv \frac{\epsilon c \Delta x^{n-1} k^n}{\nu k^2} = \epsilon \frac{c \Delta x}{\nu} (k \Delta x)^{n-2} \quad (34)$$

which means that the added dissipation will be R times slower than the viscous dissipation.

When using a high order scheme, at least 8 computational points per wavelength are normally required to resolve a wave properly. One guideline for choosing ϵ could be that the dissipation of waves with at least 8 points per wavelength should be much slower than the viscous dissipation of these waves. Hence, for $k \Delta x = \pi/4$, one obtains

$$\epsilon = \frac{\nu}{c \Delta x} \frac{R}{(k \Delta x)^{n-2}} \quad (35)$$

which provides a value of ϵ that effects the solution much less than the viscous term itself.

Another way to estimate the effects of the added dissipation is to analyze how the amplitude of a wave changes as a function of distance traveled. A wave propagating with velocity c will travel a distance $N \Delta x = ct$ over a time t , where N is the number of computational points. Inserting this into expression (31) yields

$$D_a = e^{-\epsilon c \Delta x^{n-1} k^n \frac{N \Delta x}{c}} = e^{-\epsilon (k \Delta x)^n N} \quad (36)$$

Rearranging yields

$$\epsilon = -\frac{1}{N(k \Delta x)^n} \ln(D_a) \quad (37)$$

One guideline for choosing ϵ could be that resolved waves (8 points per wavelength) should be damped only slightly when traveling through the whole domain (D_a large for large N). Another guideline could be that waves with fewer than 8 points per wavelength, say 2 or 4, should be damped quickly (D_a small for small N).

3.2 Discretization in Time

Discretization of the time derivative introduces errors as well. In this section, the explicit Euler and the midpoint rule will be studied, using the model equation (2) as a base.

Using the explicit Euler scheme means that the equation solved in the code is

$$\frac{u_j^{n+1} - u_j^n}{\Delta t} + \frac{c}{\Delta x} \sum_l a_l u_{j+l}^n = 0 \quad (38)$$

where superscript n now denotes timestep. Substituting for the Taylor expansions in time gives the modified equation as

$$\frac{\partial u}{\partial t} + c \frac{\partial u}{\partial x} = -\frac{\Delta t}{2} \frac{\partial^2 u}{\partial t^2} + T_{conv} \quad (39)$$

Taking the time derivative of the model equation yields

$$\frac{\partial^2 u}{\partial t^2} = -c \frac{\partial}{\partial x} \left(\frac{\partial u}{\partial t} \right) = -c \frac{\partial}{\partial x} \left(-c \frac{\partial u}{\partial x} \right) = c^2 \frac{\partial^2 u}{\partial x^2} \quad (40)$$

which, when substituted into the modified equation, yields

$$\frac{\partial u}{\partial t} + c \frac{\partial u}{\partial x} = -\frac{c^2 \Delta t}{2} \frac{\partial^2 u}{\partial x^2} + T_{conv} \quad (41)$$

Since the dissipative error term is negative, explicit Euler will diverge unless the spatial discretization of the convective term adds enough dissipation.

When using the midpoint rule to approximate the time derivative, the equation solved is

$$\frac{u_j^{n+1} - u_j^n}{\Delta t} + \frac{c}{\Delta x} \sum_l a_l u_{j+l}^{n+\frac{1}{2}} = 0 \quad (42)$$

Substituting for the Taylor expansions in time gives the modified equation as

$$\frac{\partial u}{\partial t} + c \frac{\partial u}{\partial x} = -\frac{\Delta t^2}{24} \frac{\partial^3 u}{\partial t^3} + O(\Delta t^4) + T_{conv} \quad (43)$$

As before, the time derivative in the error term is replaced by a spatial derivative to get

$$\frac{\partial u}{\partial t} + c \frac{\partial u}{\partial x} = \frac{c^3 \Delta t^2}{24} \frac{\partial^3 u}{\partial x^3} + O(\Delta t^4) + T_{conv} \quad (44)$$

The error in time is dispersive and of order Δt^2 . As for the explicit Euler, the midpoint rule will need some dissipation from the spatial discretization to converge, but less so since there is no direct amplification.

4 Fourier Analysis of Errors

A different way of studying numerical errors is by studying how a test function is affected by the discretization, in a very similar way to what was done in section 2. Assume that the solution to the model equation (2) can be written as a Fourier series, where each component is

$$u(x, t) = V(t)e^{ikx} \quad (45)$$

Following section 2, the analytical solution to this is

$$u(x, t) = V(0)e^{ik(x-ct)} \quad (46)$$

4.1 Semi Discretization

Discretizing in space only leads to the semi discretized equation at node j

$$\frac{du_j}{dt} = -c \frac{1}{\Delta x} \sum_l a_l u_{j+l} = Au_j \quad (47)$$

where the operator A has been introduced as the discrete differencing operator. Inserting the test function (45) yields

$$\frac{dV(t)}{dt} e^{ikx_j} = -\frac{c}{\Delta x} \sum_l a_l V(t) e^{ikx_j} e^{ik\Delta x l} \quad (48)$$

$V(t)$ and e^{ikx_j} are unaffected by the summation and can be moved out, which yields

$$\frac{dV(t)}{dt} e^{ikx_j} = \hat{A}(k) V(t) e^{ikx_j} \quad (49)$$

where

$$\hat{A}(k) = -\frac{c}{\Delta x} \sum_l a_l e^{ik\Delta x l} \quad (50)$$

Inspection of the right hand sides in equations (47) and (50) reveals that $Au_j = \hat{A}(k) u_j$, i.e. that $\hat{A}(k)$ is the transfer function of the finite differencing.

Division by e^{ikx_j} , and multiplication by the integrating factor $e^{-\hat{A}(k)t}$ yields

$$\frac{d}{dt} [V(t)e^{-\hat{A}(k)t}] = 0 \quad (51)$$

which can be integrated to

$$V(t) = V(0)e^{\hat{A}(k)t} \quad (52)$$

This yields the solution

$$u_j(t) = V(0)e^{\hat{A}(k)t} e^{ikx_j} \quad (53)$$

Splitting the real (\Re) and imaginary (\Im) parts of (53) yields

$$u_j(t) = V(0)e^{\Re\hat{A}(k)t} e^{i(kx_j + \Im\hat{A}(k)t)} \quad (54)$$

When comparing this form of the solution to the analytical solution (46), two kinds of errors are present.

4.1.1 Amplitude Errors

The amplitude of the analytical solution is constant at $V(0)$, but the amplitude of the solution to the semi discretized equation will not be constant. Instead, it will change in time as $e^{\Re\hat{A}(k)t}$.

If $\Re\hat{A}(k)$ is positive, the wave will grow in time and finally diverge. If $\Re\hat{A}(k)$ is negative, the wave will dissipate in time.

The real part of $\hat{A}(k)$ can be written as

$$\Re\hat{A}(k) = -\frac{c}{\Delta x} \sum_l a_l \cos(k\Delta xl) \quad (55)$$

The amplitude errors for some schemes are shown in figure 1(a). The schemes are a first order upwind, a second order central, a third order upwind, and the Dispersion Relation Preserving (DRP) scheme by Tam [3] with a 6th order derivative added for stability according to section 3.1.6. The coefficients of the schemes are listed in the appendix A.

4.1.2 Phase Velocity Errors

The phase velocity c of the analytical solution (46) is constant, i.e. not dependent on the wavelength. Rewriting the solution to the semi discretized equation (54) as

$$u_j(t) = V(0)e^{\Re\hat{A}(k)t} e^{ik\left(x_j + \frac{\Im\hat{A}(k)}{k}t\right)} \quad (56)$$

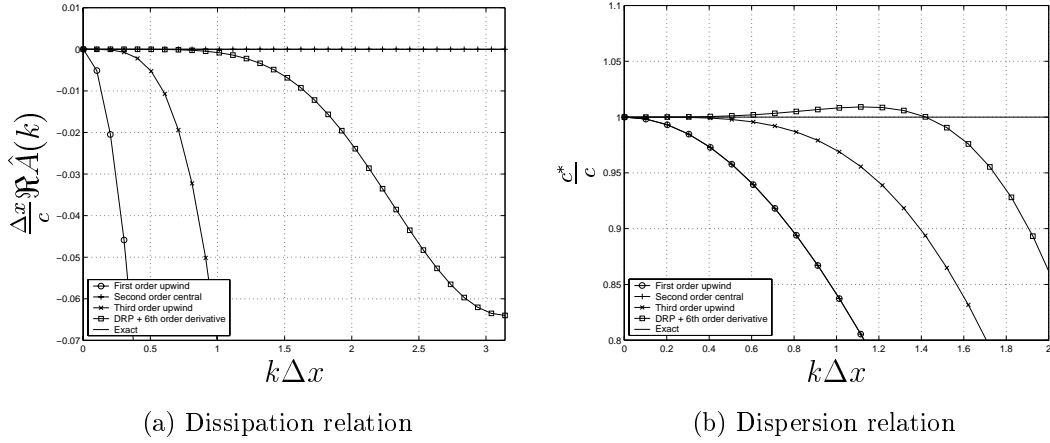


Figure 1: Relations for semi discretization

shows clearly that the phase velocity is dependent on the wavelength. Define this phase velocity as

$$c^*(k) = \frac{-\Im \hat{A}(k)}{k} \quad (57)$$

and simplify to

$$c^*(k) = \frac{c}{k\Delta x} \sum_l a_l \sin(k\Delta x l) \quad (58)$$

The dispersion relation for some schemes are shown in figure 1(b). The schemes are a first order upwind, a second order central, a third order upwind, and the DRP scheme with a 6th order derivative added for stability. The coefficients of the schemes are listed in the appendix A.

4.2 Full Discretization

The analysis of the full discretization is slightly more complex than the previous section. The overall strategy and the necessary definitions will be given in section 4.2.1, and the results for some common schemes will be derived later on.

4.2.1 Methodology and Definitions

In a full discretization, the time derivative in equation (47) is approximated by a numerical scheme, represented by the operator T . This leads to an equation on the form

$$Tu_j = Au_j \quad (59)$$

Using the relation $Au_j = \hat{A}(k) u_j$, inserting the test function (45), and dividing by e^{ikx_j} , yields an equation for, typically, $V(t^{n+1})$ and $V(t^n)$. The amplification function in time is defined as

$$G(k) \equiv \frac{V(t^{n+1})}{V(t^n)} \quad (60)$$

The solution at time t^{n+1} can now be written

$$u_j(t^{n+1}) = G(k)V(t^n)e^{ikx_j} \quad (61)$$

Setting $t^n = 0$, using $G(k) = |G(k)|e^{i\angle G(k)}$, and rewriting the equation yields

$$u_j(\Delta t) = V(0)G(k)e^{ikx_j} = V(0)|G(k)|e^{ik\left(x_j - \frac{-\angle G(k)}{k\Delta t}\Delta t\right)} \quad (62)$$

Comparison between the expressions (62) and (46) directly shows the errors.

The amplitude error, scaled by the *CFL* number as a non-dimensional timestep, is defined as

$$\epsilon_A = \frac{|G(k)| - 1}{\frac{c\Delta t}{\Delta x}} \quad (63)$$

The normalized phase velocity is

$$\frac{c^*}{c} = \frac{-\angle G(k)}{kc\Delta t} = \frac{-\angle G(k)}{k\Delta x \frac{c\Delta t}{\Delta x}} \quad (64)$$

4.2.2 The Crank-Nicolson Scheme

When using the Crank-Nicolson scheme to discretize the time derivative in equation (47) one gets

$$\frac{u_j^{n+1} - u_j^n}{\Delta t} = \frac{1}{2} [Au_j^{n+1} + Au_j^n] \quad (65)$$

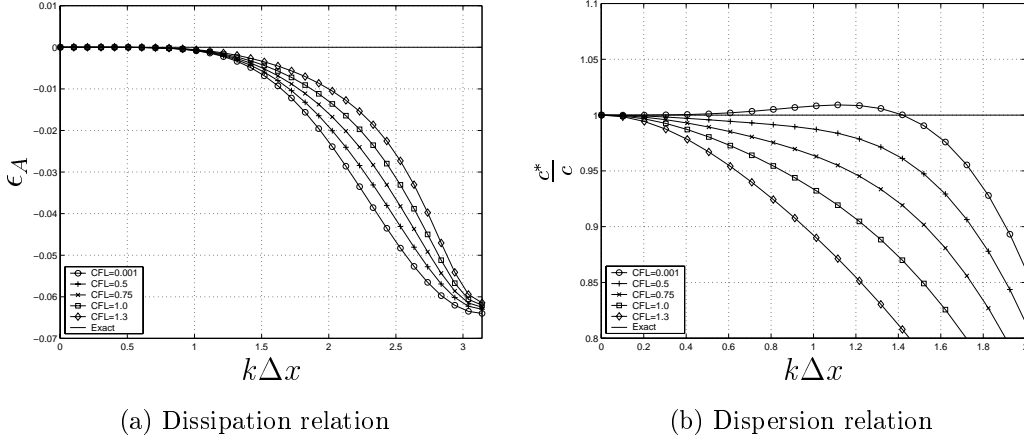


Figure 2: Relations for discretization with Crank-Nicolson

which in turn yields an amplification factor

$$G(k) = \frac{1 + \frac{\Delta t}{2} \hat{A}(k)}{1 - \frac{\Delta t}{2} \hat{A}(k)} \quad (66)$$

The errors for the DRP scheme with a 6th order derivative added for stability together with the Crank-Nicolson scheme in time are shown in figure 2. For amplitude errors, the difference between different timesteps is fairly small. For dispersion errors, however, the dependence on timestep is bigger. For waves with 4 points per wavelength, i.e. $k\Delta x = \pi/4$, a CFL number below approximately 0.5 gives good results.

4.2.3 A 3-stage Runge-Kutta Scheme

The 3-stage Runge-Kutta scheme defined by

$$\begin{aligned} u^{(1)} &= u_j^n + \Delta t A u_j^n \\ u^{(2)} &= \frac{1}{2} \left[u_j^n + u^{(1)} \right] + \frac{\Delta t}{2} A u_j^{(1)} \\ u_j^{n+1} &= \frac{1}{2} \left[u_j^n + u^{(1)} \right] + \frac{\Delta t}{2} A u_j^{(2)} \end{aligned} \quad (67)$$

or, when expanded

$$u_j^{n+1} = u_j^n + \Delta t A u_j^n + \frac{\Delta t^2}{2} A^2 u_j^n + \frac{\Delta t^3}{4} A^3 u_j^n \quad (68)$$

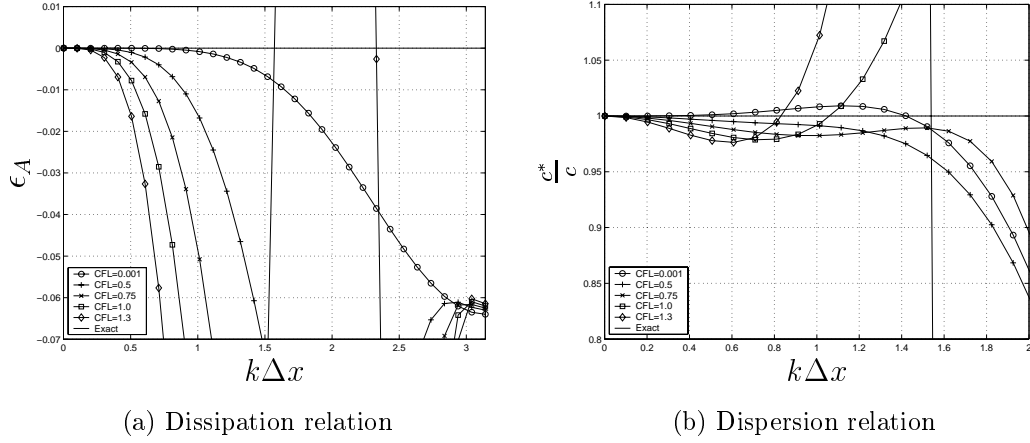


Figure 3: Relations for discretization with 3-stage Runge Kutta

yields an amplification factor

$$G(k) = 1 + \Delta t \hat{A}(k) + \frac{\Delta t^2}{2} \hat{A}^2(k) + \frac{\Delta t^3}{4} \hat{A}^3(k) \quad (69)$$

The errors for the DRP scheme with a 6th order derivative added for stability together with the 3-stage Runge Kutta scheme in time are shown in figure 3. It is seen that all reasonable timesteps are fairly dissipative, and also that the scheme diverges for $CFL = 1.3$.

4.2.4 A 4-stage Runge-Kutta Scheme

The 4-stage Runge-Kutta scheme defined by

$$\begin{aligned} u^{(1)} &= u_j^n + \frac{1}{4} \Delta t A u_j^n \\ u^{(2)} &= u_j^n + \frac{1}{3} \Delta t A u_j^{(1)} \\ u^{(3)} &= u_j^n + \frac{1}{2} \Delta t A u_j^{(2)} \\ u^{n+1} &= u_j^n + \Delta t A u_j^{(3)} \end{aligned} \quad (70)$$

or, when expanded

$$u_j^{n+1} = u_j^n + \Delta t A u_j^n + \frac{\Delta t^2}{2} A^2 u_j^n + \frac{\Delta t^3}{6} A^3 u_j^n + \frac{\Delta t^4}{24} A^4 u_j^n \quad (71)$$

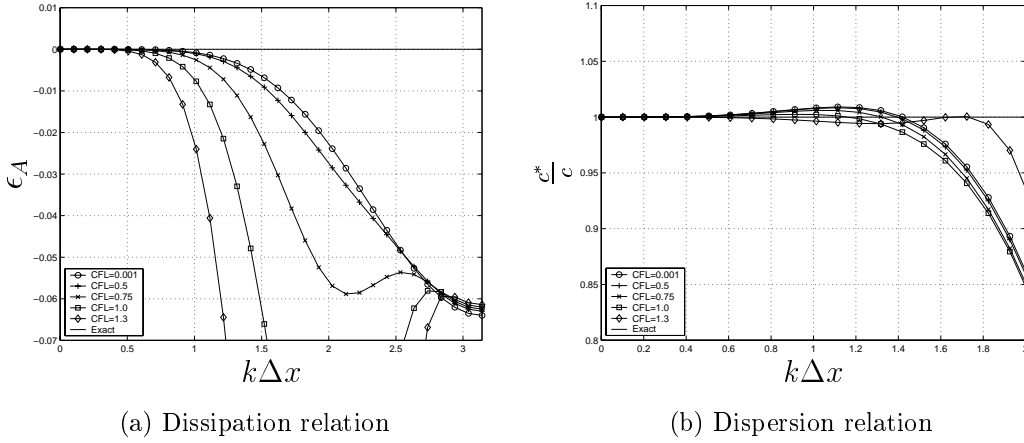


Figure 4: Relations for discretization with 4-stage Runge Kutta

yields an amplification factor

$$G(k) = 1 + \Delta t \hat{A}(k) + \frac{\Delta t^2}{2} \hat{A}^2(k) + \frac{\Delta t^3}{6} \hat{A}^3(k) + \frac{\Delta t^4}{24} \hat{A}^4(k) \quad (72)$$

The errors for the DRP scheme with a 6th order derivative added for stability together with the 4-stage Runge Kutta scheme in time are shown in figure 4. The 4-stage Runge Kutta scheme is quite insensitive to the size of the timestep for dispersion errors, but more sensitive for dissipation errors. For waves with 4 points per wavelength a CFL number below or around 0.75 seems to be adequate.

5 Finite Difference - Finite Volume

Finite volume (FV) schemes on structured meshes have direct equivalents in finite difference (FD) schemes. Consider the equation

$$\frac{\partial u}{\partial t} + \frac{\partial u}{\partial x} = 0 \quad (73)$$

which in FV, on a structured cartesian mesh, becomes

$$\frac{\partial U}{\partial t} + \frac{1}{\Delta x} [u_e - u_w] = 0 \quad (74)$$

where U is the volume average of u and u_e and u_w are the values of u at the east and west faces, respectively. Note that this is an exact relation.

Consider solving equation (73) on the meshes in figure 5 with FD and FV.

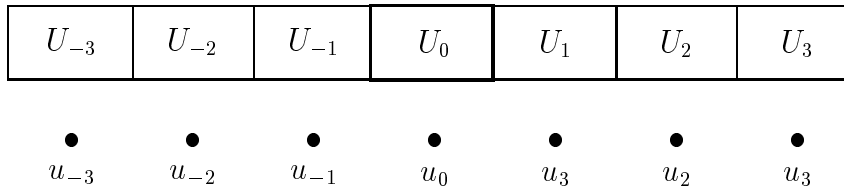


Figure 5: Corresponding FV and FD meshes

5.1 Finite Differences

Using a finite difference scheme with coefficients $a_{-3} \rightarrow a_3$ to solve equation (73), the semi discretized equation becomes

$$\frac{\partial u}{\partial t} + \frac{1}{\Delta x} \sum_{l=-3}^3 a_l u_l = 0 \quad (75)$$

5.2 Finite Volume

In finite volume, the face values of u_e and u_w need to be approximated. If this is done with a 6 point scheme with coefficients $c_1 \rightarrow c_6$, the the face

velocities become

$$u_e = \sum_{j=-2}^3 c_{j+3} U_j \quad , \quad u_w = \sum_{j=-3}^2 c_{j+4} U_j \quad (76)$$

Inserting these expressions into the FV equation (74) yields

$$\frac{\partial U}{\partial t} + \frac{1}{\Delta x} \left[-c_1 U_{-3} + \sum_{j=-2}^2 (c_{j+3} - c_{j+4}) U_j + c_6 U_3 + \right] = 0 \quad (77)$$

5.3 Comparison

Comparing equations (75) and (77) shows that they are similar, and the coefficients are related as

$$\begin{aligned} a_{-3} &= -c_1 \\ a_{-2} &= c_1 - c_2 \\ a_{-1} &= c_2 - c_3 \\ a_0 &= c_3 - c_4 \\ a_1 &= c_4 - c_5 \\ a_2 &= c_5 - c_6 \\ a_3 &= c_6 \end{aligned} \quad (78)$$

6 Buffer Layers

The discretized boundary conditions introduce errors in the solution. These errors are specifically important in Computational Aero Acoustics, since the acoustic field has very low magnitudes. Hence, reflected acoustic waves from the boundaries might contaminate the solution. One way to minimize these reflected waves is to introduce a buffer layer close to the boundary, in which oscillations in the solution are slowly damped before they hit the boundary. The simplest buffer layer is obtained by introducing a source term $-\sigma(u-u^*)$, which forces the solution towards u^* . To get a smooth damping, the damping parameter σ could for instance be chosen as $\sigma = \sigma_0(x/L_b)^2$, where L_b is the length of the buffer layer and x is the distance from the start of the buffer layer.

How would this buffer layer affect the solution? In simplified form, the governing equation would be

$$\frac{\partial u}{\partial t} = -\sigma \frac{a}{L_b}(u - u^*) = -\sigma_0 \frac{a}{L_b} \left(\frac{x}{L_b}\right)^2 (u - u^*) \quad (79)$$

where a/L_b has been added to make σ non-dimensional, and a is the speed of sound. Assuming a constant speed of propagation c , introducing $u' = u - u^*$, and assuming u^* to be constant yields

$$\frac{\partial u'}{\partial t} = -\sigma_0 \frac{a}{L_b} \left(\frac{ct}{L_b}\right)^2 u' \quad (80)$$

which can be solved using the same technique as in section 2 to

$$u'(x, t) = V'(0) e^{-\sigma_0 \frac{a}{L_b} \frac{c^2 t^3}{3L_b^2}} e^{ikx} \quad (81)$$

The damping ratio of the buffer layer is defined as

$$D_b \equiv \frac{|u'(x, t)|}{|u'(x, 0)|} = e^{-\sigma_0 \frac{a}{L_b} \frac{c^2 t^3}{3L_b^2}} \quad (82)$$

Replacing t by $t = L_b/c$, the damping ratio becomes

$$D_b = e^{-\sigma_0 \frac{1}{3M_c}} \quad (83)$$

where $M_c = c/a$ is the Mach number of the disturbance. Equation (83) can now be used to estimate the damping parameter σ_0 .

A Coefficients for Finite Difference Schemes

The coefficients for the first order upwind scheme are

$$\begin{aligned}a_{-3} &= 0 \\a_{-2} &= 0 \\a_{-1} &= -1 \\a_0 &= 1 \\a_1 &= 0 \\a_2 &= 0 \\a_3 &= 0\end{aligned}$$

The coefficients for the second order central scheme are

$$\begin{aligned}a_{-3} &= 0 \\a_{-2} &= 0 \\a_{-1} &= -1/2 \\a_0 &= 0 \\a_1 &= 1/2 \\a_2 &= 0 \\a_3 &= 0\end{aligned}$$

The coefficients for the third order upwind scheme are

$$\begin{aligned}a_{-3} &= 0 \\a_{-2} &= 1/6 \\a_{-1} &= -1 \\a_0 &= 1/2 \\a_1 &= 1/3 \\a_2 &= 0 \\a_3 &= 0\end{aligned}$$

The coefficients for the DRP scheme by Tam [3] are

$$\begin{aligned}a_{-3} &= -0.02651995 \\a_{-2} &= 0.18941314 \\a_{-1} &= -0.79926643 \\a_0 &= 0 \\a_1 &= 0.79926643 \\a_2 &= -0.18941314 \\a_3 &= 0.02651995\end{aligned}$$

The coefficients for a central approximation of a 6th order derivative are

$$\begin{aligned}d_{-3} &= 1 \\d_{-2} &= -6 \\d_{-1} &= 15 \\d_0 &= -20 \\d_1 &= 15 \\d_2 &= -6 \\d_3 &= 1\end{aligned}$$

References

- [1] Vichnevetsky, R. and Bowles, J. B. *Fourier Analysis of Numerical Approximations of Hyperbolic Equations*. SIAM, 1982.
- [2] Hirsch, C. *Numerical Computation of Internal and External Flows*, volume 1. 1988.
- [3] Tam, C. K. W. and Webb, J. C. Dispersion-relation-preserving finite difference schemes for computational acoustics. *Journal of Comp. Physics*, 107:262–281, 1993.

INTERNAL REPORT 2

CHALMERS



Internal Report 02/02

On Low Mach Number Preconditioning by Pressure Underrelaxation

Johan Larsson

Department of Thermo and Fluid Dynamics

CHALMERS UNIVERSITY OF TECHNOLOGY

and

VOLVO CAR CORPORATION

Göteborg, Sweden, March 2002

Contents

1	Introduction	1
2	Preconditioning	2
3	Designing the Preconditioning Matrix	3
4	Diagonalization of the System	4
5	Implementation	7
5.1	Upwinding	7
5.2	Spectral Radii	7
5.2.1	Inviscid	7
5.2.2	Viscous	10
5.3	Preconditioner Multiplication	11
5.4	Choice of α and Speed-up	11
5.4.1	Continuous System	11
5.4.2	Discretized System	12
6	Preconditioning with Dual Time Stepping	14
6.1	Spectral Radii	14
6.1.1	Inviscid Spectral Radius	14
6.1.2	Viscous Spectral Radius	15
6.1.3	Spectral Radius for ΔQ	15
6.2	Choice of α and Speed-up	16
7	Summary and Suggestions	21

1 Introduction

The performance of density based compressible solvers decreases severely as the Mach number (M) is decreased. The reason to this is the large separation in time-scales between convection and acoustic wave propagation. One way to solve this problem is to precondition the system of equations.

The basic idea behind local preconditioning is to modify the physics so that the acoustic time-scales are brought to the same order of magnitude as the convective ones. Modifying the physics inherently means that the solution is changed, but if this modification is done to the time-derivatives only, the steady state solution will be unaffected.

Since acoustic wave propagation is an inviscid phenomena, preconditioning is often developed using the Euler equations.

There are two benefits with preconditioning at low Mach numbers. One is obviously the increased performance of the solver, and the other is increased accuracy when using upwinding or other types of artificial dissipation. This is due to the fact that the dissipation is based on the preconditioned system, which has much lower speeds of propagation.

When using preconditioning together with dual time stepping, it is important to understand the effects of the preconditioning in greater detail. When solving a system of equations iteratively, the rate of convergence is dependent on the rate at which the degrees of freedom are updated. In high Reynolds number, low Mach number flows, the speed of propagation of acoustic disturbances sets a limit on the timestep according to the stability requirements of most explicit schemes. Hence, convected information is updated much slower, leading to a lower rate of convergence. Preconditioning brings down the acoustic speed, enabling the use of a larger timestep, and hence convected information is updated more rapidly. In the optimum situation, all kinds of information will be updated at the same rate.

The preconditioner used and analyzed here was developed by Eriksson [1].

2 Preconditioning

The Euler equations are, when written in terms of conservative variables $Q = [\rho, \rho u, \rho v, \rho w, \rho e_o]^T$,

$$\frac{\partial Q}{\partial t} + \frac{\partial E}{\partial x} + \frac{\partial F}{\partial y} + \frac{\partial G}{\partial z} = 0 \quad (1)$$

This system is to be preconditioned in a way that the characteristic speeds, or eigenvalues, are to be brought down to similar orders of magnitude, while maintaining the same steady state solution. At steady state, the time derivative $\frac{\partial Q}{\partial t}$ disappears. Hence, this term can be multiplied by any non-singular matrix P ,

$$P \frac{\partial Q}{\partial t} + \frac{\partial E}{\partial x} + \frac{\partial F}{\partial y} + \frac{\partial G}{\partial z} = 0 \quad (2)$$

In order to study the preconditioning, the system has to be linearized to

$$P \frac{\partial Q}{\partial t} + A \frac{\partial Q}{\partial x} + B \frac{\partial Q}{\partial y} + C \frac{\partial Q}{\partial z} = 0 \quad (3)$$

where the flux Jacobian are

$$A = \frac{\partial E}{\partial Q} \quad , \quad B = \frac{\partial F}{\partial Q} \quad , \quad C = \frac{\partial G}{\partial Q} \quad (4)$$

The system is transformed by writing it in terms of primitive variables $q = [\rho, u, v, w, p]^T$ by using the transformation matrices

$$S = \frac{\partial Q}{\partial q} \quad , \quad S^{-1} = \frac{\partial q}{\partial Q} \quad (5)$$

to

$$\tilde{P} \frac{\partial q}{\partial t} + \tilde{A} \frac{\partial q}{\partial x} + \tilde{B} \frac{\partial q}{\partial y} + \tilde{C} \frac{\partial q}{\partial z} = 0 \quad (6)$$

where

$$\tilde{P} = S^{-1} P S \quad , \quad \tilde{A} = S^{-1} A S \quad , \quad \tilde{B} = S^{-1} B S \quad , \quad \tilde{C} = S^{-1} C S \quad (7)$$

3 Designing the Preconditioning Matrix

The unpreconditioned system is retrieved by setting P , and hence \tilde{P} , equal to the identity matrix. This system, referred to as the physical system, can be written

$$\left(\frac{\partial q}{\partial t}\right)_{physical} = - \left[\tilde{A} \frac{\partial q}{\partial x} + \tilde{B} \frac{\partial q}{\partial y} + \tilde{C} \frac{\partial q}{\partial z} \right] \quad (8)$$

Similarly, the preconditioned system can be written as

$$\left(\frac{\partial q}{\partial t}\right)_{precond} = -\tilde{P}^{-1} \left[\tilde{A} \frac{\partial q}{\partial x} + \tilde{B} \frac{\partial q}{\partial y} + \tilde{C} \frac{\partial q}{\partial z} \right] \quad (9)$$

which yields

$$\left(\frac{\partial q}{\partial t}\right)_{precond} = \tilde{P}^{-1} \left(\frac{\partial q}{\partial t}\right)_{physical} \quad (10)$$

Since the acoustic speed is related to changes in pressure and entropy as $c^2 = \frac{\partial p}{\partial \rho}$, the idea of Eriksson [1] is to under-relax changes in pressure by a factor α ,

$$\left(\frac{\partial p}{\partial t}\right)_{precond} = \alpha \left(\frac{\partial p}{\partial t}\right)_{physical} \quad (11)$$

where $0 < \alpha < 1$. Entropy waves are defined by changes in $\rho - p/c^2$. Since the preconditioning affects changes in pressure, a correction has to be introduced in order to prevent changes in entropy as

$$\left(\frac{\partial \rho}{\partial t}\right)_{precond} - \left(\frac{\partial \rho}{\partial t}\right)_{physical} = \frac{1}{c^2} \left[\left(\frac{\partial p}{\partial t}\right)_{precond} - \left(\frac{\partial p}{\partial t}\right)_{physical} \right] \quad (12)$$

or simplified

$$\left(\frac{\partial \rho}{\partial t}\right)_{precond} = \left(\frac{\partial \rho}{\partial t}\right)_{physical} - \frac{1 - \alpha}{c^2} \left(\frac{\partial p}{\partial t}\right)_{physical} \quad (13)$$

The preconditioning matrix can now be written as

$$\tilde{P}^{-1} = \begin{pmatrix} 1 & 0 & 0 & 0 & -\frac{1-\alpha}{c^2} \\ 0 & 1 & 0 & 0 & 0 \\ 0 & 0 & 1 & 0 & 0 \\ 0 & 0 & 0 & 1 & 0 \\ 0 & 0 & 0 & 0 & \alpha \end{pmatrix} \quad (14)$$

and the only remaining task is to determine the value of α , which will be done in sections 5.4 and 6.2.

4 Diagonalization of the System

The chosen preconditioning matrix is inserted into equation (6). The system is projected onto a direction $\hat{x} = (n_x, n_y, n_z)$, which yields

$$\tilde{P} \frac{\partial q}{\partial t} + \hat{A} \frac{\partial q}{\partial \hat{x}} = 0 \quad (15)$$

where

$$\hat{A} = n_x \tilde{A} + n_y \tilde{B} + n_z \tilde{C} \quad (16)$$

This is rewritten as

$$\frac{\partial q}{\partial t} + \tilde{P}^{-1} \hat{A} \frac{\partial q}{\partial \hat{x}} = 0 \quad (17)$$

In order to diagonalize this system, and hence decoupling the system into 5 different modes, the eigenvalues and eigenvectors of $\tilde{P}^{-1} \hat{A}$ have to be found. This is done by solving the eigenvalue problem

$$\det(\tilde{P}^{-1} \hat{A} - \lambda \hat{I}) = 0 \quad (18)$$

where \hat{I} is the identity matrix.

The eigenvalues are found to be

$$\begin{aligned} \lambda_{1,2,3} &= U_p \\ \lambda_{4,5} &= \frac{1+\alpha}{2} U_p \pm c' \end{aligned} \quad (19)$$

where $U_p = n_x u + n_y v + n_z w$ and $c' = \sqrt{\frac{(1-\alpha)^2}{4} U_p^2 + \alpha c^2}$.

The corresponding eigenvectors T_i form a transformation matrix T as

$$T = (T_1 \ T_2 \ T_3 \ T_4 \ T_5) \quad (20)$$

The first mode (λ_1 and T_1) is an entropy wave, the second and third are vorticity waves, and the fourth and fifth are acoustic waves. The vorticity waves are not vorticity as it is normally defined, but rather velocity disturbances orthogonal to \hat{x} and to each other. Hence, the eigenvectors T_2 and T_3 can be chosen arbitrarily, as long as they satisfy the orthogonality condition.

For any $\hat{x} = (n_x, n_y, n_z)$,

$$\begin{aligned} T_2 &= \left(0, \frac{-n_y}{\sqrt{n_x^2 + n_y^2}}, \frac{n_x}{\sqrt{n_x^2 + n_y^2}}, 0, 0\right) \\ T_3 &= \left(0, n_z \frac{n_x}{\sqrt{n_x^2 + n_y^2}}, n_z \frac{n_y}{\sqrt{n_x^2 + n_y^2}}, -\sqrt{n_x^2 + n_y^2}, 0\right) \end{aligned} \quad (21)$$

satisfy the orthogonality condition. Defining $SH = \sqrt{n_x^2 + n_y^2}$, $SXH = n_x/SH$, and $SYH = n_y/SH$, this can be written as

$$\begin{aligned} T_2 &= (0, -SYH, SXH, 0, 0) \\ T_3 &= (0, n_z SXH, n_z SYH, -SH, 0) \end{aligned} \quad (22)$$

These definitions of T_2 and T_3 break down at $SH = 0$, or $\hat{x} = (0, 0, 1)$. At this \hat{x} , setting $SXH = 1$ and $SYH = 0$ yields $T_2 = (0, 0, 1, 0, 0)$ and $T_3 = (0, 1, 0, 0, 0)$, which is seen to satisfy the orthogonality condition.

Equation (17) can now be rewritten by multiplication by T^{-1} to

$$T^{-1} \frac{\partial q}{\partial t} + T^{-1} \tilde{P}^{-1} \hat{A} T T^{-1} \frac{\partial q}{\partial \hat{x}} = 0 \quad (23)$$

or

$$\frac{\partial W}{\partial t} + \Omega \frac{\partial W}{\partial \hat{x}} = 0 \quad (24)$$

where $W = T^{-1}q$ are the characteristic variables and $\Omega = T^{-1} \tilde{P}^{-1} \hat{A} T$ is a diagonal matrix with elements λ_i , given by (19). All quantities in T stem from the $\tilde{P}^{-1} \hat{A}$ matrix, and are hence the quantities around which the linearization was done. Denoting these quantities with a subscript o , the characteristic variables become

$$\begin{aligned} W_1 &= \rho - \frac{p}{c_o^2} \\ W_2 &= -SYH u + SXH v \\ W_3 &= n_z(SXH u + SYH v) - SH w \\ W_4 &= \frac{1}{2} \frac{\rho_o \alpha_o}{c_o'} U_p + \frac{1}{2} \frac{1}{c_o^2} \left[1 - \frac{1-\alpha_o}{2} \frac{U_{p,o}}{c_o'}\right] p \\ W_5 &= -\frac{1}{2} \frac{\rho_o \alpha_o}{c_o'} U_p + \frac{1}{2} \frac{1}{c_o^2} \left[1 + \frac{1-\alpha_o}{2} \frac{U_{p,o}}{c_o'}\right] p \end{aligned} \quad (25)$$

The transformation back to primitive variables is given by

$$\begin{aligned}
\rho &= W_1 + W_4 + W_5 \\
u &= -SYH W_2 + n_z SXH W_3 \\
&\quad + \frac{n_x}{\rho_o \alpha_o} \left[\left(\frac{1-\alpha_o}{2} U_{p,o} + c'_o \right) W_4 + \left(\frac{1-\alpha_o}{2} U_{p,o} - c'_o \right) W_5 \right] \\
v &= SXH W_2 + n_z SYH W_3 \\
&\quad + \frac{n_y}{\rho_o \alpha_o} \left[\left(\frac{1-\alpha_o}{2} U_{p,o} + c'_o \right) W_4 + \left(\frac{1-\alpha_o}{2} U_{p,o} - c'_o \right) W_5 \right] \\
w &= -SH W_3 \\
&\quad + \frac{n_z}{\rho_o \alpha_o} \left[\left(\frac{1-\alpha_o}{2} U_{p,o} + c'_o \right) W_4 + \left(\frac{1-\alpha_o}{2} U_{p,o} - c'_o \right) W_5 \right] \\
p &= c_o^2 (W_4 + W_5)
\end{aligned} \tag{26}$$

5 Implementation

The implementation of the preconditioning involves three changes. The spectral radii and the upwinding have to be based on the preconditioned system, and the fluxes have to be multiplied by the preconditioning matrix. The value of the preconditioning parameter α will also have to be decided.

5.1 Upwinding

The upwinding has to be based on the preconditioned system in order to avoid excessive numerical dissipation, something that is explained in [2]. The characteristic variables in the inviscid flux calculation have to be changed to the ones given by (25) and (26).

5.2 Spectral Radii

The spectral radius of a system of equations is related to how far information travels during a certain time. For numerical schemes, the spectral radius will determine the timestep needed to obtain a certain degree of accuracy (and for explicit schemes, to ensure stability).

For the Navier-Stokes equations there are two spectral radii to take into account, the inviscid and the viscous.

5.2.1 Inviscid

To find the inviscid spectral radius, the finite volume equations will be derived, some simplifications will be introduced, and then a solution in the form of a Fourier mode will be studied.

The linearized, preconditioned Euler equations, given by (2), are integrated over a small volume V .

$$\int_V \int \int \frac{\partial Q}{\partial t} dV + P^{-1} A \int_V \int \int \frac{\partial Q}{\partial x} dV$$

$$+P^{-1}B \int \int \int_V \frac{\partial Q}{\partial y} dV + P^{-1}C \int \int \int_V \frac{\partial Q}{\partial z} dV = 0 \quad (27)$$

where the flux Jacobians are assumed to be constant over the volume. Using Gauss' theorem, this can be written as

$$V_c \frac{\partial \bar{Q}}{\partial t} + P^{-1}A \int_S Q n_x \cdot dS + P^{-1}B \int_S Q n_y \cdot dS + P^{-1}C \int_S Q n_z \cdot dS = 0 \quad (28)$$

where V_c is the volume of V , S is the surface surrounding it, and \bar{Q} is the average of Q over the volume. Define the notations

$$SIX = \int \int_{I\text{-face}} n_x \cdot dS \quad , \quad Q_{I+} = Q_{I+\frac{1}{2},J,K} \quad (29)$$

and similar for I, J, K and x, y, z . Assuming that the metrics do not change across a cell, i.e. that for example $SIX_{I+\frac{1}{2},J,K} = SIX_{I-\frac{1}{2},J,K}$, the equation can be written as

$$\begin{aligned} & V_c \frac{\partial \bar{Q}}{\partial t} + \\ & P^{-1}A[SIX(Q_{I+} - Q_{I-}) + SJX(Q_{J+} - Q_{J-}) + SKX(Q_{K+} - Q_{K-})] + \\ & P^{-1}B[SIX(Q_{I+} - Q_{I-}) + SJY(Q_{J+} - Q_{J-}) + SKY(Q_{K+} - Q_{K-})] + \\ & P^{-1}C[SIX(Q_{I+} - Q_{I-}) + SJZ(Q_{J+} - Q_{J-}) + SKZ(Q_{K+} - Q_{K-})] = 0 \end{aligned} \quad (30)$$

Approximating the face values with linear interpolation, for example $Q_{I+} = (\bar{Q}_{I+1} - \bar{Q}_I)/2$, yields

$$\begin{aligned} & V_c \frac{\partial \bar{Q}}{\partial t} + \\ & (P^{-1}A SIX \quad +P^{-1}B SIY \quad +P^{-1}C SIZ) \quad \frac{\bar{Q}_{I+1} - \bar{Q}_{I-1}}{2} \quad + \\ & (P^{-1}A SJX \quad +P^{-1}B SJY \quad +P^{-1}C SJZ) \quad \frac{\bar{Q}_{J+1} - \bar{Q}_{J-1}}{2} \quad + \\ & (P^{-1}A SKX \quad +P^{-1}B SKY \quad +P^{-1}C SKZ) \quad \frac{\bar{Q}_{K+1} - \bar{Q}_{K-1}}{2} \quad = 0 \end{aligned} \quad (31)$$

In order to study the spectral radius, or how far information travels, a solution on the form of a Fourier mode is inserted into the equation. Assume that

$$\bar{Q}_{I,J,K} = \hat{Q} e^{-i\omega t + i(\theta_1 I + \theta_2 J + \theta_3 K)} \quad (32)$$

Waves propagate along characteristics defined by a constant exponent. Hence, during the time Δt the wave propagation is defined by

$$\theta_1 \Delta I + \theta_2 \Delta J + \theta_3 \Delta K = \omega \Delta t \quad (33)$$

Assume that $\theta_1 = \theta_2 = \theta_3 = \theta$, i.e. that the wavelengths of all 3 components are equal. The *CFL* number, which is a measure of how many computational nodes information travels during one timestep, can now be defined as

$$CFL \equiv \Delta I + \Delta J + \Delta K = \frac{\omega \Delta t}{\theta} \quad (34)$$

The maximum value of the *CFL* number determines the stability of most numerical schemes. It is now clear that the maximum value of ω/θ has to be found.

Inserting expression (32) into equation (31) yields

$$\begin{aligned} & V_c(-i\omega)\overline{Q} + \\ & (P^{-1}A \text{ SIX} \quad +P^{-1}B \text{ SIY} \quad +P^{-1}C \text{ SIZ}) \quad \overline{Q} \frac{e^{i\theta_1} - e^{-i\theta_1}}{2} \quad + \\ & (P^{-1}A \text{ SJX} \quad +P^{-1}B \text{ SJY} \quad +P^{-1}C \text{ SJZ}) \quad \overline{Q} \frac{e^{i\theta_2} - e^{-i\theta_2}}{2} \quad + \\ & (P^{-1}A \text{ SKX} \quad +P^{-1}B \text{ SKY} \quad +P^{-1}C \text{ SKZ}) \quad \overline{Q} \frac{e^{i\theta_3} - e^{-i\theta_3}}{2} \quad = 0 \end{aligned} \quad (35)$$

Since $e^{i\theta} - e^{-i\theta} = 2i \sin \theta$, the equation can be simplified to

$$\begin{aligned} & \overline{Q} [\quad -V_c \omega \hat{I} + \\ & (P^{-1}A \text{ SIX} \quad +P^{-1}B \text{ SIY} \quad +P^{-1}C \text{ SIZ}) \quad \sin \theta_1 \quad + \\ & (P^{-1}A \text{ SJX} \quad +P^{-1}B \text{ SJY} \quad +P^{-1}C \text{ SJZ}) \quad \sin \theta_2 \quad + \\ & (P^{-1}A \text{ SKX} \quad +P^{-1}B \text{ SKY} \quad +P^{-1}C \text{ SKZ}) \quad \sin \theta_3] = 0 \end{aligned} \quad (36)$$

where \hat{I} is the identity matrix. Defining

$$\begin{aligned} \beta_x L &= \text{SIX} \sin \theta_1 \quad + \text{SJX} \sin \theta_2 \quad + \text{SKX} \sin \theta_3 \\ \beta_y L &= \text{SIY} \sin \theta_1 \quad + \text{SJY} \sin \theta_2 \quad + \text{SKY} \sin \theta_3 \\ \beta_z L &= \text{SIZ} \sin \theta_1 \quad + \text{SJZ} \sin \theta_2 \quad + \text{SKZ} \sin \theta_3 \end{aligned} \quad (37)$$

and $\beta_x^2 + \beta_y^2 + \beta_z^2 = 1$, the equation can be written

$$\left(\beta_x P^{-1}A + \beta_y P^{-1}B + \beta_z P^{-1}C - \frac{\omega V_c}{L} \hat{I} \right) \overline{Q} = 0 \quad (38)$$

For non-trivial solutions \overline{Q}

$$\det \left[\beta_x P^{-1}A + \beta_y P^{-1}B + \beta_z P^{-1}C - \frac{\omega V_c}{L} \hat{I} \right] = 0 \quad (39)$$

Close inspection (making use of (7)) reveals that this equation is similar to (18), and hence the solutions can be written at once as

$$\omega_i = \frac{L}{V_c} \lambda_i \quad (40)$$

where λ_i are given by (19). The maximum value of the CFL number can now be written

$$\frac{CFL_{max}}{\Delta t} = \frac{\omega}{\theta} = \frac{1}{V_c} \left[\frac{1 + \alpha LU_p}{2} \frac{Lc'}{\theta} + \frac{Lc'}{\theta} \right] \quad (41)$$

where $U_p = \beta_x u + \beta_y v + \beta_z w$ and $c' = \sqrt{\frac{(1-\alpha)^2}{4} U_p^2 + \alpha c^2}$.

Inserting the definitions of β_x , β_y , and β_z yields

$$\frac{LU_p}{\theta} = u \frac{\beta_x L}{\theta} + v \frac{\beta_y L}{\theta} + w \frac{\beta_z L}{\theta} = \frac{\sin \theta}{\theta} [(\vec{U} \cdot \vec{S}I) + (\vec{U} \cdot \vec{S}J) + (\vec{U} \cdot \vec{S}K)] \quad (42)$$

where \vec{U} is the velocity vector and $\vec{S}I$ is the area vector of face I , and

$$\frac{Lc'}{\theta} = \sqrt{\frac{(1-\alpha)^2}{4} \left(\frac{LU_p}{\theta}\right)^2 + \alpha c^2 \left(\frac{L}{\theta}\right)^2} \quad (43)$$

From the definitions of β_x , β_y , and β_z , L/θ is found to be

$$\begin{aligned} \left(\frac{L}{\theta}\right)^2 = \frac{\sin^2 \theta}{\theta^2} [& |\vec{S}I|^2 + |\vec{S}J|^2 + |\vec{S}K|^2 \\ & + 2(SIX SJX + SIY SJY + SIZ SJZ) \\ & + 2(SIX SKX + SIY SKY + SIZ SKZ) \\ & + 2(SJX SKX + SJY SKY + SJZ SKZ)] \end{aligned} \quad (44)$$

Since at least 2 points per wavelength are required to resolve a wave, θ must be in the interval $-\pi \leq \theta \leq \pi$. In this interval, $\sin \theta / \theta \leq 1$. Hence, an upper bound on CFL_{max} can be found by setting $\sin \theta / \theta = 1$ in all expressions, and by taking the absolute values of all terms in parentheses () in equations (42) and (44).

5.2.2 Viscous

It is possible to find the viscous spectral radius by using the same technique as in the previous section, but this is quite cumbersome, and outside the scope of this report. Instead, it can be argued that the quantities in the viscous terms, i.e. u , v , w , and T , are unaffected by the preconditioning. Hence, the preconditioned viscous spectral radius will be the same as the normal one.

5.3 Preconditioner Multiplication

Since the time-derivatives have been altered, the new ones have to be computed by

$$\frac{\partial Q}{\partial t} = -P^{-1} \left[\frac{\partial E}{\partial x} + \frac{\partial F}{\partial y} + \frac{\partial G}{\partial z} - \frac{\partial E_v}{\partial x} - \frac{\partial F_v}{\partial y} - \frac{\partial G_v}{\partial z} \right] \quad (45)$$

The preconditioning matrix is $P^{-1} =$

$$\begin{pmatrix} 1 - \frac{1}{2}fU^2 & fu & fv & fw & -f \\ -\frac{1}{2}fU^2u & 1 + fu^2 & fuv & fuw & -fu \\ -\frac{1}{2}fU^2v & fuv & 1 + fv^2 & fvw & -fv \\ -\frac{1}{2}fU^2w & fuw & fvw & 1 + fw^2 & -fw \\ -\frac{\kappa}{2}U^2 - \frac{1}{4}fU^4 & \kappa u + \frac{1}{2}fU^2u & \kappa v + \frac{1}{2}fU^2v & \kappa w + \frac{1}{2}fU^2w & \alpha - \frac{1}{2}fU^2 \end{pmatrix} \quad (46)$$

where $f = \frac{(1-\alpha)(\gamma-1)}{c^2}$ and $\kappa = 1 - \alpha$.

5.4 Choice of α and Speed-up

The purpose of the preconditioner is to bring the various time-scales in the problem to the same order of magnitude. When studying the continuous system, this is equivalent to bringing the eigenvalues to the same order of magnitude. For a discretized system, however, this is not necessarily the case.

The convective time-scale is determined by the cell length in the direction of the flow, but the acoustic time-scale is determined by the smallest cell length, since acoustic waves propagate isotropically. This means that the optimum choice of α is the one that brings these two time-scales to the same order of magnitude.

5.4.1 Continuous System

The preconditioned eigenvalues are given by (19). Since the system is continuous, U_p is replaced by the velocity magnitude U . Scaling the acoustic

eigenvalues by the convective yields

$$\begin{aligned}\lambda_{1,2,3} &= U \\ \frac{\lambda_4}{U} &= \frac{1+\alpha}{2} + \sqrt{\frac{(1-\alpha)^2}{4} + \frac{\alpha}{M^2}} \\ \frac{\lambda_5}{U} &= \frac{1+\alpha}{2} - \sqrt{\frac{(1-\alpha)^2}{4} + \frac{\alpha}{M^2}}\end{aligned}\quad (47)$$

In subsonic flows, $\lambda_4/U > 1$ and $\lambda_5/U < 0$. Define the quantities Γ as measures of difference in magnitude of the eigenvalues as

$$\begin{aligned}\Gamma_4 &= \frac{\lambda_4}{U} \\ \Gamma_5 &= \max\left(-\frac{\lambda_5}{U}, -\frac{U}{\lambda_5}\right) \\ \Gamma_{max} &= \max(\Gamma_4, \Gamma_5)\end{aligned}\quad (48)$$

A numerical procedure is used to find the α_{opt} that minimizes Γ_{max} , and the results are plotted in figure 1. A simple curve fit yields the optimum $\alpha_{opt} \approx \min(1, 2M^2 + 3M^4 + 20M^6)$. When solving to steady-state, speed-ups of roughly $0.6/M$ have been reported in [1] and [3].

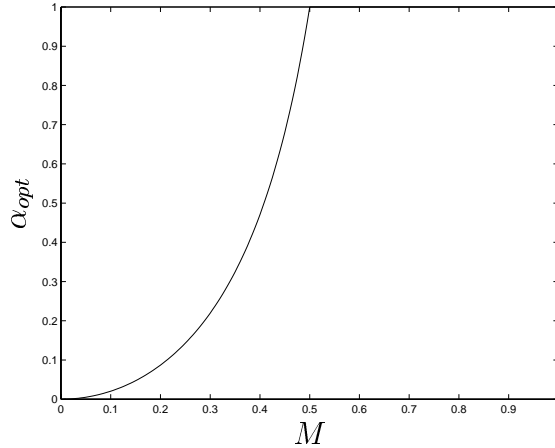


Figure 1: Optimal α for various Mach numbers

5.4.2 Discretized System

Imagine a cell with lengths Δx and Δy in a flow with velocity $\bar{U} = (U, 0, 0)$. The relevant time-scales are now

$$\begin{aligned}\tau_{conv} &= \frac{\Delta x}{U} \\ \tau_{acou} &= \frac{\Delta y}{\lambda_4} = \frac{\Delta y}{\sqrt{\alpha c}}\end{aligned}\quad (49)$$

Setting these two time-scales equal, the optimum value of α becomes

$$\alpha_{opt} = \left(\frac{\Delta y}{\Delta x} \right)^2 M^2 \quad (50)$$

and it is seen that the cell metrics affect α_{opt} . It is possible to derive more general formulations, but that is outside the scope of this report.

6 Preconditioning with Dual Time Stepping

One way to solve unsteady, low Mach number flows is to use dual time stepping. The equations are discretized using an implicit scheme, and then the non-linear system of equations for each timestep is solved by marching in pseudotime to a steady-state solution. The preconditioning can then be applied to the pseudotime derivative.

The Navier-Stokes equations are

$$\frac{\partial Q}{\partial t} + \left[\frac{\partial E}{\partial x} + \frac{\partial F}{\partial y} + \frac{\partial G}{\partial z} - \frac{\partial E_v}{\partial x} - \frac{\partial F_v}{\partial y} - \frac{\partial G_v}{\partial z} \right] = 0 \quad (51)$$

Using the midpoint rule to discretize in time

$$\frac{Q^{n+1} - Q^n}{\Delta t} + [\dots]^{n+\frac{1}{2}} = 0 \quad (52)$$

or, when defining $\Delta Q \equiv Q^{n+1} - Q^n$

$$\Delta Q + \Delta t [\dots]^{n+\frac{1}{2}} = 0 \quad (53)$$

Solving this equation is equivalent to solving

$$\frac{\partial \Delta Q}{\partial \tau} + \Delta Q + \Delta t [\dots]^{n+\frac{1}{2}} = 0 \quad (54)$$

to steady-state in the (non-dimensional) pseudotime τ . Since a steady-state solution is sought, the preconditioning can be applied as

$$P \frac{\partial \Delta Q}{\partial \tau} + \Delta Q + \Delta t [\dots]^{n+\frac{1}{2}} = 0 \quad (55)$$

6.1 Spectral Radii

When using dual time stepping, the spectral radii will be altered slightly.

6.1.1 Inviscid Spectral Radius

The inviscid part of the equations, when projected onto a direction \hat{x} , is

$$\frac{\partial \Delta Q}{\partial \tau} + \Delta t P^{-1} \left[\hat{A} \frac{\partial Q}{\partial \hat{x}} \right]^{n+\frac{1}{2}} = 0 \quad (56)$$

Assuming $Q^{n+\frac{1}{2}} \approx \frac{Q^{n+1}+Q^n}{2}$, and hence $\Delta Q \approx 2(Q^{n+\frac{1}{2}} - Q^n)$, plus using the fact that Q^n is constant in τ , this can be written as

$$\frac{\partial Q^{n+\frac{1}{2}}}{\partial \tau} + \frac{1}{2} \Delta t P^{-1} \left[\hat{A} \frac{\partial Q}{\partial \hat{x}} \right]^{n+\frac{1}{2}} \approx 0 \quad (57)$$

Comparing this to equations (17) and (19), it is seen that the pseudotime eigenvalues become $\lambda_i^\tau \approx \lambda_i \Delta t / 2$. Comparing this to the analysis in section 5.2.1 yields the spectral radius for the pseudotime as

$$\frac{CFL_{max}^\tau}{\Delta \tau} = \frac{CFL_{max}}{2} \quad (58)$$

6.1.2 Viscous Spectral Radius

Similarly to the previous section, the viscous spectral radius for the pseudotime can be written

$$\frac{\phi_{max}^\tau}{\Delta \tau} = \frac{\phi_{max}}{2} \quad (59)$$

6.1.3 Spectral Radius for ΔQ

There is an extra term in the pseudotime equations, which also gives rise to a spectral radius. This part of the equations is

$$\frac{\partial \Delta Q}{\partial \tau} + P^{-1} \Delta Q = 0 \quad (60)$$

Inserting $\Delta Q = \Delta \hat{Q} e^{s\tau}$ yields

$$(sI + P^{-1}) \Delta \hat{Q} = 0 \quad (61)$$

For non-trivial solutions

$$\det(P^{-1} + sI) = 0 \quad (62)$$

The solutions are

$$\begin{aligned} s_{1,2,3,4} &= -1 \\ s_5 &= -\alpha \end{aligned} \quad (63)$$

Defining a stability number Φ_{max}^τ yields

$$\frac{\Phi_{max}^\tau}{\Delta\tau} = |s|_{max} = 1 \quad (64)$$

6.2 Choice of α and Speed-up

When using dual time stepping, the optimum value of the preconditioning parameter α will differ from the theoretical optimum found in section 5.4.

Using the inviscid optimum, $\alpha_{opt} \sim M^2$, means that the inviscid terms are updated in an optimum way, i.e. that all modes are updated in balance. However, when looking at the spectral radius for the ΔQ term, equation (63), it is obvious that updates of one component will be slower for lower values of α . This means that finding the optimum value of α for dual time stepping will be a compromise between decreasing the acoustic eigenvalues, and increasing the updates of the ΔQ term.

Since it is quite hard to derive analytical expressions for α_{opt} , numerical experimentations on a simple test case have been performed, namely a convected vorticity wave in a domain without walls. The results from this test case should be viewed as general indications, since other flows might yield other results.

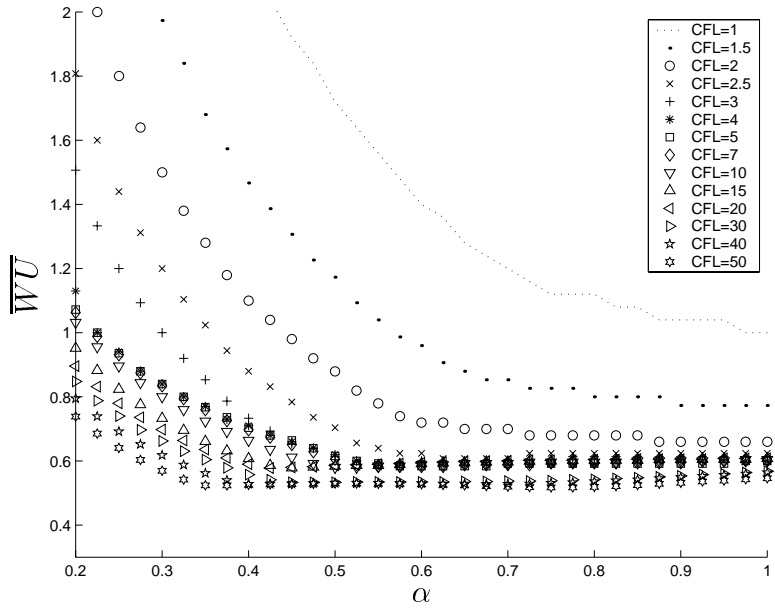
The test case was run for 3 different Mach numbers (M), 11 different CFL numbers, and various values of α . The efficiency of the solver was measured by the work (WU) required to advance the solution a certain time, i.e.

$$WU(M, CFL, \alpha) = \frac{\text{Iterations to convergence for one timestep}}{CFL} \quad (65)$$

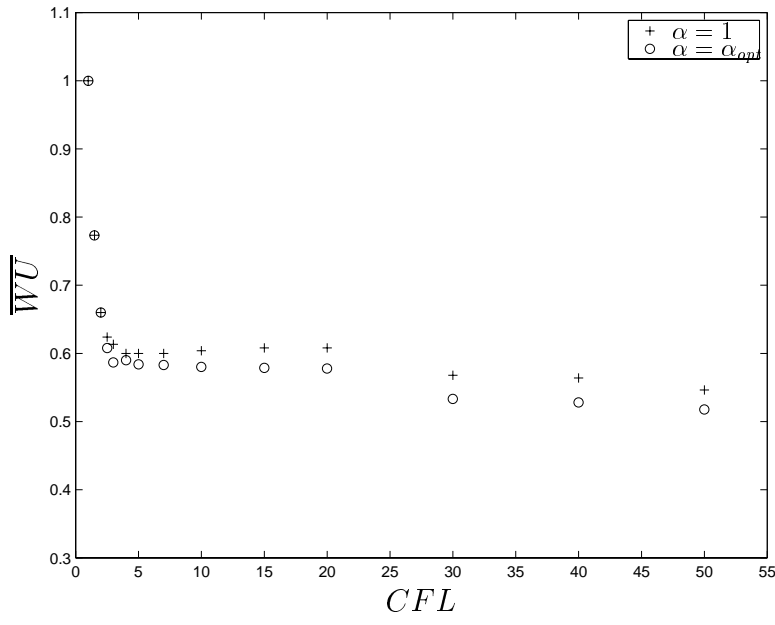
The work was then normalized by the work at $CFL = 1$ and $\alpha = 1$, i.e.

$$\overline{WU}(M, CFL, \alpha) = \frac{WU(M, CFL, \alpha)}{WU(M, 1, 1)} \quad (66)$$

When studying figures 2, 3, and 4, the first observation is that the effect of the preconditioning increases for lower Mach numbers, exactly as expected. It is also evident that for $CFL \leq 2$, $\alpha_{opt} = 1$, which means that the preconditioning will decrease the efficiency of the solver. Generally speaking, the

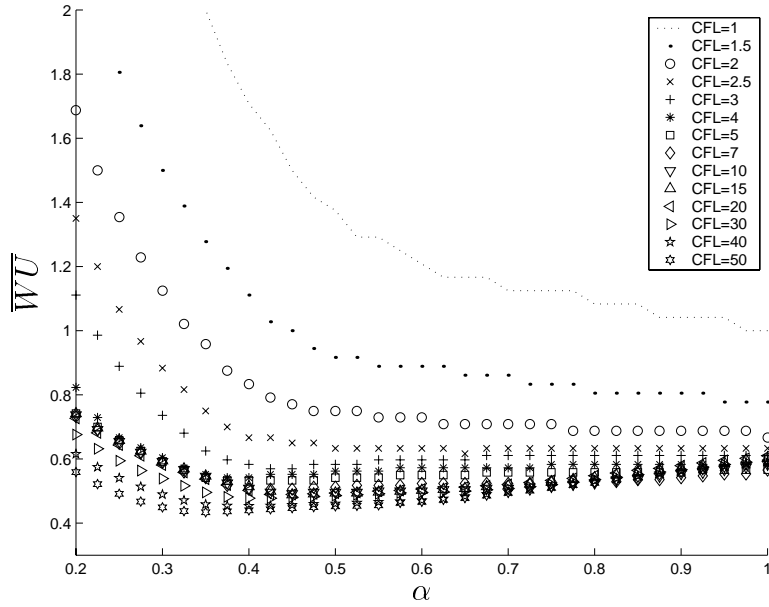


(a) Work as a function of α

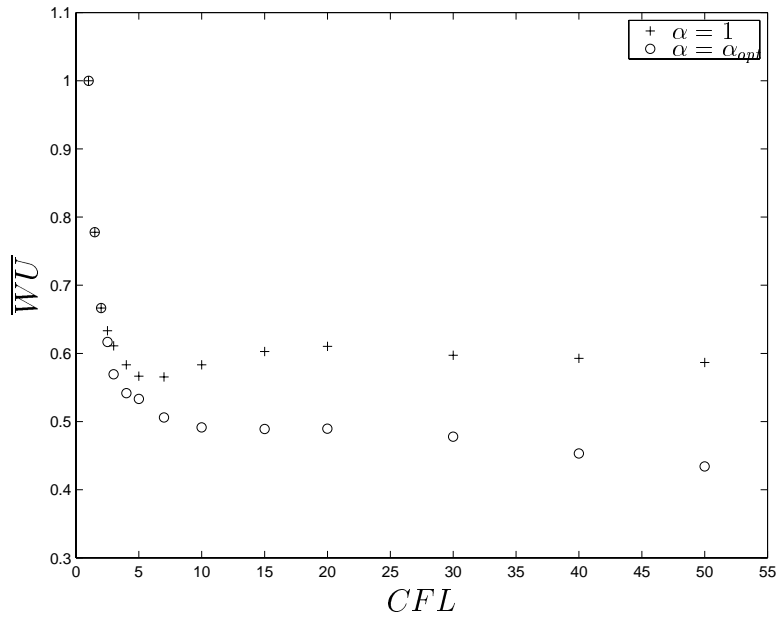


(b) Work as a function of CFL

Figure 2: Dual time stepping with $M = 0.3$

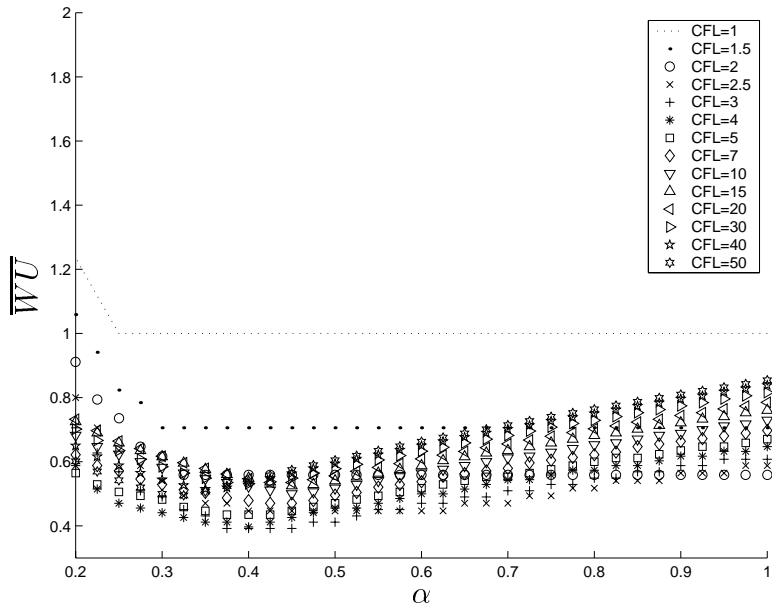


(a) Work as a function of α

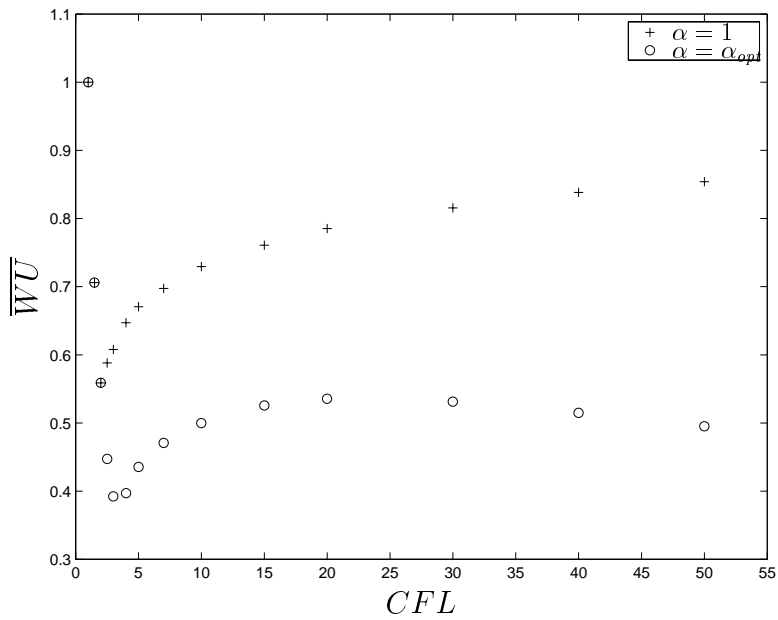


(b) Work as a function of CFL

Figure 3: Dual time stepping with $M = 0.1$



(a) Work as a function of α



(b) Work as a function of CFL

Figure 4: Dual time stepping with $M = 0.03$

increase in performance due to the preconditioning is greater for higher CFL numbers, which might be explained by the fact that the ΔQ term becomes less important.

The maximum speed-ups are nowhere close to the ones reported for stationary flows in [1] and [3], but instead about a factor of 2. This is in line with the findings in [3], which also reports severe decreases in preconditioner performance for dual time stepping. The speed-up and α_{opt} are functions of both M and CFL . For $CFL \geq 3$ and all M , $\alpha_{opt} \approx 0.4$ might be taken as a rough estimate.

Since the speed-ups are as low as they are, a pure explicit solver would outperform the dual time stepping one even at very low Mach numbers.

7 Summary and Suggestions

Low Mach number preconditioning has, in general, two effects. It reduces the numerical dissipation of the inviscid fluxes, and it may improve the efficiency of the solver. When solving unsteady flows using dual time stepping, the increase in performance is less than about a factor of 2 for the Mach numbers considered in this study. If a bigger speed-up is needed, either an explicit solver, or alternative ways of solving the system of equations at each timestep, should be considered.

References

- [1] Eriksson, L.-E. A preconditioned Navier-Stokes solver for low mach number flows. Internal report, Volvo Aero Corporation, 1996.
- [2] Larsson, J. A note on numerical errors. Internal report 01/06, Chalmers University of Technology, 2001.
- [3] Weiss, J. M. and Smith, W. A. Preconditioning applied to variable and constant density flows. *AIAA Journal*, 33:2050–2057, 1995.

